SYNTHESIS AND CHARACTERIZATION OF UPCONVERSION NANOCRYSTALS FOR BIODETECTION

TSANG MING KIU

Ph.D

The Hong Kong Polytechnic University

2018

Department of Applied Physics

SYNTHESIS AND CHARACTERIZATION OF UPCONVERSION NANOCRYSTALS FOR BIODETECTION

Tsang Ming Kiu

A thesis submitted in partial fulfillment of the requirements for the degree of Doctor of Philosophy

July, 2017

CERTIFICATE OF ORIGINALITY

I hereby declare that this thesis is my own work and that, to the best of my knowledge and belief, it reproduces no material previously published or written, nor material that has been accepted for the award of any other degree or diploma, except where due acknowledgement has been made in the text.

_____ (Signed)

___TSANG MING KIU_____ (Name of student)

Abstract

The recent development of lanthanide (Ln^{3+}) ions-doped upconversion nanocrystals (UCNCs) had provide new opportunities for them in diverse biological applications, such as bioimaging, biodetection, drug delivery and phototherapeutic systems. The Ln^{3+} ions play important role in these applications because they are able to harvest near infrared (NIR) photons and convert them into visible photons via upconversion (UC). Owing to the transparency of the NIR excitation to the biological samples, the upconversion luminescence (UCL) process poses no damage to the samples with absence of background fluorescence.

Among the aforementioned biological applications, the unique UCL property can improve the existing gene-based virus oligonucleotide (oligo) detections. Conventional clinical virus gene detection methods, such as reverse-transcription polymerase chain reaction (RT-PCR) and enzyme-linked immunosorbent assays (ELISA) are limited by some drawbacks. For instance, RT-PCR technique requires trained personnel to execute complicated procedures and the sample turnaround time is long while ELISA presents relatively low sensitivity. Owing to the limitations of these techniques, luminescent assays are developed as alternatives for rapid and sensitive detection. Ultraviolet (UV)-excited semiconductor quantum dots were used in downconversion assays. However, the gene oligo backbones are sensitive to UV and thus, prone to degradation. UV also

induces severe background fluorescence that affects the optical readout by resulting in false positive or negative detections. As a result, these factors pave the way for the emergence of UCL in biodetection assays.

Luminescent assays are divided into homogeneous and heterogeneous assays. In general, the heterogeneous assays present superior sensitivity to homogeneous assays owing to the high binding affinity between the nanoprobes and analytes. Therefore, a hybrid nanoprobe/nanoporous membrane heterogeneous platform was designed for ultrasensitive detection of Ebola virus oligos. The detection principle was manifested by the luminescence resonance energy transfer (LRET) between the $BaGdF_5$:Yb/Er UCNCs and gold nanoparticles (AuNPs). The amine-functionalized UCNCs were anchored onto the nanochannels of the amine modified anodized alumina (NAAO) membrane by using glutaraldehyde. The probe oligo was conjugated onto the surface of the anchored UCNCs by the same method. The proof-of-concept system was firstly tested with simulated Ebola virus oligo sequence and yielded a limit of detection (LOD) at 300 femtomolar (fM). Furthermore, an improvement in LOD was found at around 20 folds compared to that of the homogeneous system. The improvement may be attributed to the increased surface area for hybridization in the NAAO membrane. Finally, the assay was tested with extracted oligos from inactive Ebola viron samples. The results indicated that the NAAO-based heterogeneous assay was able to achieve the detection in the fM range. The novel sensor also featured low-cost, rapid and high sensitivity.

Although the heterogeneous sensor showed high sensitivity, the system has high potential for further improvements, such as specificity, fabrication cost and ease of handling. Therefore, the sandwich detection scheme consisting of two sections of oligo probes on the nanoprobes was devised to enhance the specificity of the nanosensor. The oleate-capped $NaGdF_4$:Yb/Er@$NaGdF_4$:Yb/Nd core-shell upconversion nanocrystals (csUCNCs) were synthesized by the coprecipitation method. The UCNCs were treated with acid and conjugated with polyacrylic acid for probe conjugation using covalent coupling. 15 nm AuNPs were selected as the quencher because of its high quenching efficiency and overlapping with the emission profile of the csUCNCs. On the other hand, the instantaneous oligo probe conjugation via acid-assisted method increased the fabrication efficiency. In order to retain the high LOD of heterogeneous assay, the csUCNCs were coupled with the nanoporous polystyrene spheres (nPS) to form a composite. Although the system is not validated with simulated or clinical samples at the moment, it is expected that the cs/nPS composite can increased the LOD and ease of handling for future on-site virus rapid screening application.

List of publications

Peer-reviewed Journals

1. Ming-Kiu Tsang, Yuen-Ting Wong, Jianhua Hao, "Hybrid upconversion nanoprobe/porous polystyrene nanosensor for rapid and specific detection of influenza subtypes" (To be submitted).

2. Ming-Kiu Tsang, Yuen-Ting Wong and Jianhua Hao, "Cutting-edge nanomaterials for advanced multimodal bioimaging applications", Small methods, 2018, 2, 1700265.

3. Ming-Kiu Tsang, Weiwei Ye, GuoJing Wang, Jingming Li, Mo Yang and Jianhua Hao, "Ultrasensitive detection of Ebola virus oligonucleotide based on upconversion nanoprobe/nanoporous membrane System", ACS Nano, 2016, 10, 598-605.

4. Ming-Kiu Tsang, Chi-Fai Chan, Ka-Leung Wong, Jianhua Hao, "Comparative studies of upconversion luminescence characteristics and cell bioimaging based on one-step synthesized upconversion nanoparticles capped with different functional groups", Journal of Luminescence, 2015, 157, 172-178.

5. Ming-Kiu Tsang, Gongxun Bai and Jianhua Hao, "Stimuli responsive upconversion luminescence nanomaterials and films for various applications", Chemical Society Reviews, 2015, 44, 1585-1607.

6. Gongxun Bai, Ming-Kiu Tsang and Jianhua Hao, "Luminescent ions in advanced composite materials for multifunctional applications", Advanced Functional Materials, 2016, 26, 6330-6350.

7. Gongxun Bai, Ming-Kiu Tsang and Jianhua Hao, "Tuning the luminescence of phosphors: beyond conventional chemical method", Advanced Optical Materials, 2015, 3, 431-462.

8. Mei-Yan Tse, Ming-Kiu Tsang, Yuen-Ting Wong, Yi-Lok Chan and Jianhua Hao, "Simultaneous observation of up/down conversion photoluminescence and colossal permittivity properties in (Er+Nb) co-doped TiO_2 materials", Applied Physics Letter, 2016, 109, 042903.

9. Huihong Lin, Ting Yu, Ming-Kiu Tsang, Gongxun Bai, Qinyuan Zhang and Jianhua Hao, "Near-infrared-to-near-infrared down-shifting and upconversion luminescence of KY_3F_{10} with single dopant of Nd^{3+} ion", Applied Physics Letter, 2016, 108, 041902.

10. Man-Chung Wong, Li Chen, Ming-Kiu Tsang, Yang Zhang, Jianhua Hao, "Magnetic-induced luminescence from flexible composite laminates by coupling magnetic field to piezophotonic Effect", Advanced Materials, 2015, 27, 4488-4495.

11. Xiaoqian Su, Chunyu Chan, Jingyu Shi, Ming-Kiu Tsang, Yi Pan, Changming Cheng, Oudeng Gerile, Mo Yang, "A graphene quantum dot@Fe_3O_4@SiO_2 based nanoprobe for drug delivery sensing and dual-modal fluorescence and MRI imaging in cancer cells", Biosensors and Bioelectronics, 2017, 92, 489-495.

12. Huihong Lin, Ting Yu, Gongxun Bai, Ming-Kiu Tsang, Qinyuan Zhang and Jianhua Hao, "Enhanced energy transfer in Nd^{3+}/Cr^{3+} co-doped $Ca_3Ga_2Ge_3O_{12}$ phosphors with near-infrared and long-lasting luminescence properties", Journal of the Materials Chemistry C, 2016, 4, 3396-3402.

13. Chun-Yu Chan, Jiubiao Guo, Cheng Sun, Ming-Kiu Tsang, Feng Tian, Jianhua Hao, Sheng Chen, Mo Yang, "A reduced graphene oxide-Au based electrochemical biosensor for ultrasensitive detection of enzymatic activity of botulinum neurotoxin A", Sensors and Actuators B: Chemical, 2015, 220, 131-137.

Book chapter

1. Ming-Kiu Tsang, Yuen-Ting Wong and Jianhua Hao, Springer-Verlag Berlin Heidelberg, 2018, Nanotechnology characterization tools for biosensing and medical diagnosis, chapter 6: Upconversion nanomaterials for biodetection and multimodal bioimaging using photoluminescence, page 253-273.

Patent

1. Jianhua Hao, Mo Yang, Ming-Kiu Tsang and Weiwei Ye, "Heterogeneous microarray based hybrid upconversion nanoprobe/nanoporous membrane system", filed on 27-Feb, 2017 (File number: 15/442850 (US)).

2. Ming-Kiu Tsang, Yuen-Ting Wong and Jianhua Hao, "A nanoprobe sandwich assay for nucleotide sequence detection", filed on 24-Oct, 2017 (File number: 15/792156(US)).

Presentations/awards in international conferences and exhibitions

1. Ming-Kiu Tsang, Yuen-Ting Wong, Ka-Lok Ho, Yadi Fan, Mo Yang and Jianhua Hao, "Ultrasensitive detection of viruses based on hybrid upconversion nanoprobe/nanoporous membrane system", Phosphor Safari 2016, 27-Nov to 30-Nov, 2016, Hong Kong.

2. Ming-Kiu Tsang, Weiwei Ye, Mo Yang and Jianhua Hao, "Nano biosensor for rapid detection of flu virus", 45th International Exhibition of Inventions Geneva, 29-Mar to 2-Apr, 2017, Geneva, Switzerland. *Award: Gold award with congratulations from the Jury and Special Diploma award from the Ministry of Research and Innovation, Romania.*

3. Ming-Kiu Tsang, Yuen-Ting Wong, Ka-Lok Ho, Yadi Fan, Mo Yang and Jianhua Hao, "Ultrasensitive detection of flu virus oligonucleotides based on hybrid upconversion nanoprobe/nanoporous membrane system" European Materials Research Society, 2017 spring meeting, 22-May to 26-May, 2017, Strasbourg, France.

Acknowledgements

I would like to express my appreciation to my supervisors Prof. J. H. Hao for his excellent guidance and constant encouragement throughout the whole period of my research work.

Moreover, I would like to thank Dr. M. Yang and Dr. W. Ye for their support in the gene oligonucleotide conjugations and detections. I would also like to thank the support of Dr. C. F. Chan and Dr. K. L. Wong of the Hong Kong Baptist University for assisting in *in-vitro* bioimaging and cytotoxicity test. Also, I would like to thank Dr. C. Y. Chan for giving useful advices and guidance in gene oligonucleotide conjugations and hybridizations. In addition, I would like to thank Dr. N. Y. Chan, Dr. T. L. Wong, Dr. H. F. Lui and Dr. L. Wei for the nanoparticle characterization support. I would also like to thank my fellow teammates, Dr. C. J. Tong, Dr. K. L. Ho, Miss Y. Fan, Miss X. Q. Su and Miss Y. T. Wong for her supportive work throughout the Innovation Technology Fund biodetection project.

I gratefully acknowledge the financial support from the Hong Kong Ph.D. Fellowship Scheme Fund, and technical support provided by the University Research Facility in Materials Characterization and Device Fabrication (UMF) of the Hong Kong Polytechnic University.

The last but not least, I would like to thank my family and girlfriend for their understanding, constant support and encouragement.

Table of Contents

List of Figures

List of symbols and abbreviations

Abbreviations / Symbols	Descriptions
ξ	Zeta potential
Ln^{3+}	Lanthanide ions
UCNCs	Upconversion nanocrystals
core UCNCs	Core upconversion nanocrystals
csUCNCs	Core-shell upconversion nanocrystals
AuNPs	Gold nanoparticles
NAAO	Anodized alumina
nPS	Nanoporous polystyrene spheres
QDs	Quantum dots
UC	Upconversion
UCL	Upconversion luminescence
PL	Photoluminescence
TPA	Two photon absorption
ESA	Excited state absorption
ETU	Energy transfer upconversion
EMU	Energy migration-mediated upconversion
NIR	Near infrared
UV	Ultraviolet
cDNA	Complementary DNA
Oligo	Oligonucleotide
RT-PCR	Reverse-transcription polymerase chain reaction
ELISA	Enzyme-linked immunosorbent assays
FRET	Fluorescence resonance energy transfer
LRET	Luminescence resonance energy transfer
LOD	Limit of detection

fM	Femtomolar
pM	Picomolar
TEM	Transmission electron microscopy
SEM	Scanning electron microscopy
FTIR	Fourier transform infrared spectroscopy
XRD	X-ray diffraction
MRI	Magnetic resonance imaging
PET	Positron emission tomography
SPECT	Single photon emission computed tomography
USI	Ultrasound imaging
PAI	Photoacoustic imaging

1. Introduction

1.1 Photoluminescence and its mechanism

Photoluminescence (PL) is the emission of photons when a material absorbed the excitation photons. The excitation source, for example ultraviolet (UV) and near infrared light (NIR), can be used to excite the material to obtain different wavelengths of photons. The photoluminescent materials are termed as phosphors,[1] they can exist as different forms of materials, for example thin films, powders and colloidal solutions. Owing to the advances in nanotechnology, the synthesis of nanocrystals had been applied in diverse fields of applications, ranging from lighting, security, biological and sensing.[2–7] Therefore, it is of high importance to understand the light emission mechanism. Figure 1(a) shows two basic components in a typical PL system: the host matrix and activator ions, the host is a chemically inert material to accommodate the doping ions while the activator ions are responsible for absorbing the incoming excitation photons and then return to ground state for photon emissions. Moreover, the scenario can be expressed in term of energy levels in Figure 1(b). It is important to note that the emissions of phonons after population of activator ions to higher energy levels, such emissions may contribute to the emission of photons of different wavelengths.

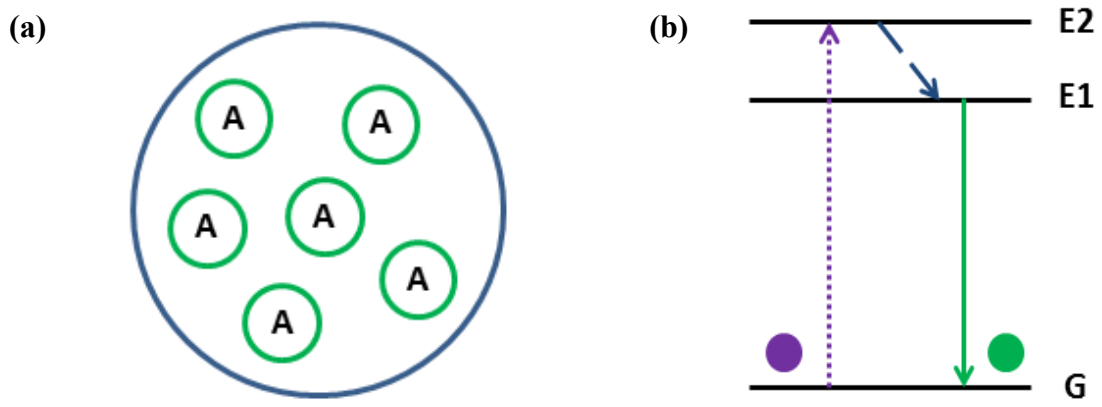

Figure 1(a) Typical PL material system consisting of the host and the activator ions (A) and (b) The simplified energy level diagram of the corresponding activator-host system. G, E1 and E2 are the ground state and higher energy states. The dotted line and purple circle represents the excitation energy, the dashed line represents the phonon emission, the solid line and green circle represents the downward transition back to ground state and emitted photon respectively.

However, the luminescent efficiency of the host-activator ions system in Figure 1(a) can be further improved by the introduction of sensitizer ions. The sensitizer ions usually match the energy level of the activator ions for efficient energy transfer. In addition, the sensitizer ions usually exhibit high absorption probability at the excitation wavelength. Therefore, this can maximize the energy harvesting ability of the host. Figure 2(a) and (b) depicts the schematic of the sensitizer-activator in the host matrix and simplified energy level diagram, respectively. The ratios of the concentration of the sensitizer and activator ions play important role in the optical properties of phosphors because they determine the distance between the two types of ions for energy transfer.

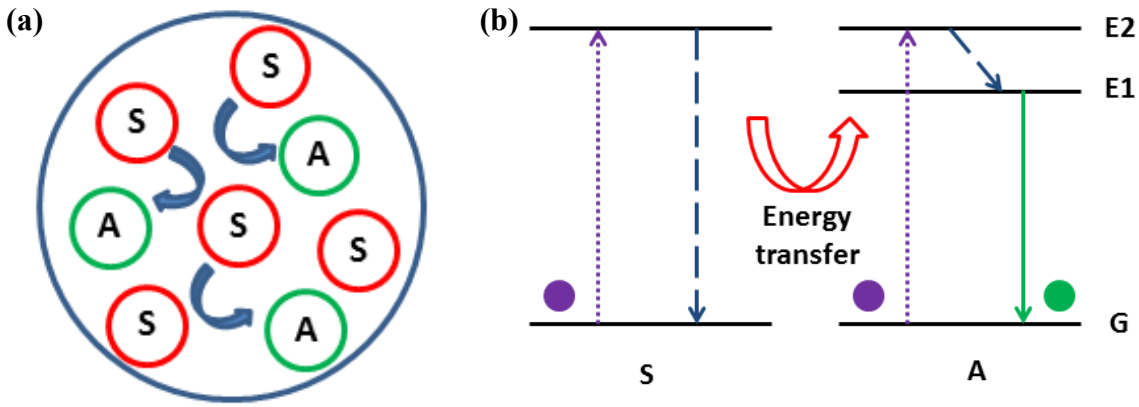

Figure 2(a) Schematic drawing of the sensitizer-activator system in a host (Blue arrows indicate energy transfer) and (b) The simplified energy level diagram of the corresponding sensitizer (S)-activator (A) system. G, E1 and E2 are the ground state and higher energy states. The dotted line and purple circle represents the excitation energy, the dashed line represents the phonon emission, the solid line and green circle represents the downward transition back to ground state and emitted photon respectively.

The observation of the differences in the excitation and emission wavelengths can be described by Stokes shift[8] (Figure 3(a)). It refers to the difference in wavelength of the absorption and emission maxima; the excitation wavelength is shorter than that of the emitted wavelength. One of the well-known examples is semiconductor quantum dots (QDs) and it is well-recorded in textbooks and reviews.[9–12] The CdSe QDs are excited by UV excitation to emit lower energy photons. Moreover, they exhibit size dependent PL and hence it is easy to tailor the QDs to emit multicolor photons by using single wavelength excitation.

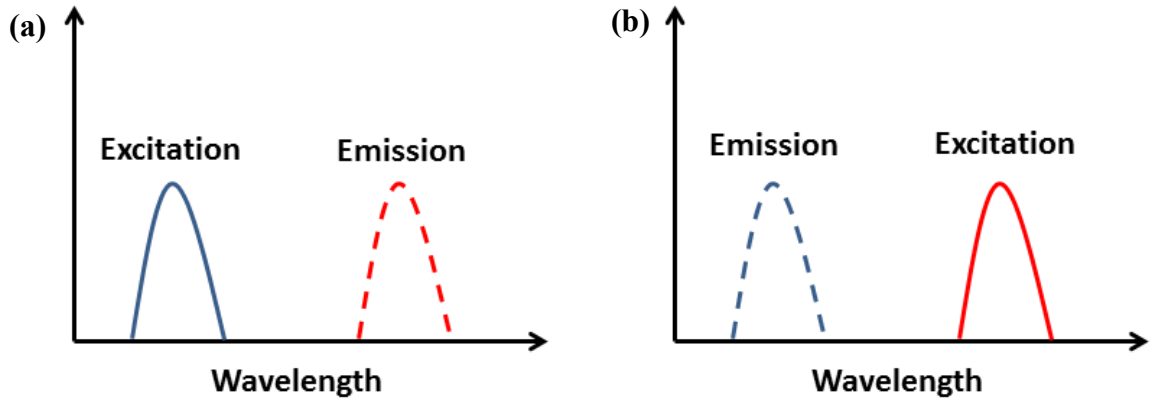

Figure 3 Schematic illustrations of (a) Stokes and (b) anti-Stokes shift emission. The solid and dotted line refer to the excitation and emission spectra respectively.

On the other hand, anti-Stokes shift is referring to the situation, where the emitted photons possess higher energy than the excitation photons. This type of optical phenomena can also be observed in some Ln^{3+} ions-doped nanocrystals. In fact, upconversion luminescence (UCL) can be realized in various combination of Ln^{3+} ions, such as yttrium (Y^{3+}), ytterbium (Yb^{3+}), neodymium (Nd^{3+}), erbium (Er^{3+}), holmium (Ho^{3+}) and thulium (Tm^{3+}) ions. Yb^{3+} and Nd^{3+} ions can act as sensitizers, because they have large absorption cross-section at NIR regime and hence they are able to harvest the NIR photons and transfer to the neighboring activator ions for UCL, for example Er^{3+}, Tm^{3+} and Ho^{3+} ions. In addition, these ions present ladder-like energy levels (Figure 4) and this implies that the sequential absorption of NIR photons may facilitate UCL.

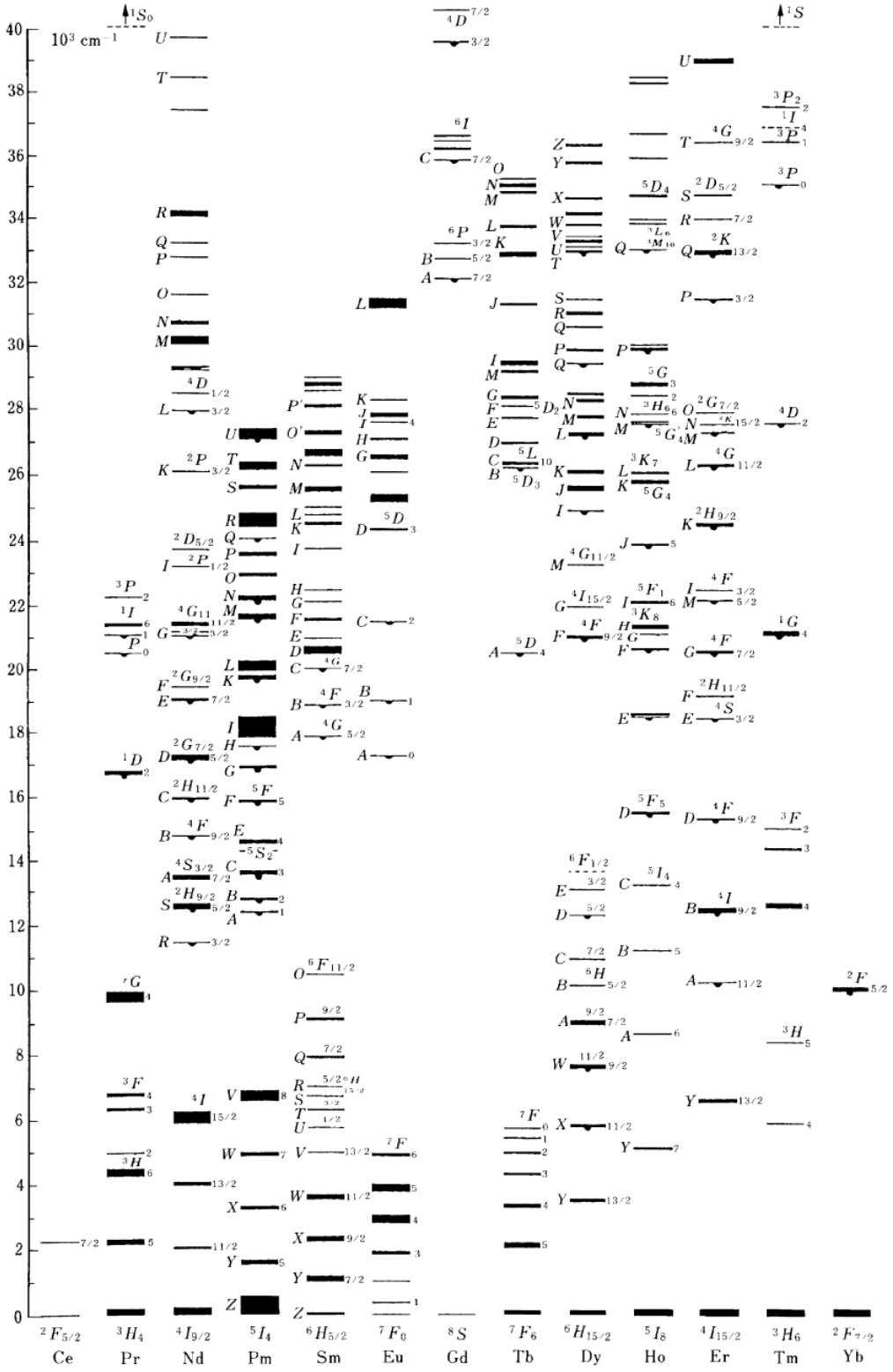

Figure 4 Energy level diagram of various types of Ln elements.[1]

1.2 Upconversion

By definition, UC is a non-linear optical process that involves the sequential absorption of lower energy photons and conversion to higher energy photons.[13] UCL should be discriminated from conventional two photon absorption (TPA) emission because conventional TPA requires ultrashort pulse lasers to pump the material for emission while Ln^{3+} ions-based UCL only requires a continuous wave diode laser. Owing to its non-linear nature, this process demonstrates power dependent emission intensities at different excitation powers. It can be described by using the following equation [14–16] and it is also known as the power law for UC,

$$I_{UC} \alpha P^n \qquad (1)$$

I_{UC} is the upconversion intensity, P is the excitation power and n is the number of photons involving in the UC process. As a result, n can be estimated by calculating the slope in a log-log plot of the emitted intensities and the pumping powers.

1.2.1 Excited State absorption

Figure 5a shows a simple three level system to describe the excited state absorption (ESA)[17–19], the activator ions absorb the incoming NIR photons and convert them into higher energy photons. The single Ln^{3+} ion should present large absorption

and radiative emission cross section; therefore the ions can be pumped to higher energy levels and returned to ground state for emission. The energy levels of the Ln^{3+} ions should also match the excitation source in order to observe high efficiency ESA, such as Er^{3+}, Ho^{3+}, Nd^{3+} and Tm^{3+} ions.[20–24] However, ESA is not popular owing to their relatively low radiative efficiency compare to sensitizer-activator ion UCL systems.

1.2.2 Energy transfer upconversion

The energy transfer upconversion (ETU)[25–27] (Figure 5(b)) is a type of sensitizer-activator UCL system, the key difference between the ETU and ESA is the doping of sensitizer ions, such as Yb^{3+} ions, into the host matrix. This system utilizes the large absorption cross section of the sensitizer ions to harvest the NIR energy and subsequently transfer to the neighboring activator ions for emission. Owing to the energy transfer, one should observe a rise time interval during temporal characterization of the UCNCs. The ratios of the sensitizer to activator ions is crucial to realize efficient ETU, because the ratios dictate the separation of the between the two types of ions. For example, previous reports indicated that the optimal doping concentration of Yb/Er system is around 20:2 or 18:2.[16] Owing to the improved UC efficiency, many UCNCs were designed and synthesized based on the ETU mechanism.[28–33]

1.2.3 Energy migration-mediated Upconversion

Thanks to the advances in UCNCs synthetic methods, the core-shell structure can be readily prepared by using coprecipitation or thermal decomposition route. The core-shell structure was also found to be useful to passivate the surface volume defects; hence the emissions in the visible regime are enhanced by such passivation.[34] The discovery of the shell coating technique gives rise to the realization of energy migration-mediated upconversion (EMU)[35–37] (Figure 5(c)). The EMU requires of four types of ions, the sensitizer, accumulator, migrator and activator ion. The sensitizers absorb the NIR energy and resonant the accumulators in the core region. After that, the energy is transfer to the migrator via hopping to the shell region. The activator at the shell region finally transit downward to emit radiative energy. One of the special features of EMU is the spatial separation of ions in the core and shell region; hence the freedom for the choice of activator ions is large. In addition, the system allows more flexibility in modulating the Ln^{3+} ion compositions and concentrations with minimal luminescence quenching. This mechanism also enabled the shifting of the excitation wavelength from 980 to 808 nm by spatially separate the Yb^{3+} and Nd^{3+} ions[38–41] and realization of up-and downconversion in a single UCL system.[42] As a result, this fostered many novel UCNC structures in terms of excitation and emission characteristics.

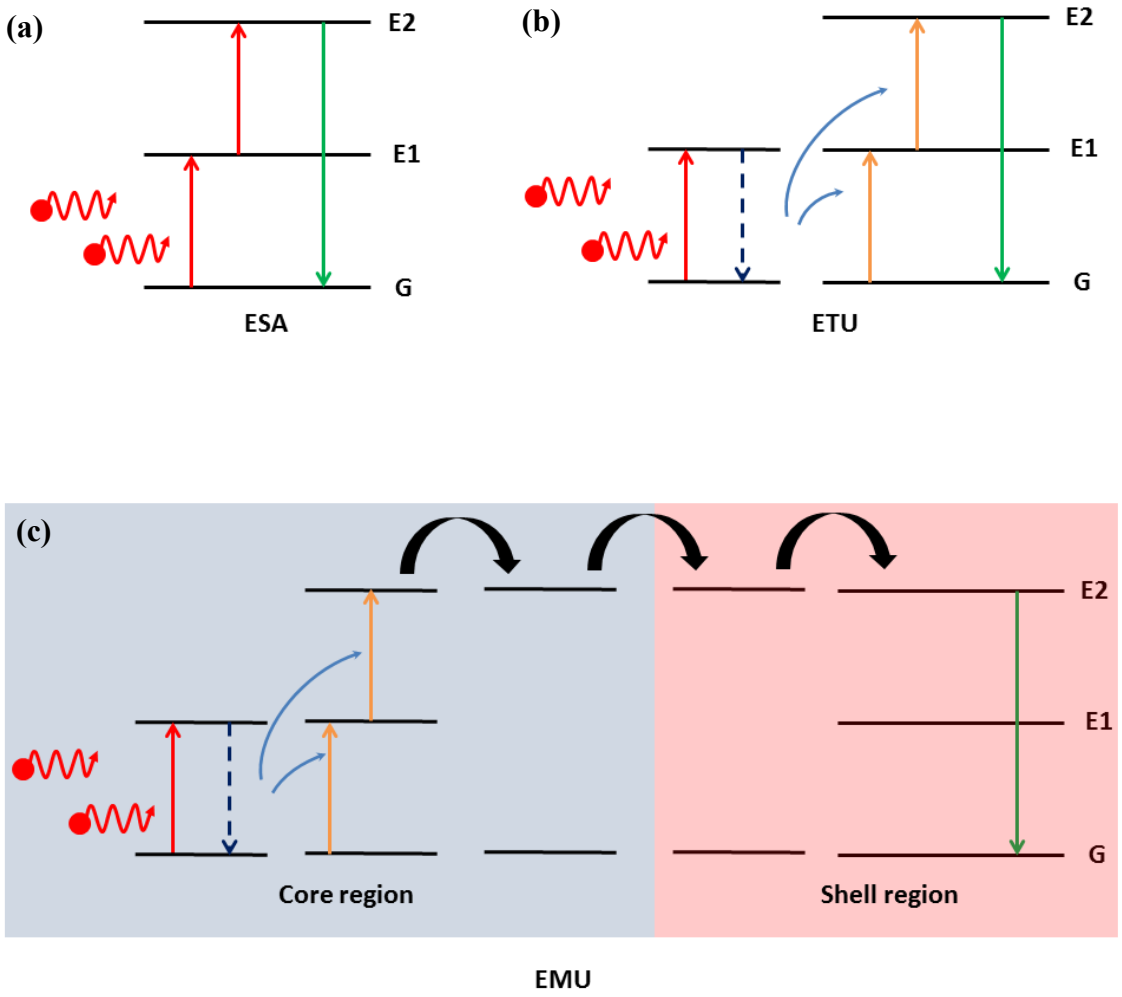

Figure 5 Simplified energy level schematic diagrams to illustrate (a) ESA, (b) ETU and (c) EMU system.

1.3 Upconversion nanocrystals synthesis techniques

The key components in a typical nanocrystal synthesis are precursors, surfactants and the solvents. Surfactants are also referred as capping or passivating ligands. The precursors are usually charged metallic salts or centers of complexes while the solvent is selected based on the nature of the metal precursors. The choice of surfactants is also critical because it controls the growth rate, size and particle solubility in other solvents. The solubility property can not only prevent particle aggregation but also enable post synthesis surface modifications. The fundamental theory for the formation of the nanocrystals can be explained briefly by using the La Mer model (Figure 6).[43,44] After the injection of the reaction precursors, the concentration of the seeds will abruptly increase because the concentration of the precursors exceeds the nucleation threshold. After that, nucleation occurs and the growth of the seeds into nanocrystals as a consequence of the high temperature. Eventually, an equilibrium state (saturation) will be attained after prolong heating. To date, the common synthetic routes to obtain fluoride-based UCNCs are hydrothermal, coprecipitation and thermal decomposition. The fluoride host is preferred because it possesses low phonon energy, which can maximize radiative emission.[16] The three routes have their unique features in the precursors, procedures, equipment and reaction temperatures.

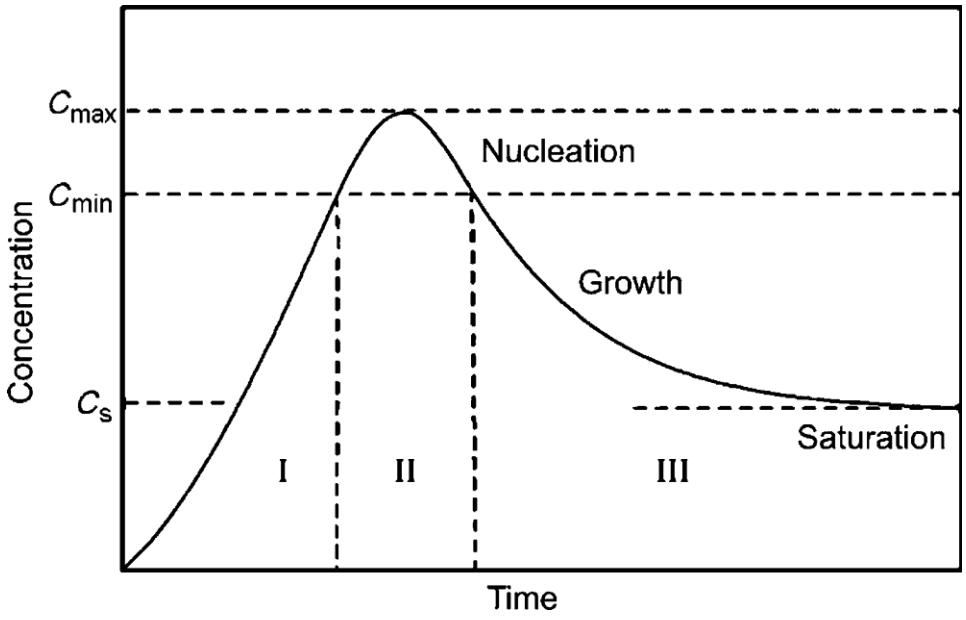

Figure 6 Plot of the La Mer model for the growth of nanocrystals.[44]

1.3.1 Hydrothermal

Hydrothermal synthesis is a relatively simple synthetic strategy because it involves the mixing of the reaction precursors and transfer of the mixture to a Teflon-lined autoclave for chemical reaction under certain temperatures. The autoclave can maintain a high pressure environment that promotes the growth of the seeds into nanocrystals. It is important to note that the nucleation and growth process is not separated in this synthetic route. The reaction precursors are usually water soluble chlorides or nitrates in ethylene glycol medium.[45–48] In addition to the precursors, various kinds of capping agent had been used for hydrothermal, such as, polyacrylic acid (PAA), polyethylene glycol (PEG)[49], poly(ethyleneimine) (PEI)[50] and oleic acid (OA)[51]. These are common capping agents for various hydrothermal synthesis

experiments to control shape and size. As a result, one-step hydrothermal and the liquid-solid-solution (LSS)[51] based hydrothermal synthesis had been developed for hydrophilic and hydrophobic UCNCs with different compositions. The one-step hydrothermal requires no post synthesis treatment for hydrophilicity while the LSS technique should follow the protocols for hydrophilicity similar to that in coprecipitation and thermal decomposition.

1.3.2 Coprecipitation

The coprecipitation route for synthesizing hydrophobic UCNCs in a binary solvent system is well documented by Wang et. al.[52] OA and 1-octadecene (1-ODE) are used as the stabilizer and solvent for the reaction respectively, while the precursors are chlorides or acetates salts to avoid degradation of the medium. The coprecipitation of the Ln^{3+} oleate complex in the presence of cationic hydroxides and ammonium fluoride manifest the principle of the synthesis of various types of oleate capped UCNCs. Since OA and 1-ODE are prone to oxidation, the synthesis requires a vacuum/inert gas switching system for the protecting the reaction medium at high temperature. As a result, a dual vacuum/gas manifold is essential for the degassing and inert gas protection for the reaction medium. The merit of this method is the freedom for precise control of the reaction precursors and the nucleation condition. Therefore, this route can yield different morphologies and sizes of oleate capped UCNCs with narrow size distributions. Moreover, it allows the injection of the core UCNCs for epitaxial shell coating. The as-prepared oleate UCNCs can be readily dispersed in non-polar solvents,

such as cyclohexane, toluene and chloroform, for further surface modifications.[53–56]

1.3.3 Thermal decomposition

The thermal decomposition synthesis of Ln^{3+} ions-doped UCNCs is firstly demonstrated by the Yan's group.[57,58] The strategy is similar to the coprecipitation route with respect to the setup and chemicals, except that the Ln^{3+} precursors and cation salts are organometallic compounds. The precursors decompose at elevated temperature in the presence of high boiling point solvents, such as OA, 1-ODE and tri-n-octylphosphine oxide. The selection of the solvents, concentration of precursors, reaction temperature and time are influential variables that determine the size distribution, crystallinity and physical properties.[59] In a later work, Yi and Chow refine the technique that by using OA and oleyamine (OAM).[60] The size of the UCNCs can be synthesized to be sub-10 nm. As a result, different new combinations of ligands and medium were reported in different UCNCs systems using OA/OAM, OA/OAM/ODE or OAM only.[61–63] The introduction of OAM to the synthesis provided new opportunities to synthesize ultra-small UCNCs to meet the need for bioimaging applications.

1.4 Ligand exchange technique for hydrophilicity

In addition to the one-step hydrothermal synthesis technique, the other two synthetic routes require surface ligand treatments for hydrophilicity in order to meet the demand for biological applications. There are many useful surfaces for biological conjugations, for example, carboxylic acid, amine-, thiol- surfaces and so on. The following diagram summarized different surfaces and strategy for biological conjugations (Figure 7).[64–66] There are mainly four categories for bio-functionalization of the hydrophobic UCNCs, including ligand attraction, ligand engineering, surface polymerization and layer-by-layer assembly.

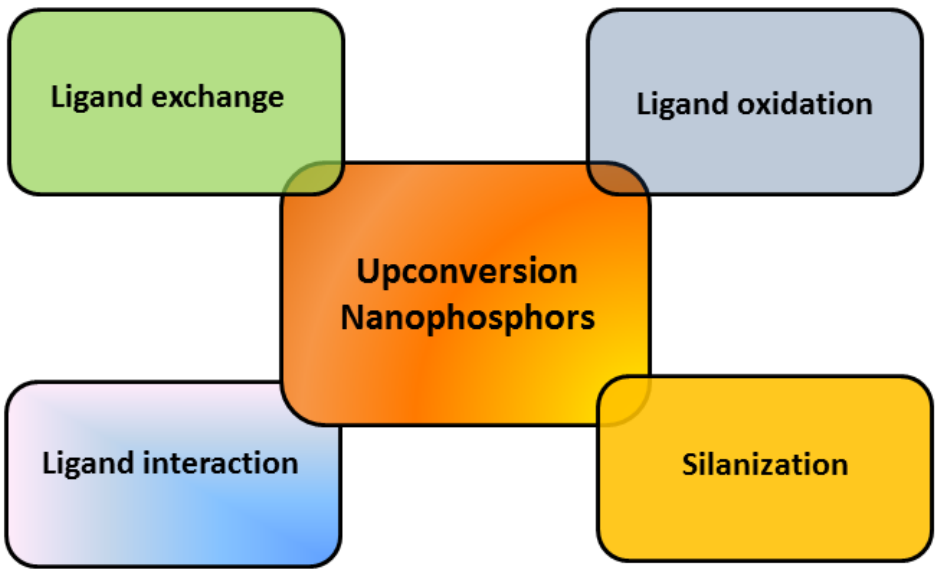

Figure 7 Summary of different pathways for bio-functionalization.

1.4.1 Ligand exchange

The as-prepared UCNCs from the OA-based media are not suitable for biological application due to their hydrophobicity; therefore the oleate can be exchanged by a hydrophilic ligand by stringent choice of type, temperature, pH, solvent and amount. The solvent should be more energetically favorable to the new than the original ligand and the amount of ligands should be in excess, these factors can assist the displacement of the original ligand by the new ligand. Moreover, multidentate ligands are more favorable over monodentate ligands because of the higher coordination sites of the ligand to the UCNCs.[64] In another situation, the oleate groups can be protonated and removed from the as-prepared UCNCs by using acid treatment, resulting in a ligand-free surface.[31,67,68] Ligand-free UCNCs can readily disperse in water owing to the vast amount of surface Ln^{3+} charges. However, previous report indicated that the ligand-free UCNCs may induce cell death by inducing adenosine triphosphate deprivation while the viability of the cells improved by coordinating PAA to the surface.[69]

1.4.2 Ligand oxidation

In addition to removing the oleate group, the oleate group can be oxidized to form other types of acidic surface to render the UCNCs in water. The double bond at the ninth and tenth carbon atom in the oleic acid can be oxidized by using Lemieux–von Rudloff reagent to become azelaic acid and nonanoic acid.[70,71] Such reagents are

essentially a mixture of permanganate and periodate ions in stoichiometric amounts. They convert the surface oleate into azelaic acid via a three-step reaction of the double bond, there are two stages of oxidation reaction by the permanganate and periodate sequentially. Another approach to oxidize the oleate group is ozonolysis.[72] The oxidation by ozone produces intermediate aldehyde groups and further oxidation by using mixture of hydrogen peroxide and acetic acid can convert the surface into carboxylic acids.

1.4.3 Ligand interaction

Ligand interaction is another surface modification strategy that aims to utilize the hydrophobic-hydrophobic interaction of the tail of the new ligand to the oleate group. Therefore, the new ligand should be an amphiphilic polymer comprising of a hydrophobic tail and hydrophilic head, the tail can conjugate to the oleate and the head contribute to the stability in water. Two common examples are OAM-PAA[73] and mixture of OAM-isopropylamine (IPA), the OAM tail interacts with the oleate group while PAA or IPA can provide stabilization in water. This method is relatively simple because it allows the new ligand to react directly with the oleate group, but one should note that the hydrophobic part of the ligand is sensitive to the chemical or biological microenvironments. Hence, the stability at high ionic strength and variable pH environment may be a critical issue during biological applications.

1.4.4 Silanization by growing silica shell

The growth of a silica shell can also endow the UCNCs hydrophilicity and the stability of silica coated UCNCs are being studied extensively. There are two ways to grow silica shell on the surface of UCNCs: the reverse emulsion method[74–77] and modified Stöber method.[78–80] The reverse emulsion method can be performed in organic phase in the presence of surfactants, ammonia and tetra-alkylorthosilicates (TEOS). The surfactant and ammonia create a hydrophilic zone for the polymerization of TEOS to form a stable silica shell. The ratio of surfactant to ammonia and amount of TEOS controls the resultant silica shell, the resultant silica-coated UCNCs can be disperse in ethanol or water. The Stöber method requires hydrophilic UCNCs and Polyvinylpyrrolidone (PVP) in ethanol, PVP chelates the UCNCs surface and thus controls the formation of the silica shell on UCNCs. The as-prepared silica-coated UCNCs can be easily functionalized with different functional groups, such as, amine, thiol and epoxy, because of the widely available functionalized silanes. However, it is worth to note that the use of surfactant in the reverse emulsion process will affect the colloidal stability of the final silica-coated UCNCs. As a result, the washing steps should be more stringent to ensure complete removal of the surfactants.

1.5 Biological applications based on upconversion nanocrystals

The advance in synthesis, surface modifications and conjugations technique had provide the opportunity for UCNCs to prove their abilities for future nanoprobe-based biological applications. In fact, UCNCs spanned a spectrum of biological applications; the following session will review the recent advances of multimodal bioimaging, biodetection assays, phototherapies and drug delivery.

1.5.1 Multimodal bioimaging

The inherent imaging modes of UCNCs are UCL, magnetic resonance imaging (MRI) and X-ray imaging. This is due to the physical properties of the Ln^{3+} ions, for instance the magnetism of Gd^{3+} ions and X-ray absorption ability of the series of Ln^{3+} ions.[81] UCL shows advantages over conventional dyes in terms of chemical stability, photostability, narrow emission bands and long-lived emissions. The high stability stemmed from the shielding of outer full-filled 4s subshell while the excellent emission properties are due to the transitions in the inner 4f-subshell. To meet the demand for multimodal bioimaging, functional molecules or groups are conjugated to the UCNCs to form nanocomposites. Additional imaging modes, such as positron emission tomography (PET), single photon emission computed tomography (SPECT), ultrasound imaging (USI) and photoacoustic imaging (PAI) are combined with the fundamental imaging modes to demonstrate multimodal bioimaging.[82,83] The key strength for

multimodality system is the compensation of the weaknesses of individual modes within a system. Moreover, the injection of a single compound for multimodal imaging can avoid the unexpected side effects due to injection of multiple contrast agents.

The advantages of UCL imaging include high spatial resolution and sensitivity, however the imaging depth is shallow, hence MRI is a good option to compensate such weakness. MRI offers high resolution, non-invasive and three-dimensional (3D) structural and functional information. For instance, Zeng et al. showed that $BaGdF_5$:Yb/Er UCNCs were able to fabricate bimodal UCL/MRI system for imaging of HeLa cells.[84] The proof of concept work indicated the potential for further small animal imaging. One important criterion for *in-vivo* imaging application is PEGylation; PEGs are stable, inert and biocompatible. Moreover, the two ends of PEG molecules can be modified with different functional groups for bioconjugations and adaptations to microenvironments. As a result, the PEG-capped UCNCs can be stabilized even at high salt concentrations and various types of solvents in addition to water. PEGs can also passivate the surface by preventing non-specific binding to molecules and increase the circulation time in the blood circulation system by masking the UCNCs to the immune system. Liu et al. reported a PEG modified $NaGdF_4$:Yb/Er UCNCs with antibody targeting function to image intraperitoneal and subcutaneous tumors.[56] Apart from the imaging results, the role of target function of antibody was shown; the MRI contrast at the tumor was greatly enhanced by comparing the imaging results with that of bare PEG modified UCNCs. The UCNCs was cleared via excretion and urination after 1.4 day of circulation.

In addition to bimodal UCL/MRI systems, radioactive isotopes can be conjugated to the UCNCs for PET and SPECT imaging. These types of imaging modes had been established in the hospitals for revealing the functional information of the organs. Li's group presented a systematic study of fluorine-18 (^{18}F) decoration on various types of Ln^{3+} ions-doped UCNCs for UCL/PET imaging.[85] Owing to the strong binding affinity of the surface Ln^{3+} ions to ^{18}F, a high loading yield was recorded by using sonication for 1 min. The ^{18}F-loaded $NaYF_4$:Yb/Tm UCNCs were used for the PET scanning and the scanning revealed a real time biodistribution of the UCNCs. Lymph node imaging was performed at the right paw of mice to validate the PET imaging ability. SPECT and PET also both utilize radioactive isotopes for imaging purpose, but the isotope in SPECT possesses longer half-life of around 6 h. Li's group had done work on UCL/SPECT bimodal imaging by using EDTMP capped ^{153}Sm-$NaLuF_4$:Yb/Tm UCNCs for blood pool imaging.[86] The radioactive tracer atomic radii is small, hence it can be easily doped into the UCNCs without dissociation. The carotid artery, vertebral arteries and superior epigastric artery of the mice was imaged after 30 min circulation. A control experiment was also prepared by using citrate capped UCNCs and EDTMP-^{153}Sm complexes, the results suggested that EDTMP ligand but not the dissociated EDTMP-^{153}Sm moieties contribute to the increased circulation time of the UCNCs. In another work, they studied the biodistribution of the UCNCs by using PEG passivated ^{153}Sm-$NaLuF_4$:Yb/Er UCNCs.[87] The metabolism of the UCNCs was changed by using their reported method from liver/spleen to kidney/urine pathway.

Tri- or higher modalities were also demonstrated by using other works. PEG-capped $BaGdF_5$:Yb/Er UCNCs were synthesized for tri-modal UCL/MRI/X-ray computed tomography (CT). The simple design can integrate three modes in a single-phase material system; it featured low-cost and easy implementation. The X-ray CT is more powerful than the ordinary X-ray imaging because of the ability to render 3D volumetric information of organs. Recently, Liu et. al reported a Indocyanine Green (ICG) decorated $NaYF_4$:Yb/Er@$NaYF_4$:Yb@$NaNdF_4$:Yb@$NaYF_4$@$NaGdF_4$ multi-shell UCNCs for PAI/MRI/UCL imaging.[88] ICG is a FDA-approved dye that can exhibit strong PA signal. In addition to typical UCL and MRI modes, the PAI capability of ICG was shown to be high because PA signal was detected from the concentration of 1 μg ml^{-1}. Their PAI results indicated that the UCNCs were capable of imaging the small blood vessels under skin with a distance range from around 4.8 to 10 mm. Recently, Rieffel et. al reported about the hexamodal imaging using porphyrin-phospholipid (POP)-coated $NaYbF_4$:Tm@$NaYF_4$ with ^{64}Cu.[89] The composition of the system was not complicated with respective to the number of modalities of the composite; the modalities included UCL/fluorescence/PAI/PET/X-ray CT/Cerenkov luminescence. It was expected to be useful for the development of hyper-integrated imaging systems.

From the above discussion, one should realize the importance of clearance after bioimaging despite the number of modes. Naked surface UCNPs were known to be highly toxic to cell because they induced adenosine triphosphate (ATP) deprivation. After PAA modification, the toxicity reduced significantly to acceptable level.[69] As a result, shell capping and surface passivation techniques are essential to reduce the

toxicity effect and facilitate efficient clearance of the injected UC probes from the *in-vivo* model. In general, PEGylation and PAA-coating of UCNPs had been shown to suppress the cytotoxicity in numerous proof-of-concept UCNPs and related composite structures. Xiong et. al presented their in-depth *in-vivo* distribution and toxicity of the PAA-coated NIR-NIR UCNPs using mouse model.[90] After injecting 15 mg/kg of UCNPs, they were uptaken and accumulated at the spleen and liver. The body weight, histological, hematological and biochemical analysis were used as the standard to survey the toxicity in a period of 115 days. Furthermore, they showed that the UCNPs were cleared via intestinal tract through hepatobiliary transport after 115 days. In another study, the 5.1 nm and 18.5 nm PEGylated-UCNPs clearance were studied by collecting the urine and feces of the injected mouse. They estimated the half-life of the UCNPs was around 8.2 days in fecal excretion and 1.4 days in renal pathway, respectively.[56] A more recent study utilized citrate-stabilized four-modal UCNPs probe for the observation of angiogenesis,[87] the X-ray CT result suggested the transport of the UCNPs via bile flow from the gall bladder but not in urinary bladder. This supported the main excretion of the UCNPs from gall to the intestine. The above discussion showed the UCNPs can be effectively cleared from the *in-vivo* model by PEGylation, PAA or citrate modification.

1.5.2 Biodetection

Before the reviewing the luminescent biodetection systems, it is critical to clarify the role of luminescent detection assays. The conventional picture of

biodetection is given in Figure 8. The luminescent detection is responsible for the readout part in the flow of the detection, hence the LODs for luminescent detections only describes the LOD of the readout. The LOD for the whole detection process is affected by numerous factors, for example sample purification, handling techniques and the detection media.

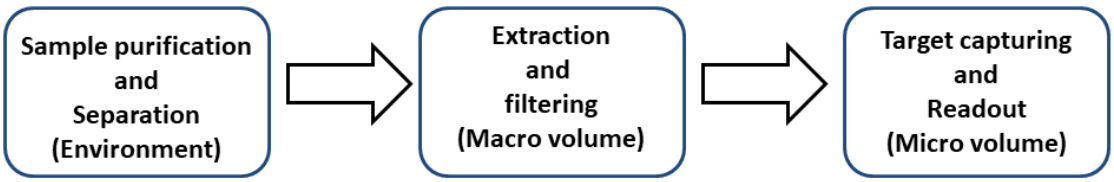

Figure 8 General picture of the flow of detection.

Homogeneous assays are simple, fast and usually performed in a liquid phase without the need for laborious washing processes.[36] Zhang et al. designed an antibody conjugated upconversion nanobarcode (UPNB) and secondary antibody-coated microspheres for multiplexed detection assays.[91] The conceptual detection system utilized the specific binding of the mouse IgG antibody modified microspheres and the IgG-modified UPNB. Wu et. al used a competition detection assay for the simultaneous detection of aflatoxin B1 (AFB1) and ochratoxin A (OTA) in food samples.[92] It involved the use of antibody modified magnetic nanoparticles and $NaYF_4$:Yb/Tm (Er) UCNCs. The role of the magnetic nanoparticles is to separate the unconjugated UCNCs, this purification process was comparatively simple because of magnetic separation. The LOD for AFB1 and OTA was around 0.01 ng ml^{-1}. On the other hand, some detection designs may apply the LRET phenomena to achieve changes in emission wavelengths

or intensities, those changes act as a reporting signal to indicate the presence of the analytes. The H7 Avian flu virus was detected by using amine-functionalized UCNCs and AuNPs.[47] The UCL emission was absorbed by the AuNPs in the presence of the virus oligos. The extent of the quenching of the UCL signal was used to quantify the concentration of the virus oligos. The sensor was able to detect the virus oligo in 2 hours with a LOD of around 7 pM. Moreover, the specificity test indicated the high specificity of the sensor towards flu virus oligo. UCL homogeneous assays were also used for environmental pollutant detections, such as mercury ($MeHg^{+}$),[93] copper (Cu^{2+}) and cyanide (CN^{-}) ions. The presence of these pollutants in water will kill marine and ultimately affect human beings. The detection of Cu^{2+} ions in water had been demonstrated by using mesoporous silica coated UCNCs.[94] Rhodamine B hydrazide was used as a probe to capture Cu^{2+} ions. The ions quenched the UCL to indicate the presence of the ions. The CN^{-} ions were probed by using the conjugated iridium (Ir) complex on $NaYF_4$:Yb/Ho UCNCs.[95] The green UCL was suppressed by the Ir complex during detection of CN^{-} ions, while the red emission was not affected by the detection. Therefore, the red emission was used as an internal standard for ratiometric detection. The benefit for such detection is the cancellation of the environmental factors that affect the detection.

Heterogeneous assays are well known for their high sensitivity but tedious washing steps are essential to ensure no contaminations.[36] The detection of lethal viruses and disease markers detections normally requires high sensitive assays (or high LOD), because this can decrease the death rate of patients by early diagnosis. The

detection of β subunit of human chorionic gonadotropin (β-hCG) was performed by utilizing the antibody-antigen interaction of β-hCG in a microplate with $LiLuF_4$ UCNCs.[96] The fabrication of the detection platform started with the avidin modification of the UCNCs followed by the addition of the biotinylated antibody. The increase in the UCL signal was used as the reporting signal for quantifying the β-hCG molecules because the unbinded UCNCs were washed away from the microplate. In addition, the heterogeneous assay indicated a LOD of 3.8 ng ml^{-1}, which is comparable to the β-hCG concentration in the serum of normal humans. Apart from proteins, UCL detection technique can also be applied to detect bacteria in food, for instance, Wu et. al developed a multiplex detection platform for simultaneous detection of three pathogenic bacteria (*Staphylococcus aureus*, *Vibrio parahemolyticus*, and *Salmonella typhimurium*) by using $NaYF_4$ UCNCs doped with Tm, Ho or Er and magnetic nanoparticles (Fe_3O_4 NPs).[97] The recognition probes were composed of different specific sequences of aptamers on the Ln^{3+} ions-doped UCNCs. On the other hand, the Fe_3O_4 NPs were conjugated with complementary DNA (cDNA) oligo sequences to hybridize with the aptamer partially. After the mixing of the UCNCs-aptamer probe-Fe_3O_4 with the bacteria, small section of the aptamer probe captured the bacteria and forced the dissociation of the cDNA. Therefore, magnetic separation could be used to collect the excess UCNCs-aptamer probe-Fe_3O_4 for quantifying the bacteria concentration indirectly. The use of magnetic separation enhanced the sensitivity and the assay reported a range of LOD from 10-25 cfu ml^{-1}.

1.5.3 Phototherapy and drug delivery

The UCL emissions are not only use for imaging and detection purpose but also trigger therapeutic systems. The term "smart" is used to describe the stimuli-responsive systems, because most of the reported drug delivery systems were able to response to some external stimuli, such as pH, temperature and light.[98] Lin's group presented a substantial amount of reports on different drug delivery systems.[99–101] For example, Wang et. al presented the hollow structured microspheres with UCL property as drug carriers.[102] The hollow structure enabled a high loading capacity for the anti-cancer drug Doxorubicin (DOX). The microspheres exhibited a pH dependent drug release profile, in which the drug release was monitored by using UCL. In a later work, a more advanced smart system which exhibit dual response to temperature and pH was reported by Zhang et al.[103] A layer of mesoporous silica shell was grown on the UCNCs; the resultant csUCNCs were linked to a pH and temperature sensitive co-polymer. Moreover, the copolymer possessed a reversible change at low or high pH and temperature, the swelling and de-swelling state of the copolymer can control the release of the drug at tumor sites.

Apart from controlled release, the UCNCs are enabled with therapeutic functions by conjugating with some light responsive species. Phototherapy is divided into photodynamic therapy (PDT) and photothermal therapy (PTT),[104–107] the former relies on the generation of reactive oxygen species (ROS) to increase cytotoxicity for inducing cancer cell death while the latter kills cancer cells by elevating temperature.

The phototherapy process was triggered by NIR and the UCNCs emit UCL to transfer the energy to the photosensitizer to produce ROS. Wang et al. presented the use of Chloin e6 (Ce6) for PDT.[108] Apart from probing the PDT efficacy for destroying tumors, clearance of the PDT agent was also an important issue. They showed that the UCNP-Ce6 composite was cleared from the mouse body after PDT for 1-2 months. The concept of stimuli-responsive system was also applied in advanced PDT scheme. Wang et. al. conjugated the pH responsive dimethylmaleic acid (DMMA) groups to the UCNP-ce6 composite for pH-sensitive PDT.[109] They also utilize the MRI ability of the Mn^{2+} ions-doped UCNCs to monitor the PDT process. On the other hand, PTT can be triggered by NIR radiation and this also matches the excitation of UCNCs, some nanomaterials are known to demonstrate photothermal property, such as silver and gold. Dong et al. fabricated csUCNCs with a nano silver as shell layer for PTT.[110] The absorption maxima of the silver layer were tuned to 980 nm to match the absorption characteristic of UCNCs. Localized heating effect was induced in the cancer cells upon 980 nm laser excitation. The cancer cells were killed after 20 min irradiation. In addition to silver and gold, graphene oxides was a new class of nanomaterial for PTT. Zhang and co-workers combined the PDT and PTT effect by fabricating a UCNP-based composite consisting of the photosensitizer zinc phthalocyanine and graphene oxide.[111] The combined photothermal strategy showed a synergistic effect, which resulted in improved therapeutic efficacy.

1.6 Conventional methods for detection of viruses

PCR and ELISA are the conventional methods for detecting the presence of viruses in the sample. However, the detection principle and mode of the two methods are different. RT-PCR is a variant of PCR, which involves the reverse transcription of virus RNA to cDNA before polymerase amplification reactions. In fact, the amplification is due to the presence of the DNA polymerase and primers. The polymerase is a type of enzyme that replicates the DNA in cells during cell divisions. In addition to the polymerase, the amplification also requires a primer; it acts as a template for the initiation of the reaction. These chemicals are mixed together and placed in a thermocycler for amplification reaction. The reaction time depends on the required number of gene copies hence the amplification usually takes several to tens of hours. It should be noted that RT-PCR belongs to a type of qualitative PCR method; hence the number of gene copies cannot be directly estimated from the result. Gel electrophoresis is routinely performed for separation and analysis of the amplified DNA, this test can also justify the size of the DNA molecules. Since the developments in the 1980s, PCR techniques had been regarded as a standard clinical diagnostic method for DNA sequencing, gene cloning and other manipulations.[112–114] Furthermore, the quantitative polymerase chain reaction (qPCR) is a real time amplification technique, which can monitor the amplification by using fluorescent dyes. The number of gene copies in the sample can be quantified by the comparing with the calibration curve.

Apart from PCR technique, ELISA is also a well-recognized clinical technique which detects the presence of viruses by using antibody-antigen interaction. It is a technique for detection and quantification of specific proteins. There are different formats of ELISA, for example direct, indirect or sandwich ELISA.[115–117] Various types of formats are characterized by their way to capture and detect the target antigen, it should be noted that each format exhibits different degree of specificity, sensitivity and speed. In the simplest case, the antigen of a particular sample is immobilized on a microwell plate followed by the addition of the detection antibody. Notice that the detection antibody is conjugated to an enzyme. After that, an enzyme substrate is added to produce a change in the assay. The change can be recorded in the form of absorbance or fluorescence or electrochemical signals. Nowadays, ELISA kits and services are widely available from the suppliers and clinical laboratories; hence the cost for ELISA is lower than that of PCRs.

1.7 Luminescence resonance energy transfer

One of the important principles that manifest luminescent biodetection is the LRET. The commonly known fluorescence resonance energy transfer (FRET)[118] was first described over 50 years ago, but it was used in biomedical research and drug discovery today. It is essential to differentiate the difference between FRET and LRET because FRET indicates a shorter lifetime than that of LRET. Despite the slight difference in definition, the theory of FRET is still valid in LRET. Basically, LRET is a distance dependent process that requires spectral overlapping of the phosphor (energy donor) and quencher (energy acceptor).[119] Organic dyes and semiconductor quantum dots and upconversion nanoprobes are frequently used as the energy donor while AuNPs,[120–122] commercialized Lowa Black dark quenchers and grapheme oxides are reported candidates for absorbing the energy from the donor.

The LRET[123] process is initiated by the incident photons and subsequently the emitted photon energy from the donor is transferred to the acceptor as follow,

$$D + h\nu \rightarrow D^*$$

$$D^* + A \rightarrow D + A^*$$

$$A^* \rightarrow A + h\nu'$$

D represents the donor, D* represents the excited donor, A represents the acceptor, A* represents the excited acceptor and $h\nu$ represents radiative/non-radiative energy. The LRET process results in a decreased luminescent intensity of the donor accompanies by a change in emission lifetime. The change in lifetime is an important parameter to determine the presence of LRET because simple reabsorption between the donor and acceptor should not induce the change in lifetime. In addition the LRET process can be interpreted in terms of energy levels below,

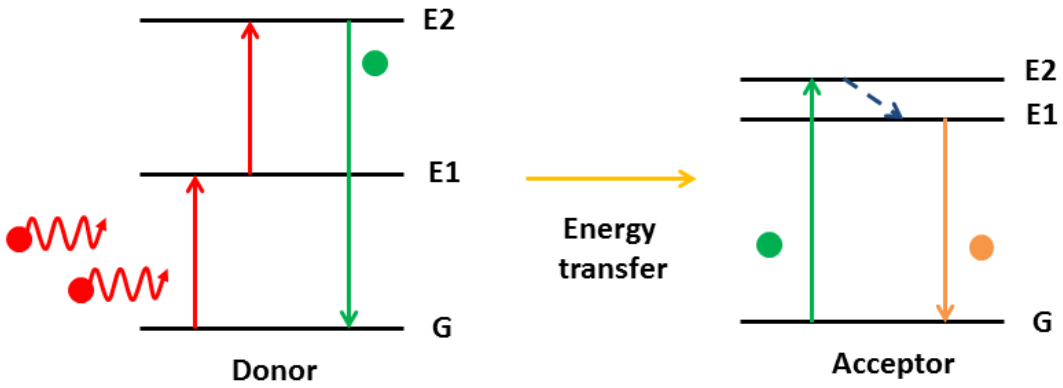

Figure 9 Schematic energy level diagram of LRET. The donor is the Ln^{3+} ion-doped UCNP that emit green emission while the acceptor is a fluorescent acceptor.

Figure 9 serves as an example to explain LRET by using a donor-acceptor LRET pair with UCNP as donor and a fluorescent acceptor. The UCNP is excited by the NIR photons and emit green light, the energy difference of the emitted photon matches that of the acceptor, and hence the acceptor is also excited to emit fluorescence. However, it is important to note that the chosen acceptor is not necessary to be fluorescent, for example AuNPs and dark quenchers. As a result, this provides additional freedom to design different optical detection system by either monitoring the change in emission wavelength or intensities.

There are two important criteria for LRET to occur, firstly, the emission spectrum of the donor should overlap with the absorption spectrum of the acceptor as much as possible. This can ensure efficient energy transfer from the donor to the acceptor. Apart from wavelength, the distance between the donor and acceptor is another consideration to facilitate LRET. The inter-particle distance should be as short as possible, typically the distance for LRET is around 1-10 nm. The relationship of the LRET efficiency (E_{LRET}) and distance r can be expressed as,

$$E_{LRET} = \frac{1}{1+\left(\frac{r}{R_0}\right)^6} \qquad (2)$$

R_o is the critical LRET distance between the donor and acceptor, in which the LRET efficiency is decreased to 50 %. Moreover, R_o is dependent on the luminescence quantum yield of the donor in the absence of acceptor (Q_Y), the refractive index of the

solution (n), the dipole angular orientation of each molecule (K') and the spectral overlap integral of the donor-acceptor pair (J),

$$R_0^{\,6} = \frac{9\ln 10}{128\pi^5 N_A} \cdot \frac{K' Q_Y}{n^4} J \qquad (3)$$

Owing to the high sensitivity of LRET, it is also termed as spectroscopic or molecular ruler. One of the well-known examples is to measure the distance between two active sites on a protein that have been labelled with suitable donor-acceptor chromophore, and therefore monitoring the conformational changes through the amount of FRET between the fluorophores. In this work, the LRET mechanism served as the fundamental for the visualization of the presence of the virus oligo, the change in UCL intensities were recorded as a result of the LRET upon DNA oligo hybridization of the probe and target oligo.

1.8 Motivation of research

Despite the establishment of PCR and ELISA, they are still limited by some drawbacks, such as high operation cost and complicated procedures in PCR, and low sensitivity in ELISA. As a result, these limitations paved the way for the development of luminescent biodetection assays, which are beneficial to the biomedical field by providing an alternative for rapid, simple and sensitive detection assays. In the early stage, downconverting phosphors are used as energy donors; these materials are excited

by high energy UV radiation to emit visible light. It is important to note that DNA oligos exhibit absorption at the UV regime at around 260 nm and literature indicated that UV radiation damaged the DNA backbone of oligos.[124] In addition, the high energy radiation induces severe background fluorescence that contributes to the disturbance of the test and cross-talking to the detectors. UCL assays utilize NIR excitation and this can avoid high energy excitation and pose no damage to the DNA oligos. In addition, the large anti-Stokes shift of UCL provides a clear distinguishing signal for the optical detector for future device implementation. Moreover, the long-lived emission characteristic of UCL from Ln^{3+} ions offers time-resolved detections; therefore the short-lived background disturbance can be filtered easily. The existing homogeneous assays are simple but the sensitivity is not sufficient for ultrasensitive detection of lethal viruses DNA oligos. Moreover, there were a substantial amount of reported biosensors by using different detection schemes to date.[125–129] The developed sensors should be tested with PCR-validated clinical samples in order to valid their performance in future clinical or practical detections.[130]

Owing to the aforementioned problems, this project aims to develop new UCL-based biodetection systems, which is able to provide high sensitivity, low cost and rapid detection of lethal viruses. The inherent merits of UCL are combined with the heterogeneous assay design to maximize the performance of the detection systems by increasing the LOD and specificity of the detection systems. Moreover, the developed nanosensor is tested with PCR-validated clinical sample of viruses to evaluate its feasibility for future DNA sensing applications.

1.9 Scope of work

This work aims to develop a new generation of UCL-based biodetection assays for lethal virus oligo detection by using Ln^{3+} ions-doped UCNCs. Chapter 1 introduces the fundamental knowledge of UCL and LRET. Different synthetic routes for high quality UCNCs will be introduced and reviewed. In addition, comprehensive reviews on the current status of multimodal bioimaging, biodetection, phototherapy and drug delivery are given.

In chapter 2, the synthetic route for Ln^{3+} ions-doped UC fluoride for this work will be introduced; the fundamentals and mechanisms of the one-step hydrothermal and coprecipitation synthesis are presented. Moreover, the chapter depicts the principles of different characterization techniques and instruments.

After that, chapter 3 presents the work on the ultrasensitive detection of Ebola virus oligo using heterogeneous UC nanoprobe/nanoporous membrane system, in which provided new insight to the UCL-based heterogeneous detection. The hybrid composite can not only enhance the LOD of luminescent detection assay but also provide a versatile platform for multi-viruses detection. The novel heterogeneous assay is tested with clinical Ebola virus oligo for future biomedical applications.

The developed hybrid system in chapter 3 is improved and hence fosters the new heterogeneous sandwich detection scheme in Chapter 4. The design is based on two oligo probe modified UC and gold nanoprobes. The csUCNCs were combined with nPS to form the csUCNCs/nPS composite as the platform for the heterogeneous sandwich assay. The complements of the virus oligo are divided into two strands of single strand oligos. The design allows highly specific recognition of virus oligo by hybridizing two sections of single strand oligo probes with the virus oligo. The resultant design is tested with clinical influenza virus oligo validated by PCR.

Finally, chapter 5 concludes the thesis by a brief summary of the works and provides the future development direction of UCL-based detection assays and other biological applications.

2. Methodology

This chapter will describe the routes for synthesis and modifications of UCNCs for biodetection. The one-step hydrothermal synthesis is simple, non-toxic and requires no post synthesis treatment for hydrophilic UCNCs while the coprecipitation synthesis is able to prepare high quality UCNCs with regular morphologies and high quantum efficiency, though surface ligand engineering is needed for hydrophilicity. After that, a series of characterizations were performed to evaluate the physical and chemical properties of the modified UCNCs prior to biodetection.

2.1 Hydrothermal and coprecipitation synthesis

The one-step hydrothermal synthesis of amine-functionalized $BaGdF_5$:Yb/Er UCNCs was realized by using water soluble Ln^{3+} nitrates, because nitrates could be prepared in high concentrations to avoid water in the reaction medium. In addition, barium chloride and ammonia fluoride were used as the cationic and anionic source for formation of the UCNCs. The rational choice of surfactant was essential because it determined the surface and controlled the size of the UCNCs; branched PEI was chosen because it was a multi-dentate ligand with vast amount of amine groups. The above surfactant and precursors were dissolved in ethylene glycol (EG), and then subsequently heated to 190 ^{o}C for formation of UCNCs under high pressure. The selection of reaction temperature was based on the boiling point of EG. The autoclave consists of Teflon-

lined container inside a sealed stainless steel container was used to ensure the pressure for crystallization (Figure 10).

Figure 10 Photographs of the autoclave for one-step hydrothermal synthesis. The white part is the Teflon lining of the container.

In order to improve the morphology, luminescence efficiency and excitation property of the UCNCs, the coprecipitation synthesis was selected to synthesize $NaGdF_4$:Yb/Er@$NaGdF_4$:Yb/Nd csUCNCs. The Ln^{3+} acetates were used instead of nitrates because nitrates degrade the reaction medium. Meanwhile, OA and 1-ODE were used as the surfactant and solvent respectively. OA was able to coordinate the growth for regular morphologies and provide stability in non-polar solvents for further surface modifications. 1-ODE is a high temperature solvent that provides a stable environment for cubic-to-hexagonal phase transition of csUCNCs. Sodium hydroxide (NaOH) and ammonia fluoride (NH_4F) were used as the ion source for the formation of UCNCs instead of sodium fluoride, because this allowed the modulation of the sodium to

fluoride ion ratio for controlled morphologies. The reaction was also degassed and purged by argon to ensure minimal oxidation during the synthesis. Moreover, the dual-gas/vacuum manifold (Figure 11) is selected as the device to control the degassing and purging process because the inclined stopcocks can switch from vacuum to purging state by turning it. The temperature and duration for the high temperature heating at 290 ^{o}C for 1.5 h is to ensure the crystallization and complete cubic-to-hexagonal phase transition. The hexagonal phase of UCNCs is known to emit higher UCL intensity than its cubic counterpart by tens of folds.[131]

Figure 11 Photograph of the dual-gas/vacuum manifold for coprecipitation. The stopcocks are tightened by a spring at the backward side while the four ports can connect to the vacuum pump or inert gas source.

2.2 Characterization techniques

The optical, morphological, phase and surface properties of the as-prepared UCNCs were investigated by different characterization techniques. The surface characterization part played an exceptionally important part of the work because the conjugation of the oligo probes onto the surface of the hydrophilic UCNCs determined the functionality of the detection system.

2.2.1 Electron microscopy

Owing to the small size of the as-prepared UCNCs, transmission electron microscopy (TEM) is essential to reveal the size, phase and compositions. The high voltage electron beam strikes on the carbon grid with UCNCs to give different secondary signals, such as transmitted electrons, diffracted electrons and X-ray. The transmitted electrons are used to observe the morphologies of the UCNCs while the diffracted electrons interact with the samples to give electron diffraction patterns. The patterns are analyzed to confirm the crystalline structures of the UCNCs. The energy dispersive X-ray mode in TEM utilizes X-ray transitions in elements to reveal the type and atomic ratio of different doped ions in the UCNCs.

On the other hand, scanning electron microscopy (SEM) is capable to provide 3D information of the composite samples. The magnification and resolution is inferior

to TEM because of relatively low accelerating voltage. The scanning electron beam strikes on the samples to give secondary electron signal for imaging, the scan speed determines the quality and detail of the resultant images. However, it should be note that prolonged scan time lead to charge up and destruction of samples.

2.2.2 Photoluminescent spectroscopy

The PL properties of the UCNCs and hybridized samples were measured in a commercialized PL measurement system FLS920 from Edinburgh Instruments. The interior and exterior view of the system is shown in Figure 12(a) and (b), respectively. The instrument consists of four sides, in which two sides are connected to the Xenon lamp and NIR lasers separately. The right arm connected to the photomultiplier tube to amplify the emission signal before arriving at the optical detectors while the left arm is not used in this work. 980 and 808 nm diode lasers are chosen as the excitation source because of the absorption cross section of the Yb^{3+} and Nd^{3+} ions. The lasers can be switched to pulse laser mode simply by switching at the modulator for measurement of lifetimes. The samples are measured in liquid state because the drying of the functionalized UCNCs led to the destruction of the surface groups. The changes in surface abruptly affected the emission intensities. As a result, the UCNCs are either dispersed in water or cyclohexane to form a colloidal solution for measurement. However, it should be noted that quartz cuvette is preferable over polystyrene disposable cuvette because cyclohexane will lead to swelling of polystyrene. On the hand, polystyrene disposable cuvette is suitable for measuring the emission spectra in

biodetection samples, because it can ensure no residual UCNCs affecting the UCL intensities.

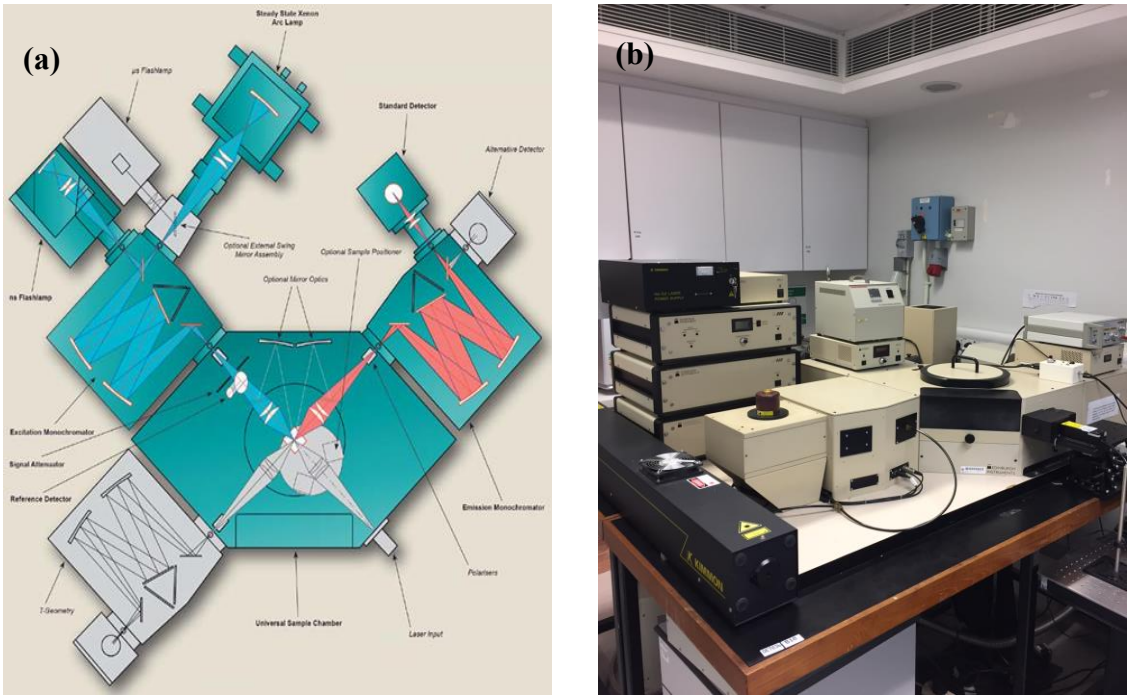

Figure 12(a) Interior view and (b) Exterior view of the FLS920 commercialized PL measurement system from Edinburgh Instruments.

2.2.3 X-ray diffraction

X-ray diffraction (XRD) is an optical technique for determining the phase structures of crystals. The crystalline planes in the UCNCs diffracted the incoming X-ray at different angles; therefore the resultant XRD spectra consisted of diffracted peaks with different peak intensities. The patterns can be subsequently compared with the standard diffraction patterns for composition and phase confirmation. The width of the diffracted peaks represent the average size of the UCNCs, small-sized UCNCs will

result in broader diffracted peaks and vice versa. Apart from the angles, the intensities of the peaks also provide the crystallinity of specific planes. The XRD experiment is performed in a Rigaku SmartLab X-ray diffractometer, the theta-2 theta configuration is used for the scanning process.

2.2.4 Fourier transform infrared spectroscopy

The surface groups are characterized by using Fourier transform infrared spectroscopy (FTIR). Briefly, FTIR is a sensitive spectroscopy technique for obtaining IR spectrum by collecting an interferogram of a sample signal using an interferometer. Fourier transform (FT) is then performed on the interferogram to obtain the resultant spectrum. In this work, the Vortex 70, Bruker was used to measure the transmission spectra of the UCNCs (Figure 13). The conjugated functional groups, such as PEI, PEG and PAA are organic polymers, which consists of vast amount of organic functional groups. In fact, these groups are sensitive to the mid infrared (MIR) radiations, thus the absorptions and vibrations of these groups from 1000 to 4000 cm^{-3} are detected for comparison with standard wavenumbers. The samples are prepared by using freeze-drying and mixed with potassium bromide (KBr) powder for pallet preparation. KBr is transparent to MIR and they can act as a matrix to disperse the functionalized-UCNCs for transmission measurement. Moreover, KBr can reduce the amount of UCNCs for sample preparation.

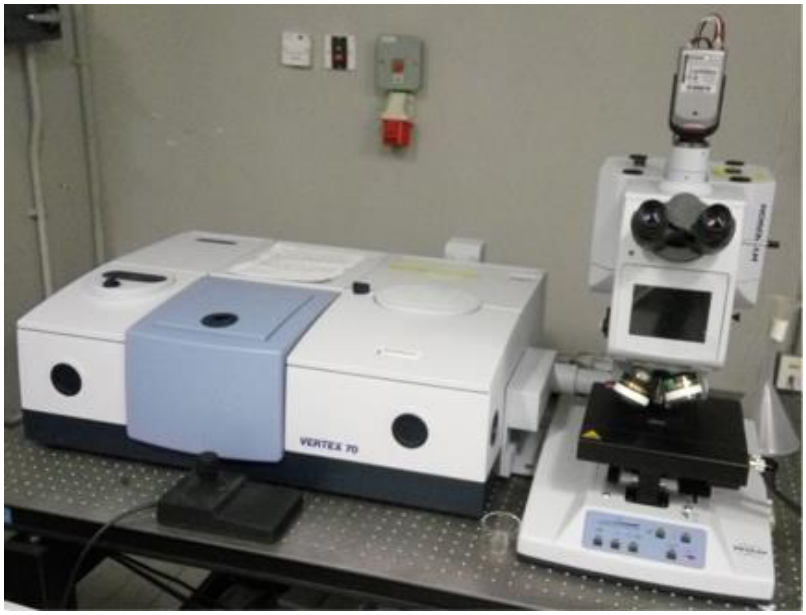

Figure 13 FTIR spectrometer for surface characterization (Vortex 70, Bruker).

2.2.5 Zeta potential measurement

Although FTIR can reveal the presence of organic groups, it cannot indicate the surface charge of the functionalized UCNCs. Zeta potential (ξ) can be used for the measurement of the surface charge properties, ξ is defined as the charge on the particle at the shear plane (Figure 14).[132] The parameter reflects the colloidal stability of the nanocrystals in a particular solvent; hence the measurements can aid the understanding of dispersion, aggregation and flocculation. The surface charges of the functionalized UCNCs are important for further conjugations and implication of successful conjugations. For instance, the conjugation of DNA oligos of onto the amine functionalized UCNCs resulted in a stark change of positive to negative charge surface.

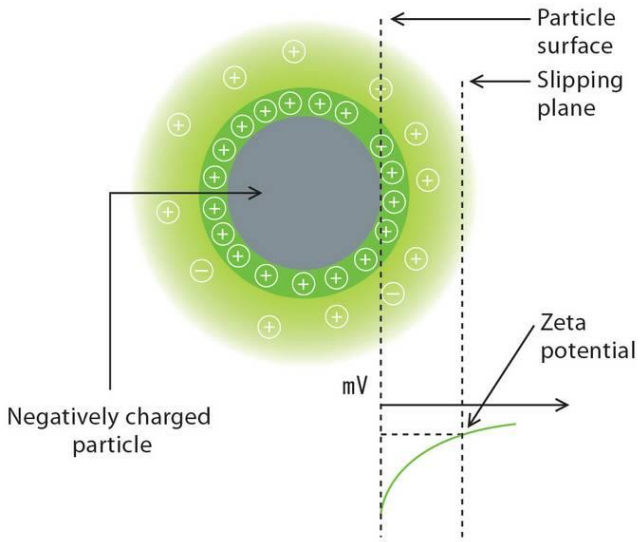

Figure 14 Schematic representation of ξ. (Horiba, SZ-100 Brochure)

2.2.6 UV-vis absorption

The absorption property of the quenchers in biodetection is critical for facilitating the LRET phenomena for luminescent biodetection. In addition to quenchers, the absorbance of the oligo with dye was also measured to quantify the amount of conjugated oligo on the surface of the nanoparticles. As a result, the UV-vis spectroscopic technique was chosen to evaluate the absorption properties. The UV-vis absorption spectroscopy is the measurement of the attenuation of light after it passes through the sample. The wavelength of the light source was selected by a monochromator and subsequently absorbed by the measuring sample; the absorbance at specific wavelength manifested the absorption spectra for analysis. The absorbance was used to calculate the concentration of the number of molecules or particles in the sample

by using Beer-Lambert's Law,

$$A=\varepsilon cl \qquad (4)$$

A is the absorbance, ε is the extinction coefficient, c is the concentration of molecules or particles in the sample and l is the optical path of the cuvette.

3. Detection of Ebola virus oligo by UCNCs/NAAO membrane

3.1 Introduction

Ebola virus, formerly known as Zaire ebolavirus, is a lethal pathogen that causes severe and even fatal hemorrhagic fever in humans and non-human primates. The previous outbreaks of Ebola virus diseases were limited to remote regions of central Africa, while the outbreak in February 2014 and spread quickly into several countries. A total of 21724 confirmed, probable and suspected cases, including 8641 deaths had been reported by January, 2015 with high fatality rate.[133,134] Traditional Ebola virus diagnosis methods include RT-PCR[135] and ELISA. Firstly, the target amplification based RT-PCR is limited by expensive equipment, laborious procedures, time-consuming and susceptible to contamination during amplification process. On the other hand, ELISA displays insufficient sensitivity for detection of lethal viruses. Therefore, considerable amount of attempts had been made to develop rapid test for virus detection, for example, biobarcode assay approaches, optofluidic biosensors based on plasmonic nanoholes and interferometric measurement techniques.[136–138] These techniques detected the presence of the virus by using the complementary oligo hybridization or antibody-antigen interaction. Despite the effort, the fabrication processes for these sensors are usually complicated and the sample preparation time is quite long.

Although downshifting luminescent nanosensors[139] are developed for sensitive,

rapid and low-cost detection, the UV excitation posed destruction to the backbone of the DNA oligos and severe background signals.[140] These provided uncertainties in the final detection signal and eventually contributed to false positive results. As a result, this paved the way for the emergence of NIR-triggered UCL for detection of virus oligos. NIR excitation does not pose destruction to the oligo backbone and background fluorescence, the sharp emission bandwidth and large anti-Stokes shift can also avoid cross talk and provide clear determination of detection signal.[38,141–143]

Previously, a homogeneous assay was developed for the detection of H7 Avian influenza subtype and the assay yielded a LOD of 7 pM. [47] Unfortunately, the LOD is not sufficient for detecting lethal viruses. This chapter presented the fabrication of the heterogeneous assay based on UC nanoprobe/nanoporous alumina (NAAO) membrane. The high porosity of NAAO membrane was originally used for filtering chemicals and other impurities. However, researchers had been explored their ability as biosensors to detect different analytes, such as bacteria, toxins and pollutants.[144–147] There was no report that utilized the NAAO membrane for fabricating composites for luminescent detections. The UC nanoprobes were anchored in the hollow channels of the NAAO membrane via covalent bond. On the other hand, the AuNPs captured the virus oligo and quenched the UCL emission as a reporting signal for detection. The homogeneous assay was also prepared to compared with the heterogeneous assay, the LOD was improved by around 20 folds compared to the homogeneous assay; such enhancement could be attributed to the increased oligo hybridization throughout the cross section of the membrane. Moreover, clinical Ebola virus oligos were tested to validate the new

design for future biomedical applications.

3.2 Experimental procedures

3.2.1 Hydrothermal synthesis of PEI-$BaGdF_5$:Yb/Er UCNCs

PEI-modified $BaGdF_5$:Yb/Er UCNCs were synthesized according to previously reported one-step hydrothermal synthesis.[14,46–48,148,149] Typically, 1.0 g of PEI was added to 20 mL of EG with 1 mmol of lanthanide dopants 0.5 M $Gd(NO_3)_3$, $Yb(NO_3)_3$, and 0.1 M $Er(NO_3)_3$ with a molar ratio of 78:20:2 under vigorous mixing. $BaCl_2$ (1 mmol) was added to the above solution under stirring. The mixture was agitated for 30 min to form a transparent homogeneous solution. After that, 5.5 mmol of NH_4F in 10 mL of EG was added to the above mixture. The mixture was agitated for 1 h and subsequently transferred to a 50 mL stainless steel Teflon-lined autoclave and hydrothermal at 190 °C for 24 h. After reaction, the as-prepared UCNCs were purified by using ethanol and DI water. Finally, the amine functionalized UCNCs were dispersed in water for further conjugations.

3.2.2 Synthesis of citrate-stabilized AuNPs

AuNPs were prepared following the procedures described in previous study.[150] Briefly, a mixture of Gold(III) chloride trihydrate solution (3 μL, 14.3 wt %) and

Deionized (DI) water (10 mL) was boiled in beakers that were washed thoroughly in aqua regia (mixture of hydrochloric acid and nitric acid with the ratio of 3:1) and rinsed in DI water. Sodium citrate solution (1 mL, 1 wt %) was quickly injected to the boiling solution under vigorous stirring. The solution color abruptly changed from pale yellow to wine red in few min. The solution was allowed to boil continuously for 15 min and left to cool down to room temperature under stirring.

3.2.3 Conjugation of Ebola virus oligo with AuNPs

The studying model was built by using the Au-thiol conjugation. Thiol modified Ebola virus oligonucleotide (short segment: 5'-thiol GGACCGCCAAGGTAAAAAAT GAGGT-3', 25-base, M233114.1), FAM modified oligo (5'-thiol-GGACCGCCAAGGTAAAAAATGAGGT-FAM-3') another non-target oligo (S1:5'-thiol-CCTGGCGGTTCCATTTTTTACTCCA-3') and 3-base mismatch oligo (S2: 5'-thiol-GGACCGGCAAGGAAAAAATTGAGGT-3') were purchased from Integrated DNA Technologies (IDT) Inc. (Coralville, IA). Thiolated oligo were cleaved by dithiothreitol (DTT) (0.1 M, pH 8.2) and purified by gel columns (illustra MicroSpin G-25 Columns, GE Healthcare, UK). Thiol modified Ebola gene oligo were mixed with AuNPs and incubated for 24 h at room temperature. Sodium solution (0.1 M sodium chloride, 5 mM monosodium phosphate) was added to age for 16 h. The excess oligos were removed by centrifugation for 30 min at 13200 rpm. The remaining red oily precipitate was collected and washed by phosphate buffer saline (PBS) solution for 3 times. The complementary oligo was added to the AuNPs-Ebola virus oligo conjugation

system and incubated for 30 min to ensure full hybridization. The unreacted single-stranded oligo was removed by centrifugation. The double-stranded oligo and AuNPs conjugation was incubated at different temperatures for quantification using UV-vis technique.

3.2.4 Surface modification of NAAO membrane

NAAO membranes with a pore diameter of 100 nm were cleaned and hydroxyl (-OH) groups were generated on the surfaces by boiling in hydrogen peroxide for 30 min and rinsing in DI water with gentle shaking for 15 min. Dried membranes were immersed in a solution of 3-aminopropyltriethoxysilane (APTES) and acetone (2 % APTES) for 1 h and followed by rinsing with acetone.[151] The silane linkage was cured under 110 ^{o}C for 1 h. Amine functionalized UCNCs were dispersed in PBS (pH 7.4, 10 mM) with the concentration of 10 mg/mL, followed by addition of 2 µL glutaraldehyde to the mixture. The mixture was shaken for 1 h at room temperature to ensure thorough reaction. It was centrifuged and washed by PBS for 3 times to remove excess glutaraldehyde and resuspended in PBS. The functionalized UCNCs were added to APTES modified NAAO membrane and reacted overnight. UCNCs were conjugated on NAAO membrane by glutaraldehyde linkage between amino groups. Acetaldehyde solution (2 %) was used to rinse the NAAO membrane immobilized with glutaraldehyde modified UCNCs to react with the remaining amino groups on membrane surface. Amino modified oligonucleotide probes (5'-amino-ACCTCATTTTTTACCTTGGCGGTCC-3', 5 µM) were covalently conjugated to

UCNCs on NAAO membrane using glutaraldehyde as the linkage.

3.2.5 Homogeneous assay preparation

PEI modified $BaGdF_5$:Yb/Er UCNCs was covalently conjugated with amino modified oligonucleotide probe (5'-amino- ACCTCATTTTTTACCTTGGCGGTCC -3') and (5'-amino-ACCTCATTTTTTACCTTGGCGGTCC-FAM-3') by covalent bond with glutaraldehyde as the cross linking agent. 2 mg UCNCs were dispersed in 200 μL of PBS (pH 7.4, 10 mM). UCNCs were added to glutaraldehyde (5 %, 1 mL) and left reaction with gentle shaking for 1 h at 25 ^{o}C. The glutaraldehyde-activated UCNCs were washed and resuspended in 200 μL PBS. Amino modified oligonucleotides (100 μM) were incubated with glutaraldehyde-activated UCNCs. FAM modified oligos (5 μM, 100 μL) were conjugated on UCNCs (10 mg/mL, 50 uL) and centrifuged. The supernatant was collected and diluted to 100 μL for fluorescence intensity measurement. Fluorescence intensity was measured by microplate reader (Infinite F200, Tecan, Switzerland). Various concentrations of Ebola virus oligonucleotides conjugated with AuNPs were mixed with $BaGdF_5$:Yb/Er UCNCs-oligo (0.2 mg/mL) and incubated for 2 h at 25 ^{o}C for hybridization of Ebola virus oligos with probes. The mixture was subjected to for LRET measurement using FLS920 Edinburgh analytical instrument.

3.2.6 Heterogeneous assay preparation

The prepared AuNPs-Ebola target oligo conjugation was incubated with modified NAAO membranes for 2 h at room temperature to ensure complete hybridization between Ebola target oligos and probes. The hybridization process led to close proximity of AuNPs and UCNCs in the membranes. The NAAO membrane immobilized with UCNCs-probe oligo was fixed on the measuring stage of FLS920 Edinburgh analytical instrument for PL measurement with the center point and surrounding four points detected. The same detecting procedure was applied for PL measurement after various concentrations of target oligos conjugated with AuNPs hybridization with probe oligo on NAAO membrane. The photoluminescence intensity of each concentration was averaged by the data obtained from five points. The visible emissions from UCNCs were absorbed by AuNPs, and then the quenched UC LRET spectra were obtained under 980 nm laser excitation.

3.2.7 Gene extraction from inactivated Ebola virus particles

The ribonucleic acid (RNA) was extracted from the inactive Ebola virus particles supplied by the Beijing Hospital (Beijing, China). The inactive samples consisted of purified RNA target fragments (2400 bp, 3'-untranslated region (UTR) and a large part of the NP region). Nucleotide sequences of the epidemic strain of Zaire Ebola virus from West Africa were obtained from GenBank KJ660346, KJ660347 and KJ 660348. The detailed preparation procedures for Ebola virus particles were based on

the protocols for external quality assessment (EQA) of Ebola virus molecular detection in China established by National Center for Clinical Laboratories (NCCL) of China. Generally, Zaire (Mayinga) Ebola virus from infected Vero E6 pellets was suspended in 50 mM sodium borate and gamma irradiated on dry ice and sonicated to get inactivated and highly disrupted viral particles. To purify the inactivated viral particles, the cell supernatants were pelleted over a 20 % sucrose cushion and then further purified on a 10-60 % sucrose gradient. The gradient fraction containing the inactivated viral particles was then collected. Inactivated virus particles were mixed with human serum from human male AB plasma (Sterile-filtered, Sigma Chemical Co.) to extract the viral oligo. Total oligonucleotide fragments were extracted and fragmented from the above sample (200 μL) using a PureLink Viral RNA kit (Life Technologies) with RNA fragmentation reagents according to procedures. The extracted oligonucleotides were eluted in 30 μL sterile, RNase-free water and detected by the biosensor without thiol modification. The target oligonucleotides contain a fragment with the sequence: 5'-GGACCGCCAAGGTAAAAAATGAGGT-3', which led to the hybridization with the probe immobilized on UCNCs.

3.2.8 Viral RNA-AuNP conjugation

AuNPs were functionalized with 3-Mercaptopropionic acid (3MPA) by covalent bonding between AuNP and thiol group of the linker. RNA extracted from inactivated Ebola virus particles were conjugated on functionalized AuNPs by EDC activation. Diluted 3MPA solution (6 μM, 5 μL) was slowly added into AuNPs solution (6 nM, 100 μl) and incubated for 10 h at 4 ℃. The excess linker molecules were removed by centrifugation. The remaining functionalized AuNPs were collected and redispersed in sterilized PBS. The extracted RNA (10 μL) was added to conjugate with functionalized AuNPs for hybridization and detection.

3.3 Characterizations

3.3.1 Detection scheme based on the nanoprobe/membrane assay

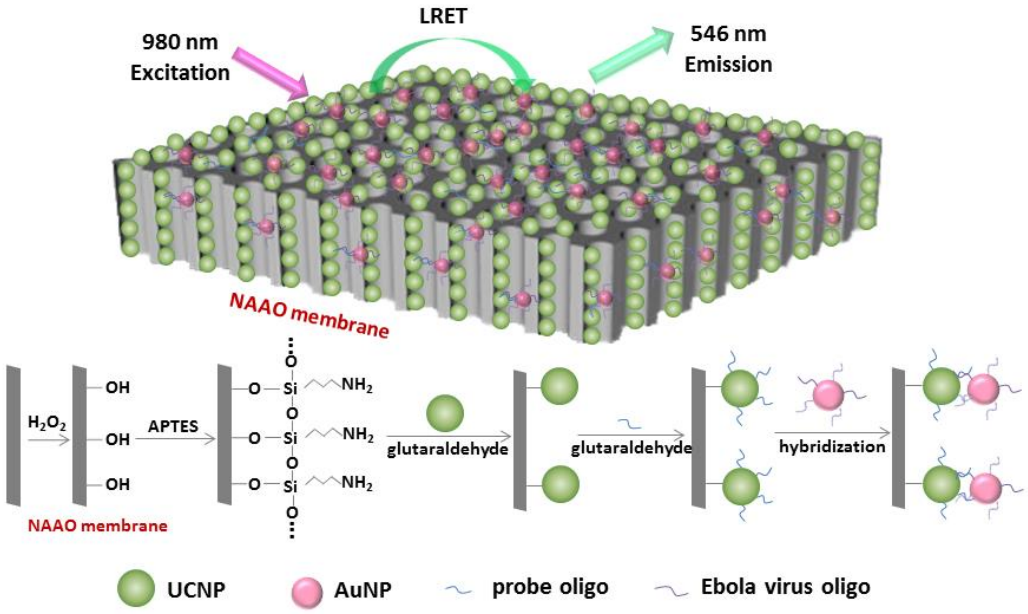

Figure 15 Detection scheme for the UC nanoprobe/NAAO membrane heterogeneous assay. The chemical modification steps were shown below.

Figure 15 presents the detection scheme of the Ebola virus oligo by using UC nanoprobe/NAAO membrane heterogeneous assay. The NAAO membrane was firstly boiled with hydrogen peroxide to activate the –OH group, then APTES was added to create amine surface throughout the cross section of NAAO membrane for internalization of amine-functionalized UCNCs. The Ebola virus oligo specific probe was immobilized of the UCNCs as the nanoprobe, the oligo hybridization between

complementary pairs can bring AuNPs to the proximity of UCNCs on the NAAO membrane. As a result, this manifested the condition for LRET. The decrease in UCL intensity acted as the reporting signal to validate the concentration of the virus oligo. Note that the NIR-triggered nature of UCNCs causes low photodamage to the Ebola virus oligo. The high surface area to volume ratio of NAAO allows large amount of UCNCs to conjugate into the membrane.

3.3.2 Phase, morphology and elemental analysis of the PEI-UCNCs

The amine-functionalized UCNCs were prepared by the one-step hydrothermal method with branched PEI as capping agent. The branched configuration can not only passivation the growth but also endow repulsion between UCNCs, therefore the PEI-modified UCNCs can form a stable colloidal in water. The mean size of the UCNCs was obtained by counting the size of 400 NPs, the distribution of the size is shown in Figure 16(a). The distribution presented a Gaussian-like shape with a mean of around 14 nm. Moreover, the selected electron diffraction (SAED) presented in Figure 16(b) shows clear diffraction rings; this indicated the polycrystalline nature of the UCNCs with simple cubic phase structure. Also, the high resolution transmission electron microscopy (HRTEM) image (Figure 16(c)) indicates the lattice spacing is estimated as 2.96 Å, and it is consistent with the (200) of simple cubic structure of $BaGdF_5$ host.

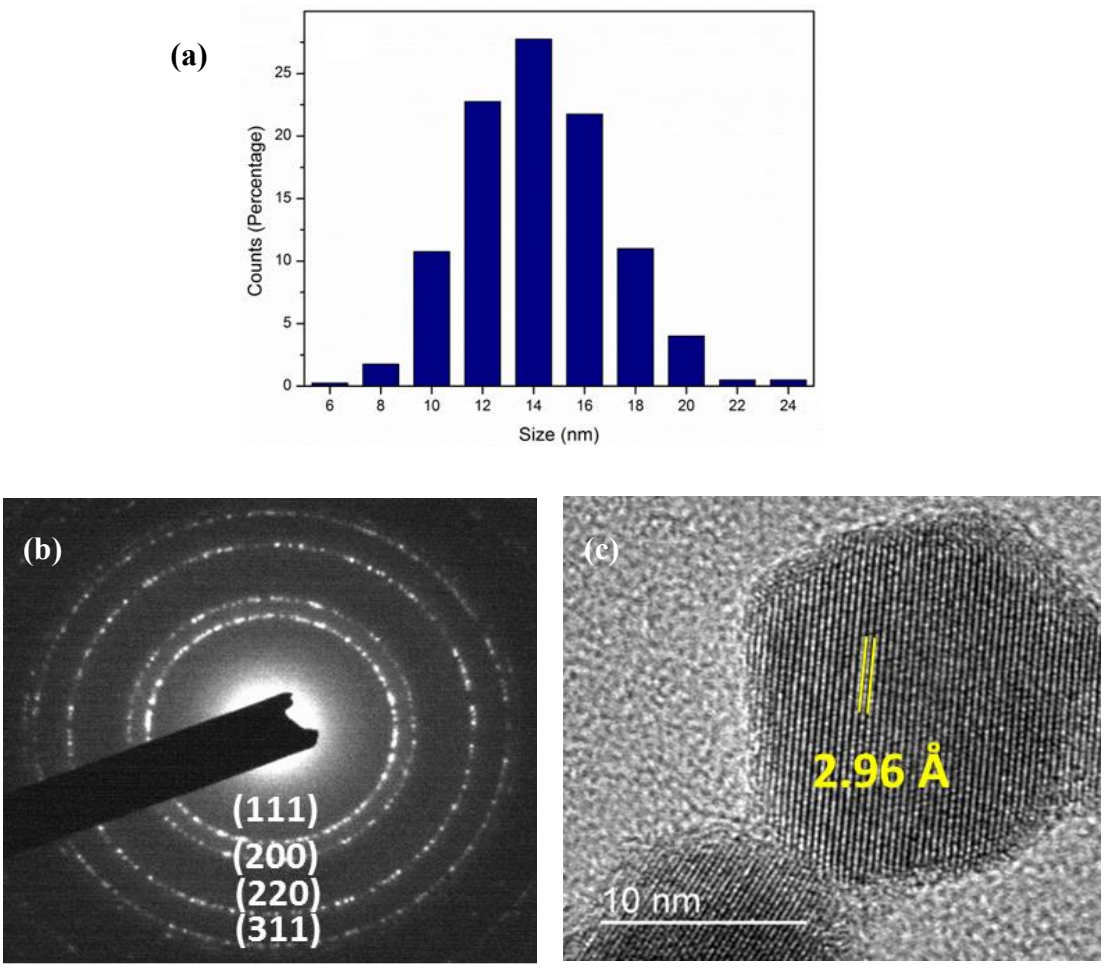

Figure 16(a) Size distribution (b) SAED pattern and (c) HRTEM of the of the as-synthesized PEI-modified $BaGdF_5$:Yb/Er UCNCs.

In addition to the morphology and phase of the UCNCs, the elemental analysis is able to provide solid evidence for the doping of ions. The energy dispersive X-ray (EDX) spectrum is shown in Figure 17(a). The peaks of all the elements in the UCNCs were indexed, for example Ba, Gd, F and various Ln^{3+} ions. The element distribution in space was confirmed by using the scanning transmission electron microscopy (STEM) technique (Figure 17(b)). The yellow frame indicates the selected area for elemental

mapping analysis. The panels labelled different elements, such as Ba, Gd, F, Yb and Er. The mapping was carried out in five channels with different colours. The amount of dots represented the atomic amount of the ions in the area. Among them, the fluorine channel resulted in the strongest signal and this was consistent with the synthesis condition.

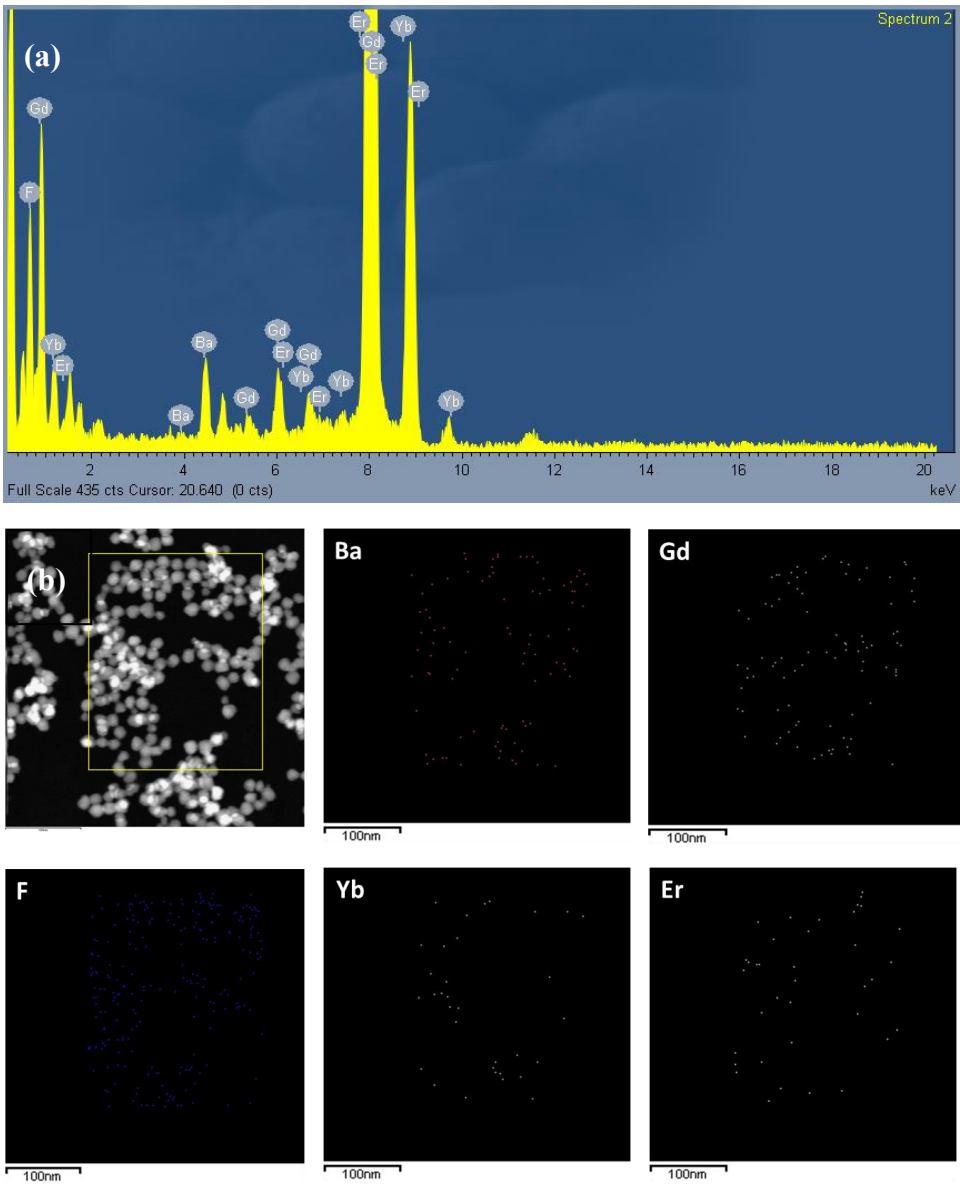

Figure 17(a) EDX spectrum and (b) STEM image of PEI-modified $BaGdF_5$:Yb/Er UCNCs, the panels were labelled with different colours to represent different elements.

3.3.3 Optical properties of the PEI-UCNCs and AuNPs

After purification and separation, the amine-functionalized UCNCs were dispersed in water to form stable colloidal for PL measurement. The UCL spectrum was measured by using a colloidal of 1 mg ml^{-1} under 980 nm laser excitation. Figure 18(a) presents the emission spectrum of the UCNCs, the three major peaks at around 520, 540 and 654 nm were due to the Er^{3+} ions. Moreover, the inset shows the observed green emission. The power dependence for the respective peaks was also measured by tuning the excitation power. Figure 18(b) indicates that the slope of the emission peaks can be fitted by the power law of UC with values close to 2. This suggested the UC process was a two photon process. In fact, the UC emission peaks can be deduced by using the simplified energy level diagram in Figure 18(c). The Yb^{3+} ion absorbed the incoming 980 nm excitation and resulted in the emission of phonons. The phonons resonated with the energy level of Er^{3+} ions by energy transfer and populated the Er^{3+} ions to higher energy states.

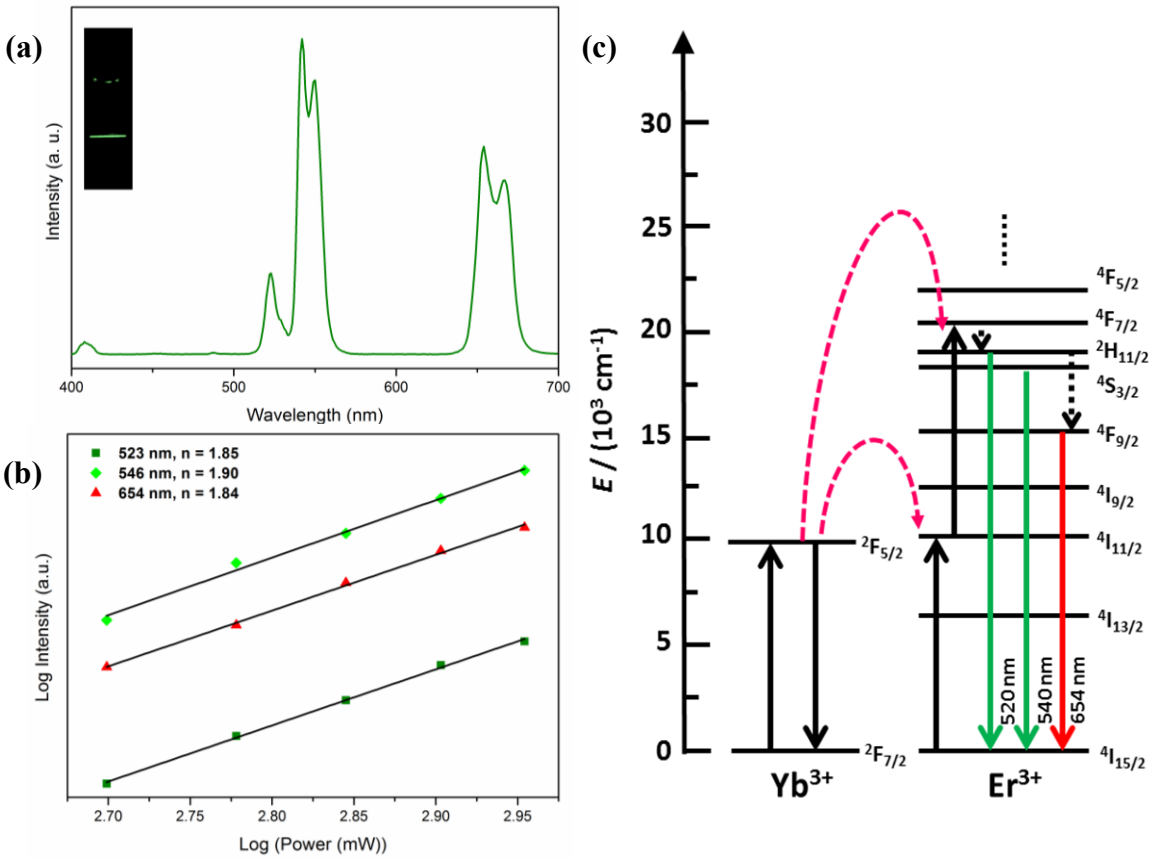

Figure 18(a) UCL emission spectra (b) Power dependence and (c) Simplified energy level diagram of PEI-modified $BaGdF_5$:Yb/Er UCNCs. Inset of (a) shows the green UCL emission under 980 nm laser excitation.

In addition to the UCL property, the plasmonic absorption of AuNPs play important role in the LRET detection system as the quencher. The absorption property of AuNPs is size dependent, the increase in the crystalline size of the AuNPs result in the redshift of peak absorption wavelength. The absorption spectra of the AuNPs are shown in Figure 19. The as-synthesized AuNPs displayed peak absorption at around 540 nm, this enable efficient overlapping of the absorption spectrum and emission spectrum for LRET detection. After the capturing of virus oligo, the absorption peak of the

AuNPs shifted slightly. This was also served as an indicator for successful conjugation.

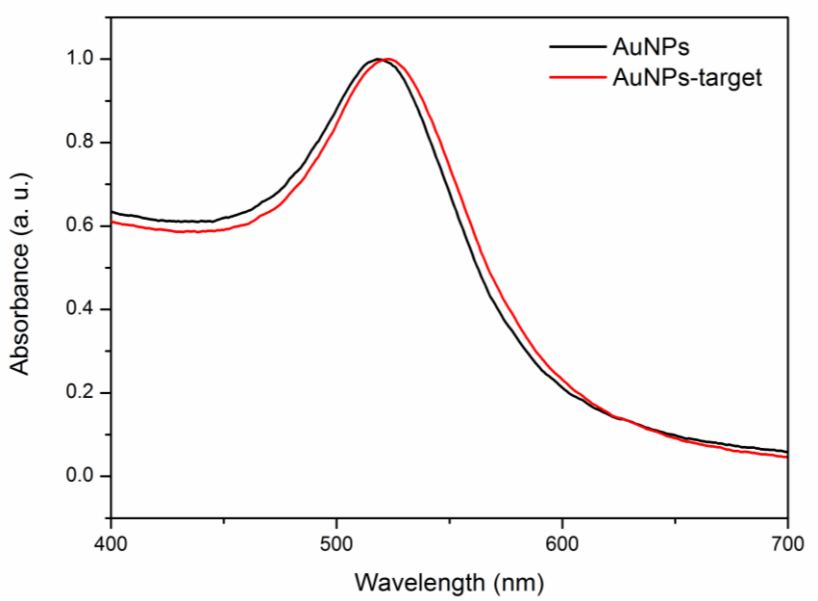

Figure 19 Absorption spectra of AuNPs and Ebola virus oligo captured AuNPs.

3.3.4 Formation of the homogeneous assay

The amine surface of the UCNCs was replaced with glutaraldehyde to bind with the probe oligo to form the nanoprobe. The oligo coating was revealed by HRTEM, Figure 20(a) shows a single oligo coated UCNP, the coating was uniform and the contrast was not high because of the non-crystalline nature of oligos. After oligo hybridization, it can be seen that the single UCNP was surrounded by several AuNPs. The formation of such satellite structure was due to the hybridized duplex (Figure 20(b)).

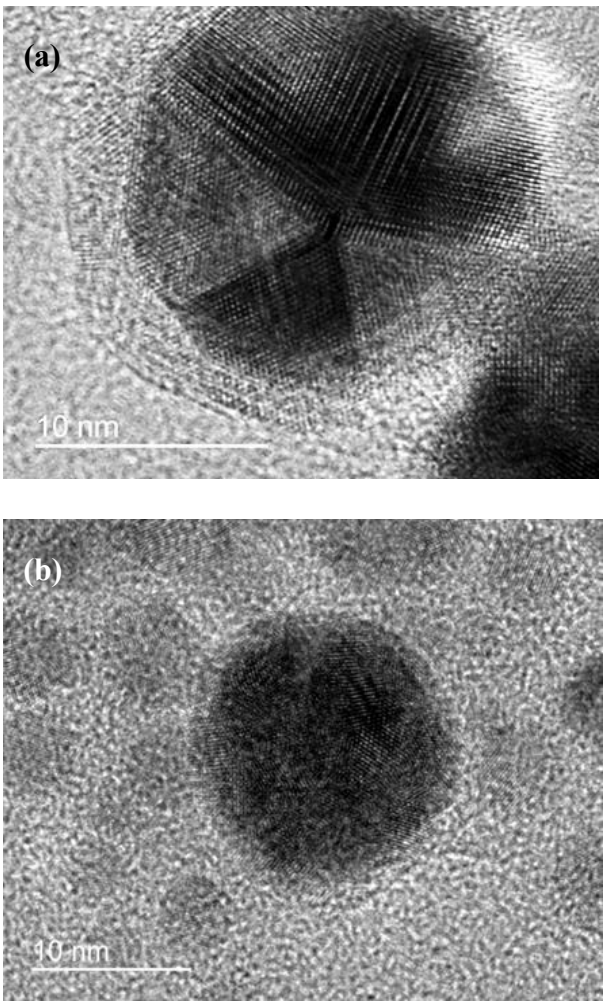

Figure 20(a) Formation of oligo layer after glutaraldehyde modification and (b) Formation of satellite structure by hybridizing UCNCs and AuNPs as oligo duplex structure.

In addition to TEM, XRD was also used to investigate the phase of the hybridized structure. Prior to experiment, it was predicted that the hybridized sample should demonstrate two types of crystalline structures. Figure 21(a) and (b) show the XRD scan of the $BaGdF_5$:Yb/Er UCNCs before and after oligo modification, respectively. The patterns suggested that the coating of the oligo layer did not induce

any change in the crystalline structure, this agreed with the observation with Figure 21(a). Moreover, two types of XRD patterns were observed in Figure 21(c), the additional (111) plane was due to the presence of the AuNPs after hybridization.

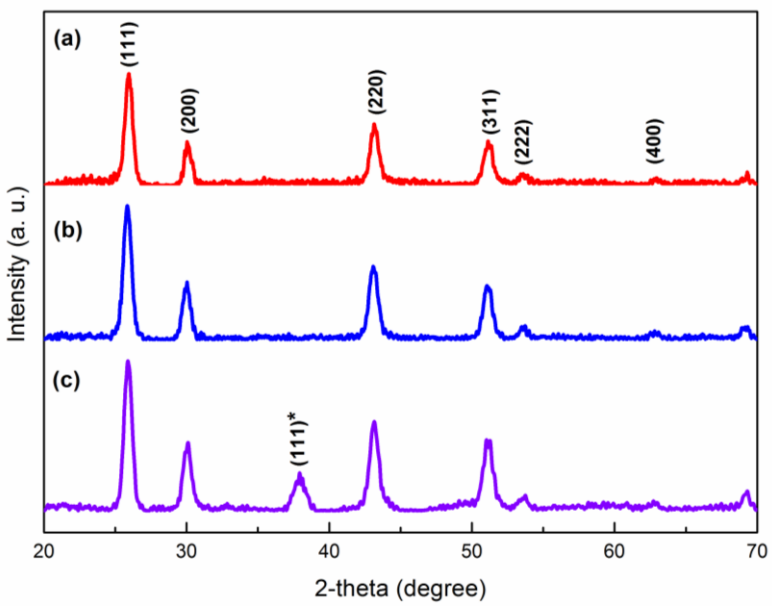

Figure 21 XRD patterns of (a) PEI-modified and (b) Oligo-coated $BaGdF_5$:Yb/Er UCNCs; (c) Hybridized homogeneous assay with $BaGdF_5$:Yb/Er UCNCs and AuNPs.

Apart from XRD, the organic bonds present in the surface ligands and groups are sensitive to mid-infrared radiation. Those bonds vibrate and stretch as a result of absorbing the MIR photons. Figure 22(a) shows the transmission spectrum of the PEI-modified UCNCs. The large absorption band centered at 3440 cm^{-1}, small absorption band at 1645, 1523 and 1440 cm^{-1} were attributed to the N-H and C-N bonds. Moreover, the small absorption bands at 2924 and 2859 cm^{-1} were due to the vibration of $–CH_2$ bonds. After oligo modification, a new peak at 1053 cm^{-1} appeared in Figure

22 (b). This peak was a directly evidence of the oligo coating, because this peak aroused from the P=O bond in the phosphate backbone of DNA oligo strands. The backbone is bonded with the four bases: cytosine (C), guanine (G), adenine (A), or thymine (T). These functional groups also consist of N-H and C-N bonds, therefore the remaining absorption peaks are similar to that of PEI-modified UCNCs.

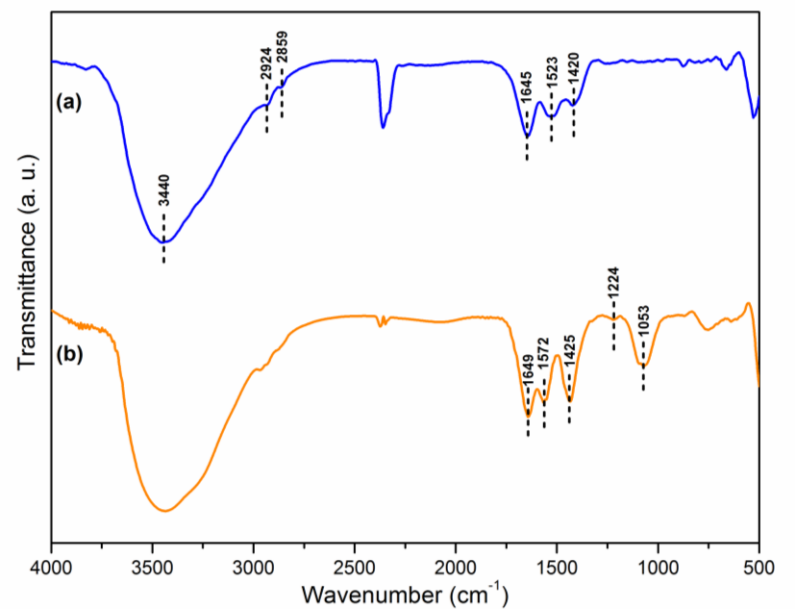

Figure 22 FTIR transmission spectrum of (a) PEI-modified and (b) Oligo coated-$BaGdF_5$:Yb/Er UCNCs.

In FTIR, some of the wavenumbers of absorption bands might overlap with particular bonds, for example the absorption band of O-H and N-H. Therefore, ξ is needed to assist the justifications of the surface modifications. The ξ of the PEI-modified UCNCs is presented in Figure 23(a). Initially, the as-prepared UCNCs displayed a highly positively values owing to the vast amount of NH_2 groups on the branched PEI molecules. After oligo modification, the ξ value shifted from positive to

negative, such shift indicated the successful oligo modification because of the negatively charged phosphate backbone. On the other hand, the AuNPs indicates negative ξ value because of the citrate stabilization, the capturing of the virus oligo shifted the ξ value to slightly negative (Figure 23(b)). The difference between the negative ξ value in the UCNCs and AuNPs was due to the amount of oligos on the surfaces. Importantly, the amount of probe oligo was larger than that of the captured target Ebola virus oligos to facilitate efficient oligo hybridization for detection.

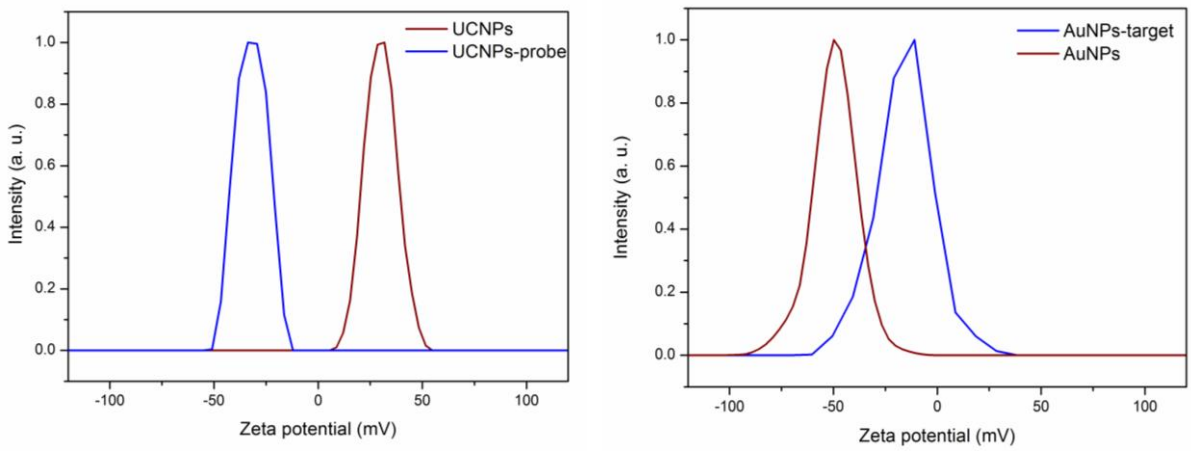

Figure 23 ξ value of (a) PEI and oligo modified $BaGdF_5$:Yb/Er UCNCs and (b) Citrate-stabilized and Ebola virus target captured AuNPs.

3.3.5 Formation of the heterogeneous assay

In homogeneous assay, the liquid state samples can be easily fitted into different systems for characterizations while the samples in the heterogeneous assay are solid phase samples. Therefore, different characterization techniques are used for justifying the NAAO membrane-based heterogeneous assay.

The NAAO membrane consists of hollow structure throughout the surface, therefore the cross-section was investigated by using SEM. Figure 24(a) shows the SEM image of the cross-section of a bare NAAO membrane. The nanochannels were well-aligned with average width of around 100 nm. The nanochannels and the PEI-modified UCNCs were linked by using glutaraldehyde. The internalization of the UCNCs into the NAAO membrane was driven by capillary force. Figure 24(b) presents the morphological change after the internalization of the UCNCs. A substantial amount of nanoparticles occupied the nanochannels with high density. EDX scan was performed on the whole area of Figure 24(b) to prove the anchoring of UCNCs in the nanochannels. Figure 24(c) shows the EDX spectrum of the selected area, the essential elements in the UCNCs and Al were presented in the spectrum. However, the doping amount of Yb^{3+} and Er^{3+} ions were relatively low, therefore they were not displayed in the spectrum. After that, the oligo probe was also deposited onto the surface of the UCNCs as nanoprobe for hybridizing with the Ebola virus oligo. The injection of the virus oligo bearing AuNPs resulted in a significantly higher occupation density (Figure 24(d)) than that in Figure 24(b). However, it should be noted that the light elements in

the oligos, such as nitrogen and oxygen, cannot be detected by using EDX. Therefore, sensitive and powerful spectroscopic method is necessary to reveal the presence of all the elements in the hybridized NAAO membrane.

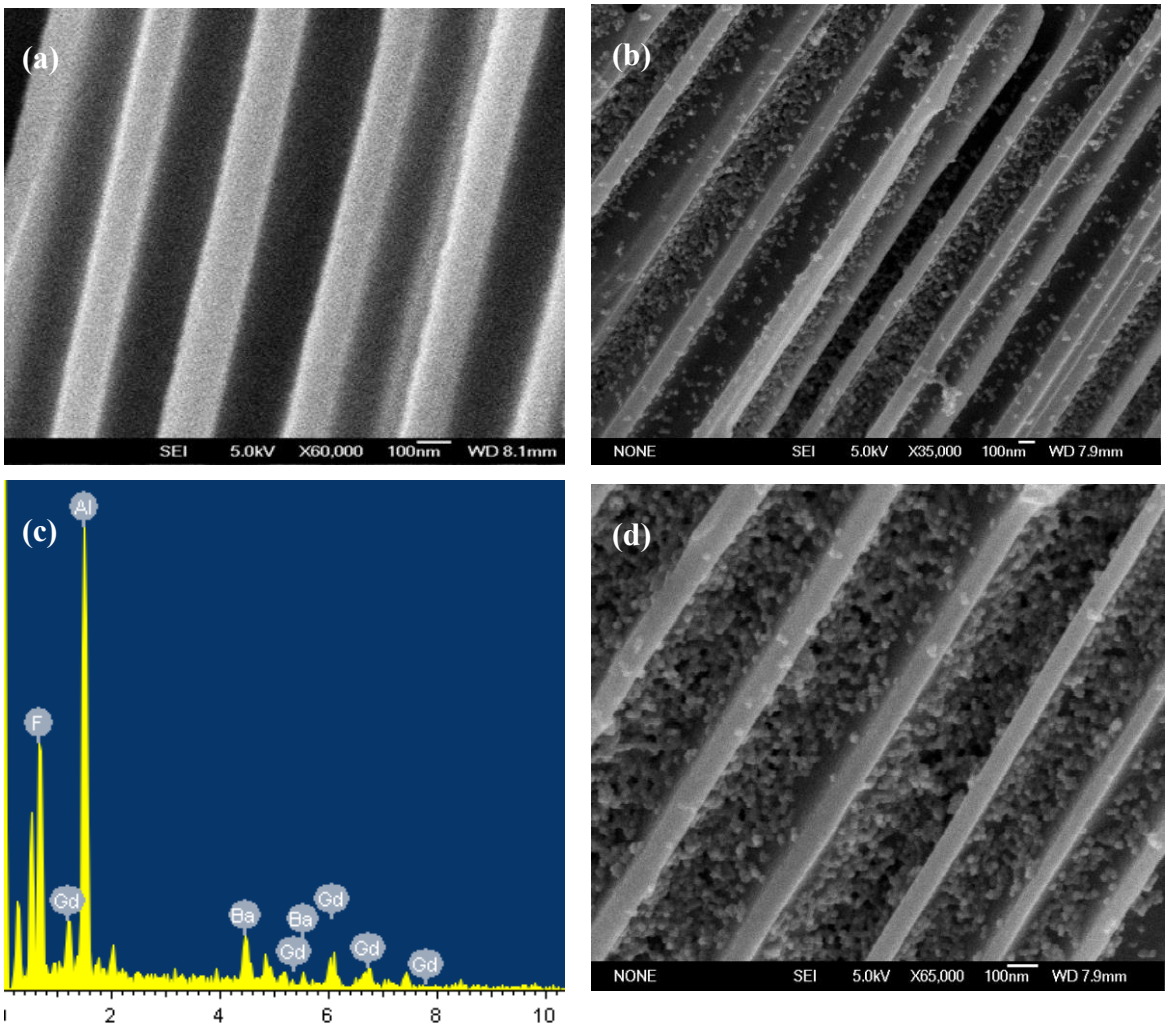

Figure 24 SEM images of (a) cross-section of bare NAAO membrane and (b) NAAO membrane after modification with UCNCs, (c) EDX spectrum of NAAO membrane after UCNCs modification and (d) SEM image of the hybridized NAAO membrane, the UCNCs and AuNPs were hybridization in the nanochannels.

X-ray photoelectron spectroscopy (XPS) is a surface sensitive technique that utilizes highly collimated X-ray photons for chemical analysis. The penetration depth is around 1 mm and hence the X-ray can penetrate the NAAO membrane (60 μm).

Moreover, the electronic states of the elements can be identified at specific binding energy ranges. The XPS wide scan from 0-800 eV was performed to observe the elements in the hybridized NAAO membrane (Figure 25). The electronic states of some elements, such as C (1s), O (1s), F (1s) and Ba (3d) were easily observed in the scan.

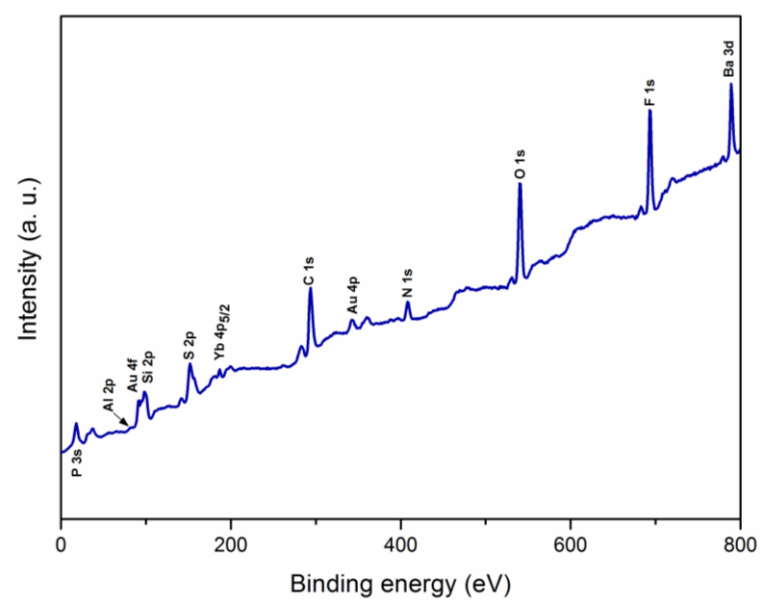

Figure 25 XPS wide scan of the hybridized NAAO membrane with UCNCs and AuNPs in the range 0-800 eV.

The electronic states of the elements were clearly labelled in the high resolution (HR) XPS scan (Figure 26), for example the Yb 4d and P 2s states. Nevertheless, the XPS results provided evidence for the internalization of the components that manifested the detection system.

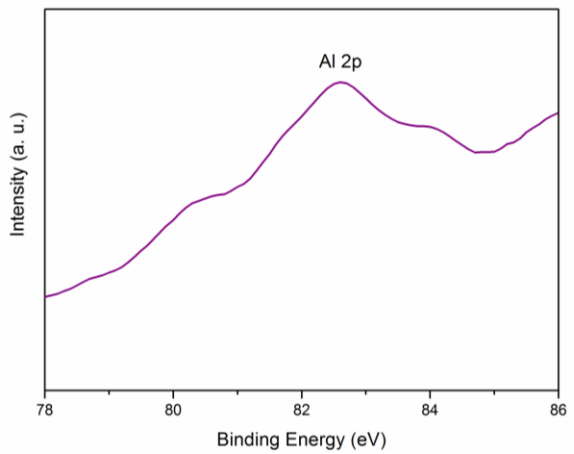
Al 2p
Intensity (a. u.)
78
80
82
84
86
Binding Energy (eV)

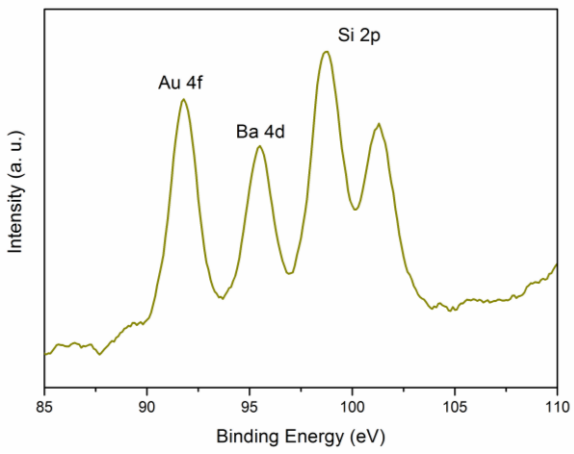
Si 2p
Au 4f
Ba 4d
Intensity (a. u.)
85
90
95
100
105
110
Binding Energy (eV)

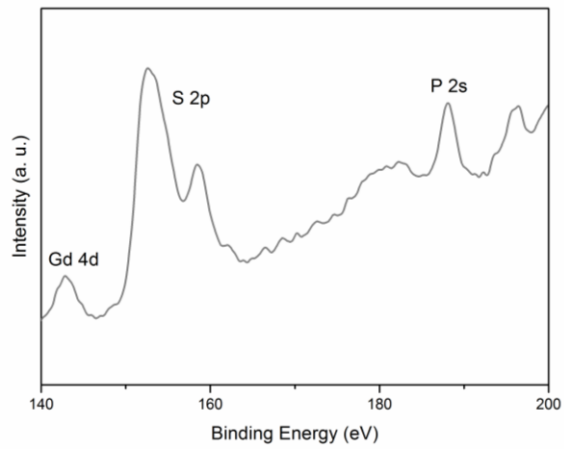
S 2p
P 2s
Gd 4d
Intensity (a. u.)
140
160
180
200
Binding Energy (eV)

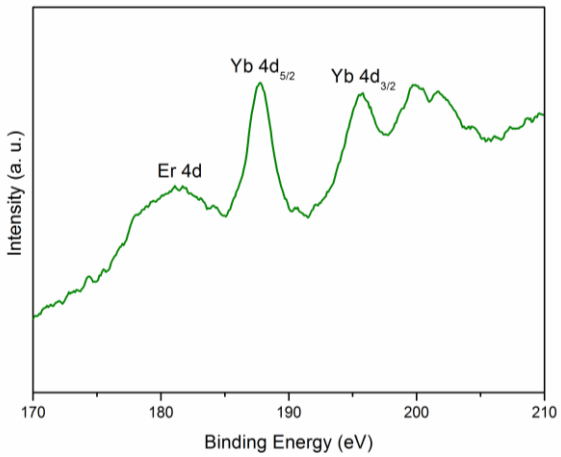
Yb 4d5/2
Yb 4d3/2
Er 4d
Intensity (a. u.)
170
180
190
200
210
Binding Energy (eV)

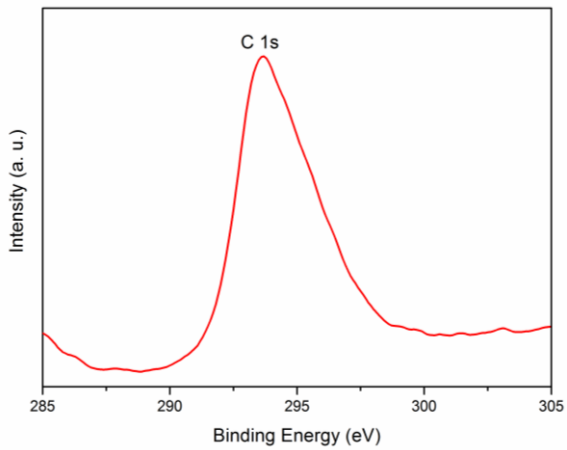
C 1s
Intensity (a. u.)
285
290
295
300
305
Binding Energy (eV)

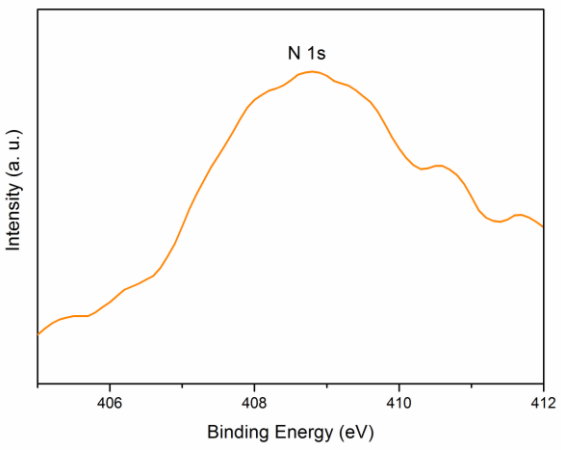
N 1s
Intensity (a. u.)
406
408
410
412
Binding Energy (eV)

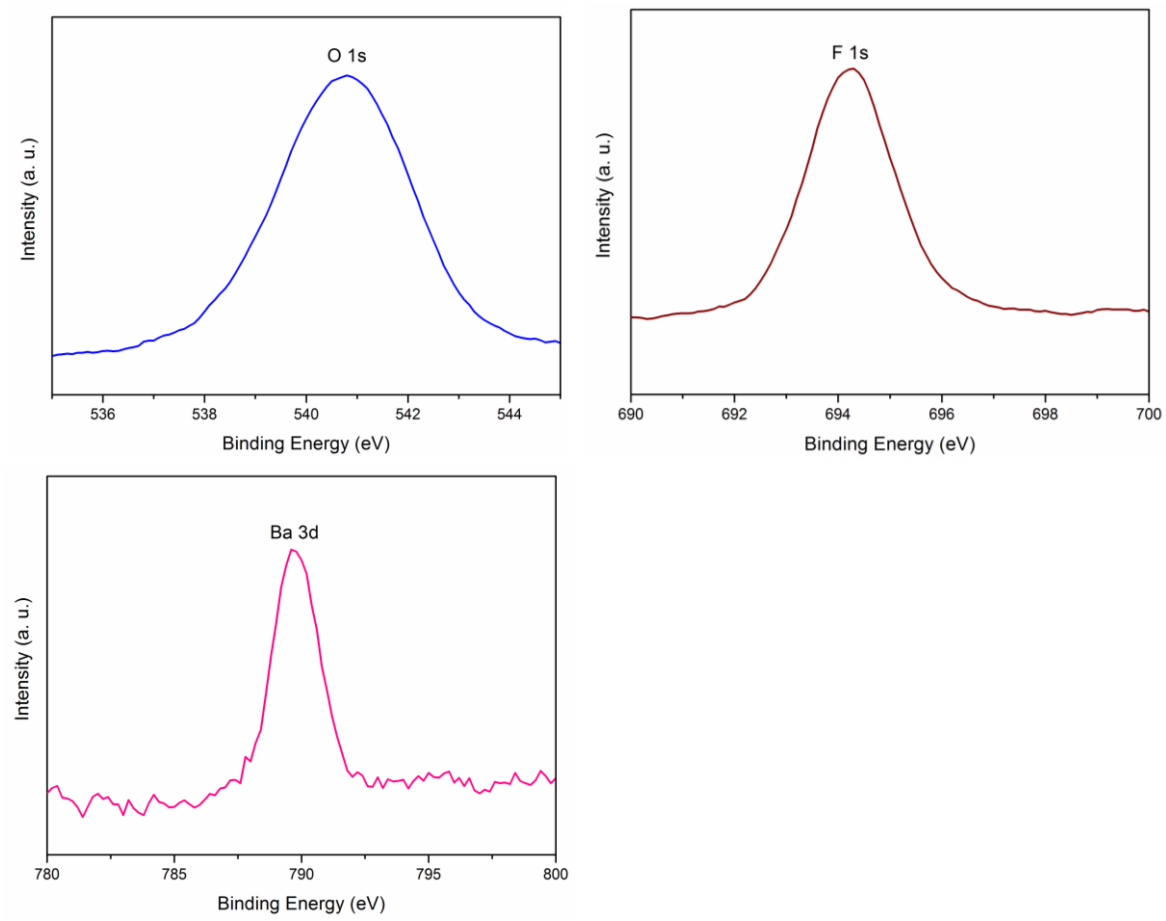

Figure 26 XPS-HR scans of different elements in the hybridized NAAO membrane. The electronic states at 0-800 eV were labelled in each graph.

3.4 Detection of Ebola virus oligo

After stringent characterizations, the simulated Ebola virus oligo was detected by using the homogeneous and heterogeneous assay. The homogeneous assay was performed to compare with the performance of the novel heterogeneous assay. The NAAO membrane provided new insight to UCL-based heterogeneous assay by exploring the impact of porous nanomaterials on the LOD of luminescent assays.

3.4.1 Homogeneous assay with UCNCs and AuNPs

The homogeneous assay was manifested by hybridizing the UCNCs-probe with the simulated virus oligo in PBS. Firstly, the number of virus oligo captured by the AuNPs was quantified by using UV-vis spectroscopy. The optical density at 260 nm was used as a standard for calculating the concentration, because that wavelength is an intrinsic absorption characteristic of DNA oligo strands. It was estimated that each AuNP consisted of 10 virus oligo molecules. Hereafter, the detected concentrations of the virus oligo were calculated by using this number. Figure 27(a) shows the UCL emission spectra of the UCNP-probes under different concentrations of virus oligos under 980 nm laser excitation. The control spectrum for comparison was 0.2 mg/ml UCNP-probe in PBS. The UCL intensities decreased with increasing concentrations of virus oligos, this can be explained by the enhanced LRET effect at increasing virus oligo concentrations for oligo hybridization. Since the emission maxima was observed

at around 540 nm, the emission intensities at that wavelength were recorded and extracted for further analysis on the quenching efficiencies and linearity of the sensor.

The quenching efficiencies were found by measuring the percentage change in luminescent intensities with respect to the control intensity. The quenching efficiencies increased abruptly from pM concentrations and then leveled off at around 5 nM of virus oligo. The highest quenching efficiency was around 80 % (Figure 27(b)). The qualities for evaluating sensors are the linear working range, LOD and specificity. The linear working range was found at the pM range (Figure 27(c)) and it was fitted as $y = 0.075 \ln(x) + 0.449$. In addition, the LOD was found by the lowest detectable concentration plus three times the standard deviation and it was estimated at about 7 pM. The specificity of a biosensor is equally important as its LOD because non-specific binding to other biological species will possibly result in false-positive signals. Figure 27(d) presents the specificity test using base mismatch and completely mismatch target. The discrimination between the two types of disturbance was at least 50 %.

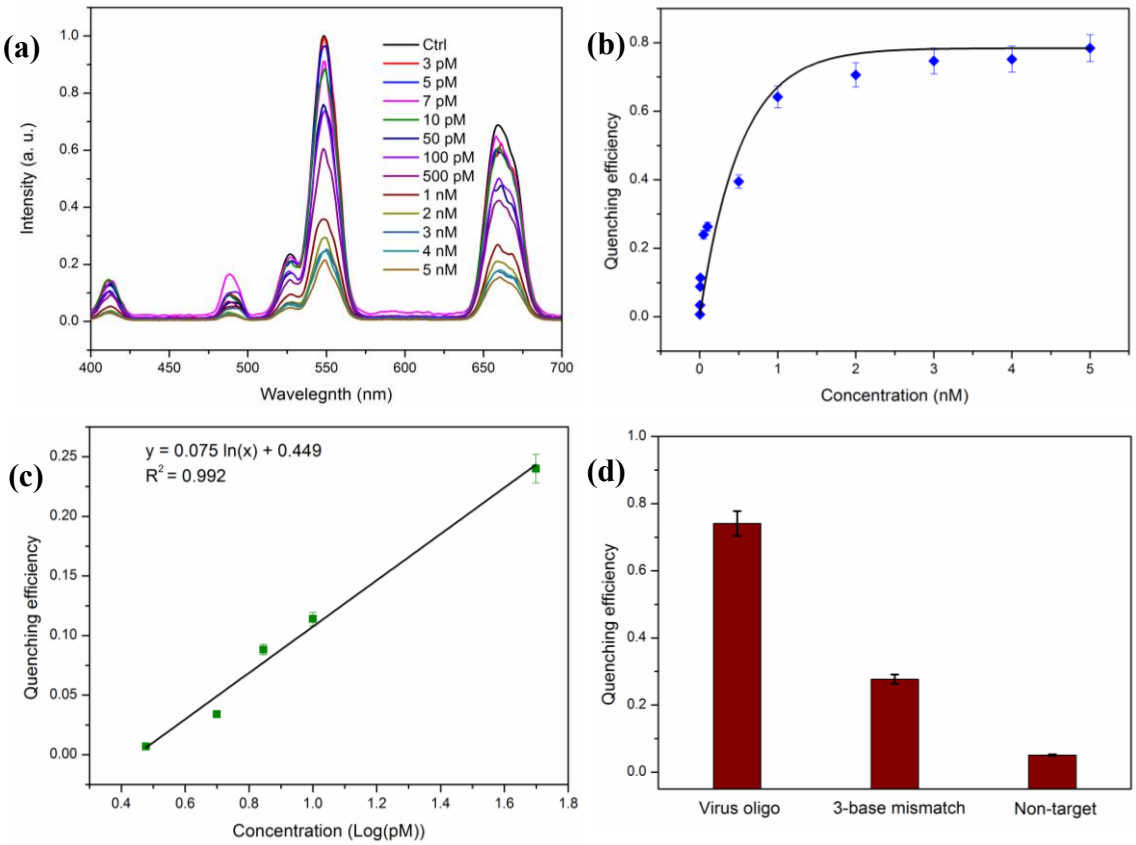

Figure 27(a) UC emission spectra and (b) Quenching efficiencies various concentrations of simulated Ebola virus oligos; (c) Linearity at the pM range and (d) Specificity of homogeneous assay.

3.4.2 Heterogeneous assay with UCNCs-NAAO-AuNPs

Despite the simplicity of the homogeneous assay, its sensitivity is not sufficient for detection of lethal viruses. The heterogeneous assay is well-known for its high sensitivity; hence the NAAO membrane was used as the substrate to fabricate the assay. Previously, NAAO membranes served as filtering membrane for chemical purifications and electrochemical detections. This work firstly utilized NAAO membrane as the

matrix for supporting increased hybridization reactions. The hypothesis was supported by the same amount of UCNCs in a piece of alumina foil and NAAO membrane. Figure 28 shows the UCL spectra of the UCNCs/foil (ALO) and UCNCs/NAAO membrane composite. The UCL was found to enhance by 6-folds in the UCNCs/NAAO membrane compared to that of UCNCs-foil, such enhancement may be attributed to the increased capturing of UCNCs in the nanopores.

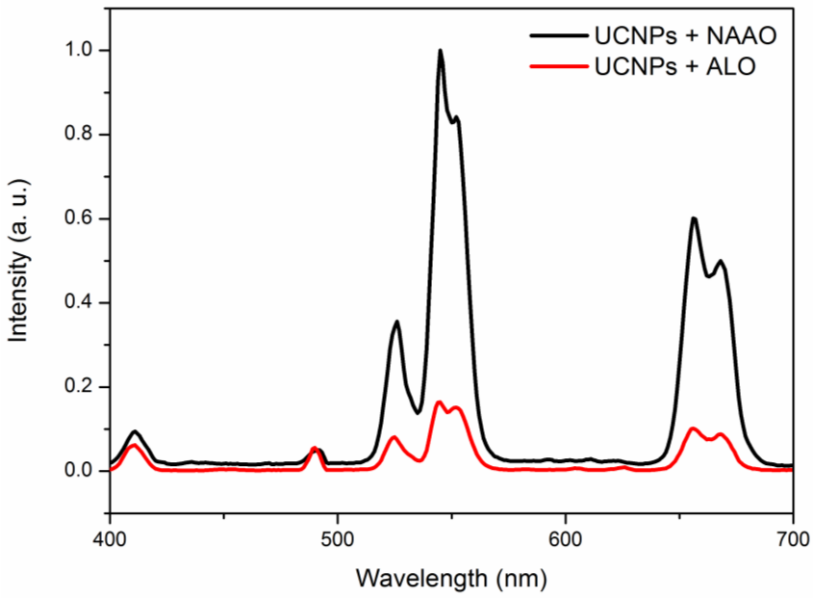

Figure 28 UCL enhancement of UCNCs/NAAO membrane compared to that of UCNCs/ALO.

The UCL enhancement provided insight for the fabrication of the UC nanoprobe/NAAO membrane assay for enhancing the sensitivity of the detection. Figure 29(a) depicts the UCL emission spectra of the heterogeneous assay. Similar to the homogeneous assay, the control was 0.2 mg/ml UC-probe in NAAO membrane. The quenching efficiency (Figure 29(b)) also saturated at around 80 %, because the same

amount of AuNPs for capturing the virus oligo. However, the linear working range was found at femtomolar (fM) range, fitted as y = 0.0003x + 0.0163 (Figure 29(c)) and the specificity test in Figure 29(d) suggests that the difference in UCL intensity could retain for at least 50 % between the virus oligo and the non-target sample.

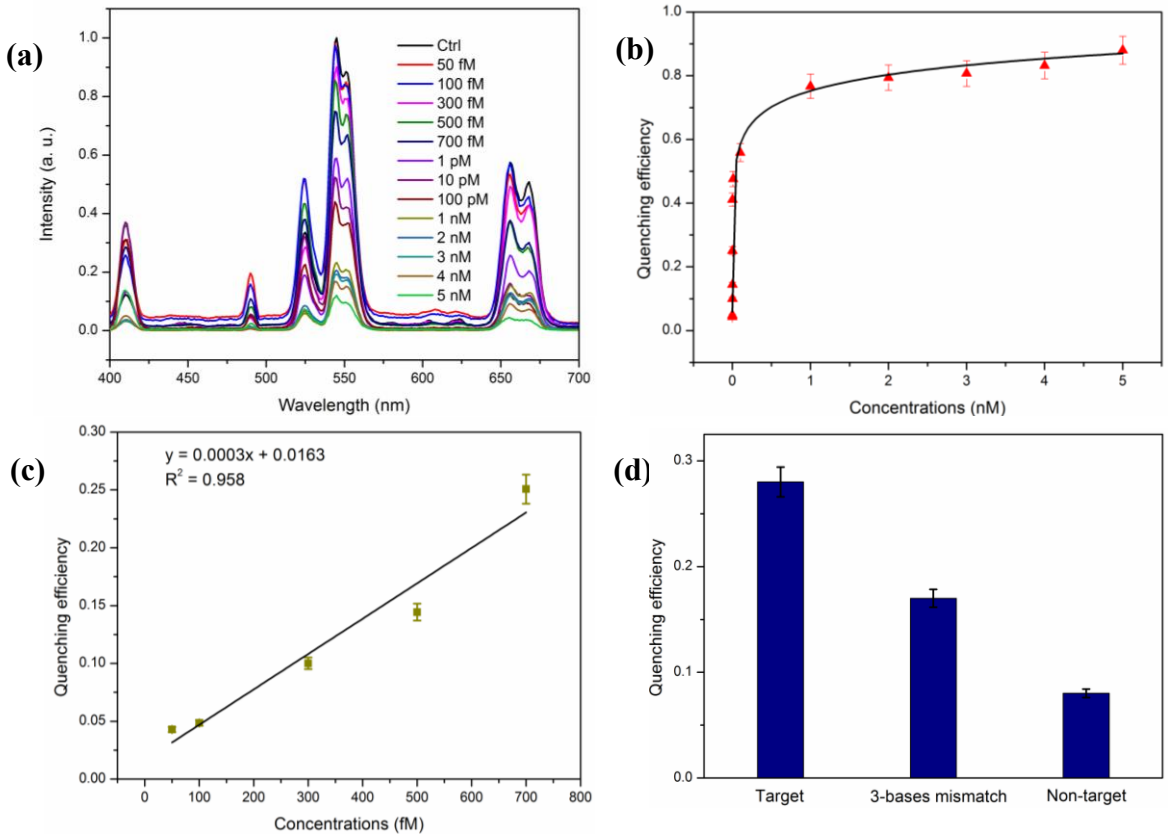

Figure 29(a) UC emission spectra and (b) Quenching efficiencies of the UC nanoprobe/NAAO membrane heterogeneous assay, (c) Linearity at the fM range and (d) Specificity of heterogeneous assay.

3.4.3 Detection of inactive Ebola virus RNA using heterogeneous assay

The total RNA from the Ebola virons was extracted by using a viral RNA kit. The AuNPs were functionalized with carboxylic acid to facilitate the capturing of Ebola RNAs. Subsequently, the anchored UC-probes in the NAAO membrane were hybridized with the extracted RNA. The UCL emission spectra against different concentrations of Ebola RNA are shown in Figure 30(a). The results show that the heterogeneous system performs well for extracted viral RNA in the range of pM to fM levels. Notably, the concentration of Ebola viral RNA extracted from can be detected as low as 500 fM. In addition, the quenching efficiency can also be attained as indicated in Figure 30(b). Therefore, this indicated that the novel heterogeneous assay might be useful for future biomedical detection purposes.

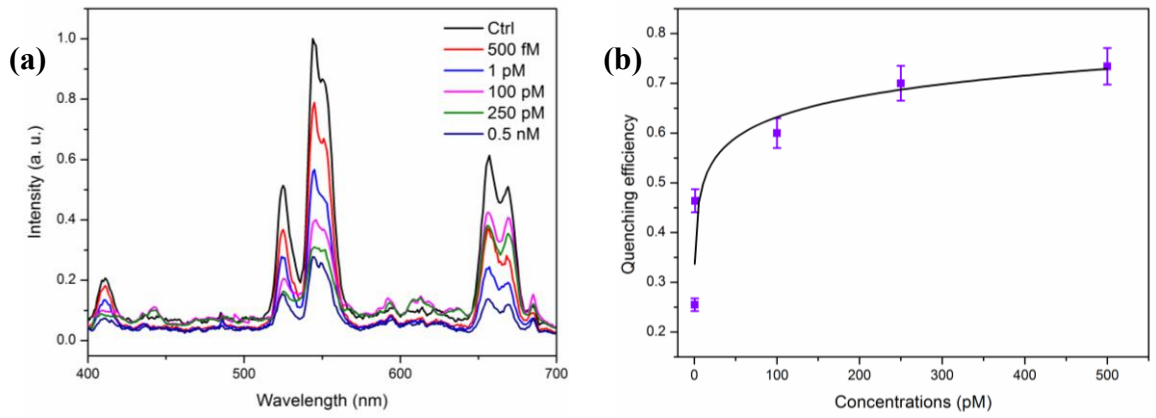

Figure 30(a) UCL emission spectra and (b) Quenching efficiencies of Ebola viral RNA detection.

3.5 Discussion

The use of PEI modified $BaGdF_5$:Yb/Er UCNCs had been combined with AuNPs to form a heterogeneous assay in the NAAO membrane. The novel heterogeneous assay improved the LOD of the assay by increasing the light-matter interaction throughout the cross-section of the NAAO membrane. In addition, the LOD of the assay had been increased by around 20-folds compared to the homogeneous assay. At this stage, the LOD is not suitable to compare with that of qPCR because the LOD of qPCR is referring to the initial amount of copies of genes. In the future, the assay may detect the targets without amplification and that may fairly compare with the LOD of qPCR technique. Despite the improvements, the assay required 980 nm laser for excitation. It is well-known that the water absorption coefficient is not minimal; hence the test may induce heating effect to the sample.[152] The heating effect, in fact, is detrimental to the assay because thermal agitation may cause DNA dehybridization. Figure 31(a) and (b) shows the heating effect of 980 nm laser in water and melting curve of the hybridized DNA duplex with AuNPs, respectively. Although 980 nm laser posed heating effect to the assay, the effect is not significant to the dehybridization as shown in Figure 31(b).

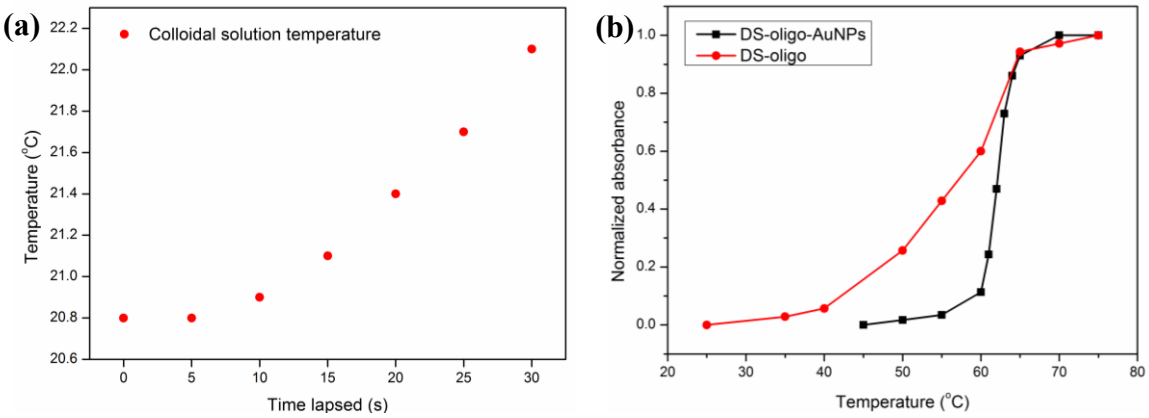

Figure 31(a) Heating effect of 980 nm laser in water in 30 s and (b) Melting curve of double strand oligo with or without AuNPs.

Apart from heating effect, the luminescent intensity is another issue because the synthesis of brighter UCNCs implying the smaller required amount of UCNCs. Moreover, the recognition of target oligo will be critical for the detection. In actual detection environment, there are substantial amount of disturbance in the extracted samples, for example ions and different strands of DNA oligos, therefore functional group-based capturing might not be suitable.

4. Nanobiosensor for influenza virus subtypes detection

4.1 Introduction

In recent years, the influenza (flu) epidemic has become a global problem. The seasonal flu virus that infects human being belongs to type A flu. Those viruses mutate with different combinations of hemagglutinin (HA) and viral neuraminidase (NA). They are the key proteins that are found on the surface of the flu viruses. HA is responsible for binding the virus to cells with sialic acid (SA) on the membranes, such as cells in the upper respiratory tract or erythrocytes while NA enables the releasing of the virus from the host cell, the protein is also able to cleave SA from glycoproteins, which required for flu virus replication. There are at least 18 types of HA gene and 11 types of NA gene associated with type A flu. As a result, the rapid and specific detection of the HA and NA gene might be helpful in the rapid screening of the patients in the peak seasons of flu.

The previous chapter presented a NAAO membrane-based heterogeneous assay to enhance the LOD of the detection assay. The assay was firstly tested with simulated sample of Ebola virus oligo followed by the inactive clinical samples of Ebola virons. The citrated stabilized AuNPs were modified with a carboxylic acid to capture the viral RNA via chemical capturing. As mentioned, actual clinical samples for detection are much more complicated, because of the presence of ions, non-target oligo strands or

even micro-organisms. Therefore, the detection scheme should be modified to enable the luminescent nanobiosensor for real-world detection application. The subtypes of the flu viruses were selected to prove the specificity of the new design.

This chapter describes a heterogeneous sandwich scheme based on two strands of oligo probes on csUCNCs and AuNPs. The LRET mechanism in the previous chapter still holds but the target recognition is completely different. The target flu virus oligo strand is divided into two sections for recognition. Then, the probe oligos hybridize separately with the virus oligos and they bridge the two types of nanoprobes for LRET. This detection scheme avoids the non-specific hybridization to non-targets and increases the ease of handling. Moreover, the csUCNCs were coupled to nPS to form the composite to accommodate the hybridization reaction as the heterogeneous sandwich assay.

4.2 Experimental

4.2.1 Synthesis of $NaGdF_4$:Yb/Er core UCNCs

In a typical coprecipitation synthesis, 0.4 mmol of Ln^{3+} acetate (Gd^{3+}, Yb^{3+} and Er^{3+} ions) solution with designated molar ratio were added to a 50 ml three-necked flask. After that, 4 ml OA and 6 ml ODE were added to the same flask under magnetic stirring. The mixture was heated to 100 ^{o}C for 30 min followed by 150 ^{o}C for 1 h. The heating mantle was removed and the mixture was allowed to cool down to room temperature under magnetic stirring. Then, 1 mmol NaOH/methanol and 1.32 mmol NH_4F/methanol were mixed by vortexing for 10 and immediately injected into the reaction mixture. After that, the temperature was heated to 50 ^{o}C for 1 h under stirring to remove methanol. The flask was connected to the dual gas/vacuum manifold for degassing in 10 min, and then the mixture was heated to 290 ^{o}C in 1.5 h under argon gas protection. After cooling to room temperature, the crude UCNCs were purified by using cyclohexane and ethanol. Finally, the core UCNCs were dispersed in 4 ml cyclohexane for further modifications.

4.2.2 Synthesis of $NaGdF_4$:Yb/Er@$NaGdF_4$:Yb/Nd core-shell UCNCs

In a typical synthesis, 0.4 mmol of Ln^{3+} acetate (Gd^{3+}, Yb^{3+} and Nd^{3+} ions) solution with designated molar ratio were added to a 50 ml three-necked flask. After that, 4 ml OA and 6 ml ODE were added to the same flask under magnetic stirring. The mixture was heated to 100 ^{o}C for 30 min followed by 150 ^{o}C for 1 h. The heating mantle was removed and the mixture was allowed to cool down to room temperature under magnetic stirring. Then, the core UCNCs in 4 ml cyclohexane were injected into the flask. 1 mmol NaOH/methanol and 1.32 mmol NH_4F/methanol were mixed by vortexing for 10 and immediately injected into the reaction mixture. After that, the temperature was heated to 50 ^{o}C for 1 h under stirring to remove methanol. The flask was connected to the dual gas/vacuum manifold for degassing in 10 min, and then the mixture was heated to 290 ^{o}C in 1.5 h under argon gas protection. After cooling to room temperature, the crude csUCNCs were purified by using cyclohexane and ethanol. Finally, the csUCNCs were dispersed in 4 ml cyclohexane for further modifications.

4.2.3 Ligand-free and PAA modification of csUCNCs

1 ml of the csUCNCs in cyclohexane was centrifuged and redispersed in 2M hydrochloric acid with ethanol. Then, the mixture was subjected to 20 min sonication. After high-speed centrifugation at 14000 rpm for 30 min, the supernatant was discarded. Then, the same procedure was repeated until the vanishing of the brown color. After that, 5 mg ligand-free csUCNCs were dispersed in 3 ml DI water under magnetic

stirring in a beaker. Then, 100 mg PAA powder was dissolved in the reaction medium. After 10 min, 1 ml 1M NaOH solution was injected into the beaker. The mixture was stirred for 24 h and purified by high-speed centrifugation using DI water.

4.2.4 Instantaneous conjugation of thiolated oligo to AuNPs

The thiol-modified DNA oligo was obtained from IDT Inc. and then cleaved by 0.1 M DTT in water. After that, gel column (illustra MicroSpin G-25 Columns, GE Healthcare, UK) was used to purify the cleaved thiolated oligo and suspend in water for further use. Traditionally, the salt aging method was used for conjugating thiolated oligo to citrate-stabilized AuNPs. The aging usually required one to two days for completion. In the contrast, the instantaneous conjugation of thiolated oligo to AuNPs was manifested by the salt-acid synergetic effect.[153] Briefly, 200 μL citrate-stabilized AuNPs was mixed with 4 μL cleaved thiolated oligo and 3.2 μL 50 mM phosphate buffer (PB). Then, 10 μL citrate buffer was added and mix thoroughly by vortexing. After 10 min, the AuNPs-oligo was extracted by centrifugation and resuspended in 10 mM PB.

4.2.5 Sandwich homogeneous assay

The sandwich detection scheme divided the complementary sequence of the target into two strands.[154] The half strands of probes on csUCNCs were modified with amine functional group while the other half was conjugated onto AuNPs via chemisorption of Au-S bond of thiolated oligo.

i) The amine modified probe sequences for csUCNCs were listed below,

H1: 5'-TTACCCAAATGCA-3' (13 bases)

H3: 5'-ACGCAGCAAAGCC-3' (13 bases)

H5: 5'-TGGGTACGCTGCA-3' (13 bases)

H7: 5'-TGACCCAGTCAA-3' (12 bases)

N1: 5'-CAGCGGAAGTT-3' (11 bases)

N2: 5'-CTTCCCCTTAT-3' (11 bases)

N8: 5'-ACTATGAGATTG-3' (12 bases)

N9: 5'-AGACAATCCCCG-3' (12 bases)

ii) The probe sequences for AuNPs were listed below,

H1: 5'- ATGGGGCTACCCC-3' (13 bases)

H3: 5'-TACAGCAACTGTT-3' (13 bases)

H5: 5'-GACAAAGAATCCA-3' (13 bases)

H7: 5'-ACTAAGCAGCGG-3' (12 bases)

N1: 5'- TCGTTCAACAT-3' (11 bases)

N2: 5'-CAACTCCACA-3' (10 bases)

N8: 5'-CCGACTGGTCA-3' (11 bases)

N9: 5'-ACCGAATGACCC-3' (12 bases)

0.5 mg PAA-csUCNCs were dispersed in 2-(N-morpholino)ethanesulfonic acid MES buffer (pH = 3.4). After that, (1-ethyl-3-(3-dimethylaminopropyl)carbodiimide hydrochloride) (EDC) and (N-hydroxysuccinimide) (NHS) powder at molar ratio of 2:3 were added to the colloidal and shaken for 10 min. Then, the NHS activated csUCNCs were centrifuged to remove the supernatant. After redispersing in MES buffer, 1 nmol probe oligo was injected to the tube for conjugation for 1.5 h. Finally, the csUCNCs-probe was purified by centrifuged in water and dispersed in 10 mM phosphate buffer for storage at 4 ^{o}C.

After that, 50 μg csUCNCs-probe and 200 μL AuNPs-probe were hybridized with various concentrations of simulated flu virus oligo target in 1X PBS for 2 h at 25 ^{o}C. The control sample was prepared by mixing the two types of probes in 1X PBS. The UCL emission spectra were recorded by using 808 nm laser operating at 250 mW.

The target sequences were listed as follows,

H1: 5'-GGGGTAGCCCCATTGCATTTGGGTAA-3' (26 bases)

H3: 5'-AACAGTTGCTGTAGGCTTTGCTGCGT-3' (26 bases)

H5: 5'-TGGATTCTTTGTCTGCAGCGTACCCA-3' (26 bases)

H7: 5'-CCGCTGCTTAGTTTGACTGGGTCA-3' (24 bases)

N1: 5'-ATGTTGAACGAAACTTCCGCTG-3' (22 bases)

N2: 5'-TGTGGAGTTGATAAGGGGAAG-3' (21 bases)

N8: 5'-TGACCAGTCGGCAATCTCATAGT-3' (23 bases)

N9: 5'-GGGTCATTCGGTCGGGGATTGTCT-3' (24 bases)

4.2.6 Sandwich heterogeneous assay using csUCNCs/nPS system

The csUCNCs/nPS composite was fabricated by using the EDC/NHS reaction. 5 mg PAA-UCNCs were dispersed in MES, EDC and NHS were added with a molar ratio of 2:3. After stirring for 10 min, the NHS-csUCNCs were centrifuged to remove the supernatant. The NHS-csUCNCs was redispersed in 875 μL MES. 125 μL nPS with concentration of 2 mg/mL was added to shake for 2 h. Finally, the csUCNCs/nPS composite was centrifuged at 3000 rpm for 10 min with DI water. The purified composite was stored in 1 ml DI water for further use. Then, the as-prepared csUCNCs/nPS composite was redispersed in MES and repeated with the EDC/NHS activation step and centrifugation. After that, 0.5 nmol probe oligo was added to conjugate with the csUCNCs/nPS for 2 h. The composite with probe was dispersed in 10 mM PB for further hybridization reaction. 50 μg csUCNCs/nPS-probe was mixed with AuNPs-probe and various target oligo sequences in 1X PBS for 2 h. The control sample was prepared by mixing the two types of probes in 1X PBS. The UCL emission spectra were recorded by using 808 nm laser operating at 250 mW.

4.3 Characterizations

4.3.1 UCL-AuNPs sandwich detection system

The previous chapter presented the ability of nanoporous membrane for superior LOD. The main cost of the heterogeneous arose from the membrane; therefore the nPS is used as the carrier for the heterogeneous sandwich assay for reducing the cost and increase the ease for handling. The formation of the csUCNCs/nPS composite forms the fundamental reaction platform for the heterogeneous sandwich detection system. The amine-functionalized nPS was obtained from Sinochem and the PAA-csUCNCs were encapsulated into the nanopores by the efficient EDC/NHS reaction. The heterogeneous sandwich assay consists of the csUCNP-probe, AuNPs-probe and the target is shown in Figure 32. In the presence of the target oligo, the hybridization reaction of the probes and target oligo bring the csUCNCs and AuNPs in close proximity, therefore manifests the spatial condition for LRET. This assay is simple for handling, rapid and low-cost.

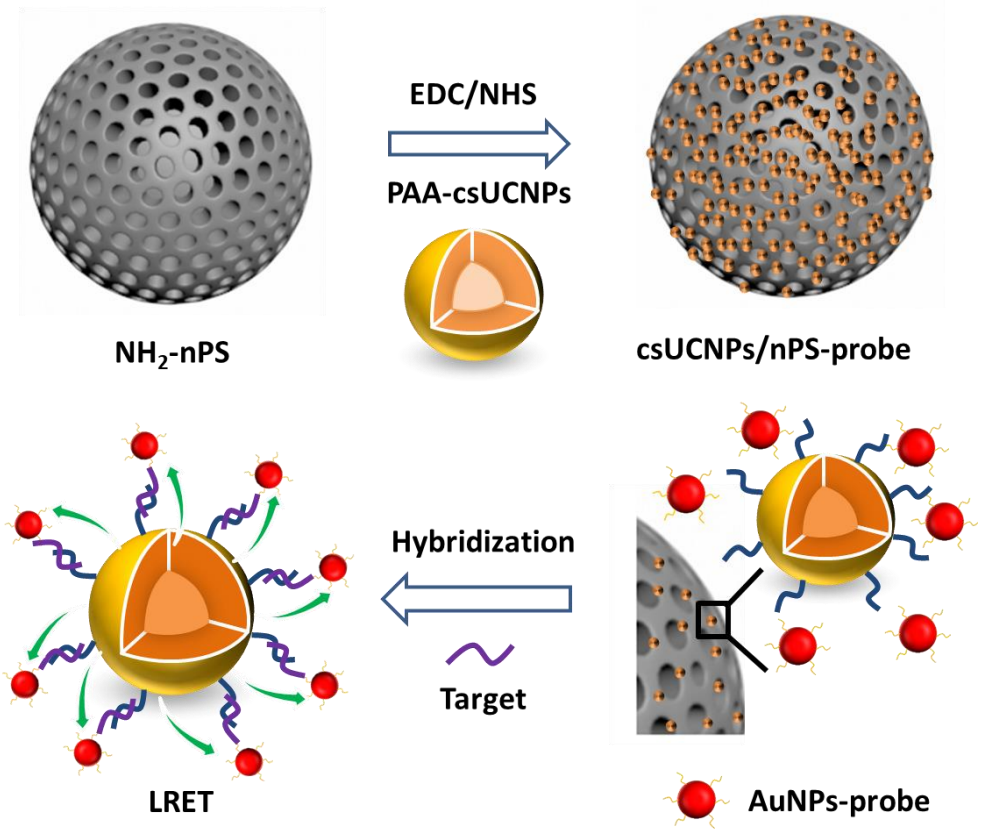

Figure 32 Schematic drawing of the spatial scenario of the UCL-AuNPs sandwich heterogeneous assay by using csUCNCs/nPS composite.

4.3.2 Morphology and structure of the core and core-shell UCNCs

The $NaGdF_4$:Yb/Er core UCNCs were synthesized by the coprecipitation method and the products are all protected by a layer of oleate group because of the OA molecules in the reaction medium. Hence, they can be dispersed in non-polar solvents, such as cyclohexane, toluene or chloroform, to form a stable colloidal. Figure 33(a) shows the morphology of the as-synthesized $NaGdF_4$:Yb/Er core UCNCs. The core UCNCs present a regular morphology with high dispersity, the hexagonal shape and small size distribution was attributed to the capping of OA. The shape homogeneity is crucial to the epitaxial growth of the shell layer because irregular morphology may not favor the growth of the shell due to high surface energy. Moreover, Figure 33(b) presents the size distribution of the OA-core UCNCs; the average size of the core UCNCs was around 13.53 nm with narrow size distribution. This indicated the good control of the nucleation and growth process. The SAED pattern in Figure 33(c) indicates that the core UCNCs possessed hexagonal phase, this result was in good agreement with the XRD pattern of the core UCNCs in Figure 33(d). The XRD pattern matched well with the standard line pattern of hexagonal phase $NaGdF_4$, the small phase in the diffracted angle was due to the doping of Ln^{3+} ions into the host.

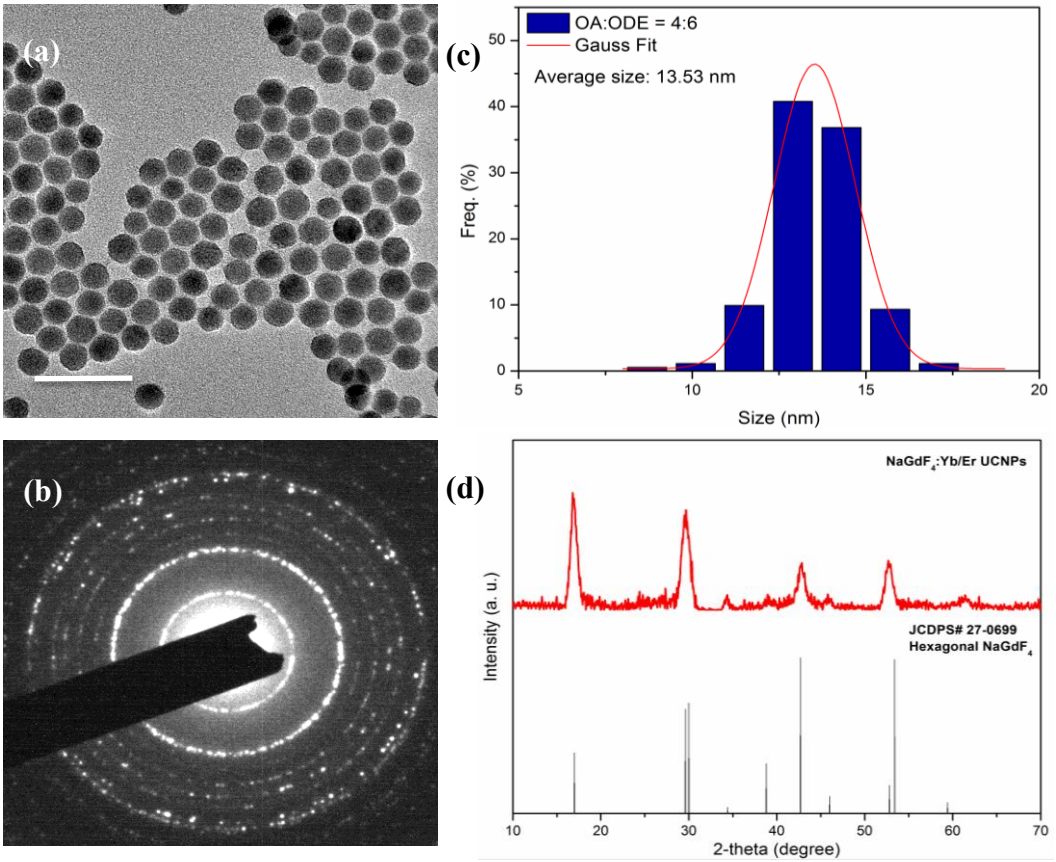

Figure 33(a) TEM image, (b) SAED, (c) Size distribution and (d) XRD pattern of the oleate-capped $NaGdF_4$:Yb/Er core UCNCs (The scale bar is 50 nm).

After confirming the morphology and phase of the core UCNCs, a thin layer of shell was grown on the surface of the core UCNCs to form the csUCNCs. There are different ways to confirm the growth of the shell, the most trivial way is to observe the increase in the crystalline size of the UCNCs. Figure 34(a) presents the morphology of the csUCNCs; there were no major morphologic changes in the shape and dispersity of the csUCNCs. However, Figure 34(b) indicates that the size increment of the UCNCs, this implied the growth of the shell layer onto the core UCNCs. Figure 34(c) and (d) confirms the hexagonal phase nature of the csUCNCs.

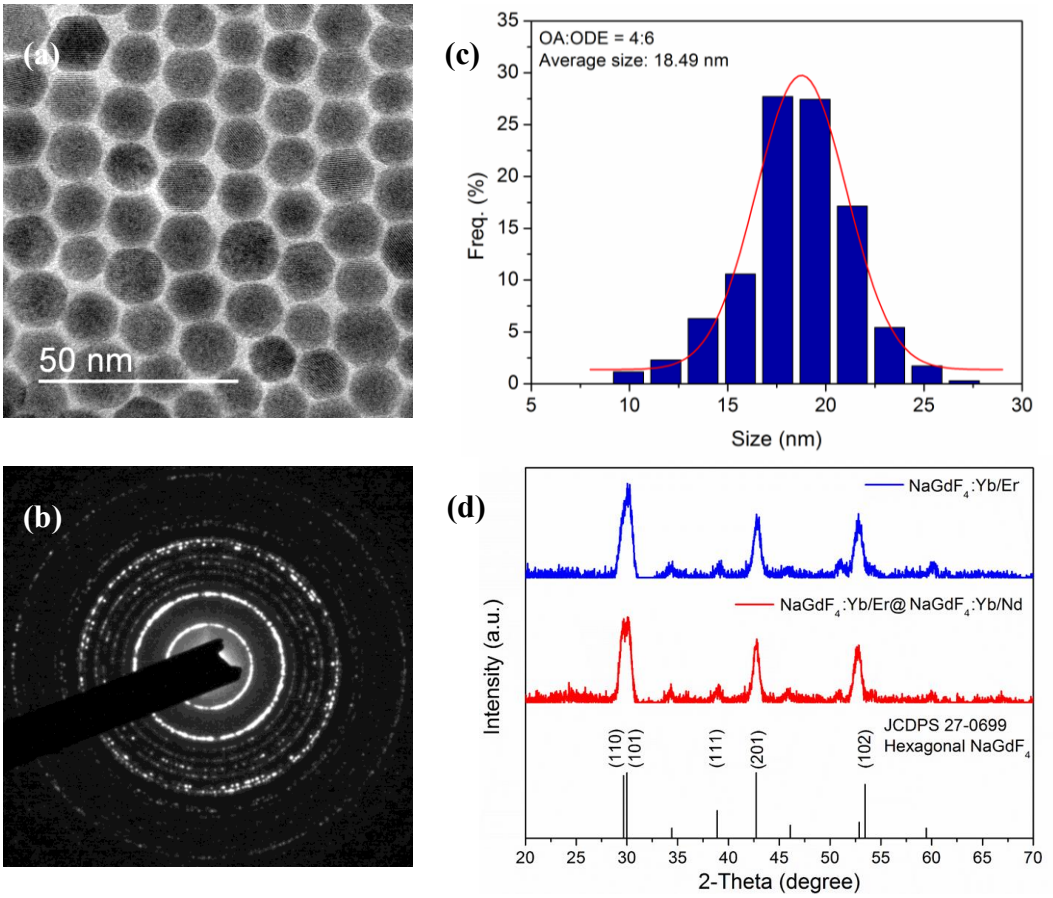

Figure 34(a) TEM image, (b) SAED, (c) Size distribution and (d) XRD pattern of the oleate-capped $NaGdF_4$:Yb/Er@$NaGdF_4$:Yb/Nd csUCNCs.

4.3.3 Optical property of the csUCNCs

The UCL properties of the UCNCs were characterized by using 980 and 808 nm laser excitation. It should be noted that the core UCNCs can only be excited by the 980 nm laser owing to the absence of Nd^{3+} ions while the csUCNCs can either be excited by 980 or 808 nm excitation because of the Nd^{3+} ion doping at the shell layer. In fact, this was the optical evidence for the growth of the shell layer consisting of Nd^{3+} ions. Figure

35(a) and (b) shows the 980 and 808 nm excited UCL spectra at different powers, respectively. The three characteristic emission bands at around 520, 540 and 654 nm were similar to that of the previous Yb/Er-doped UCNCs; however, the peak intensity at 540 nm was more distinct. In addition, the normalized lifetime decay spectra of the emissions are given in Figure 35(c) and (d). The initial rise was due to the energy transfer process from Yb-Er and Nd-Yb-Er.

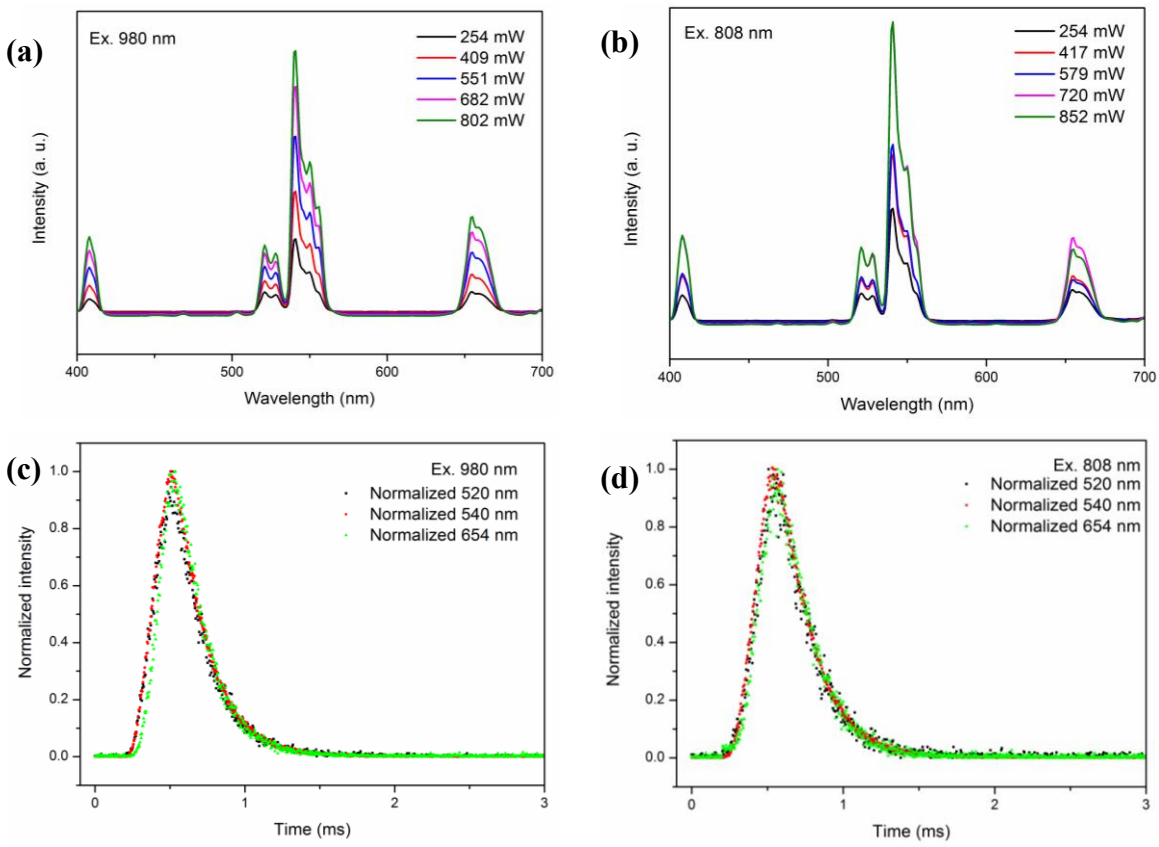

Figure 35(a) 980 nm- and (b) 808 nm-excited UC emission spectra of $NaGdF_4$:Yb/Er@$NaGdF_4$:Yb/Nd csUCNCs. (c) 980 nm- and (b) 808 nm-excited decay profile of the emission bands at 520, 540 and 654 nm in $NaGdF_4$:Yb/Er@$NaGdF_4$:Yb/Nd csUCNCs.

It was predicted that the lifetimes for the emissions for 808 nm excitation were longer than that of 980 nm, this was because the different harvesting position of the photon energy in space. The Nd^{3+} ions harvested the 808 nm excitation followed by the hopping of the energy from the shell into the core layer, while the 980 nm excitation was directly harvested in the core region. The change in the emission lifetimes at various emission bands in Figure 35 were found and tabulated in Table 1. The results showed that the increased UCL lifetimes for the same emission bands, hence these data supported the prediction. Moreover, such delays in the lifetimes provided support to the growth of the shell consisting of Nd^{3+} ions.

Table 1 Comparison of the emission lifetimes at 520, 540 and 654 nm excited by 980 and 808 nm laser excitation at 400 mW.

Emission (nm)	980 nm excited lifetime (μs)	808 nm excited lifetime (μs)
520	232	280
540	248	272
654	216	244

4.3.4 Surface modifications of csUCNCs for biodetection

The oleate surface was replaced by PAA via ligand-free and EDC/NHS reaction to endow hydrophilicity and provide carboxylic acid surface for covalent coupling to the probe oligos. FTIR was used to reveal the surface functional groups by testing the MIR transmission spectra after each step of modification. Figure 36 shows the transmission spectrum of the OA and PAA capped csUCNCs. The two pronounced absorption peaks at 2800-2900 cm^{-1} were attributed to the stretching vibration of the large amount of $-CH_2$ groups on the fatty acid chain. Furthermore, the absorption peak at 1569 cm^{-1} and 1454 cm^{-1} was due to carbonyl stretching and COO^- symmetric vibration, respectively. After ligand exchange with PAA, a large and broad peak appeared at 3446 cm^{-1}, this was ascribed to the vibration of –OH groups in the PAA polymer chains. Moreover, the peak at 1641 cm^{-1} was due to the stretching of C=O.

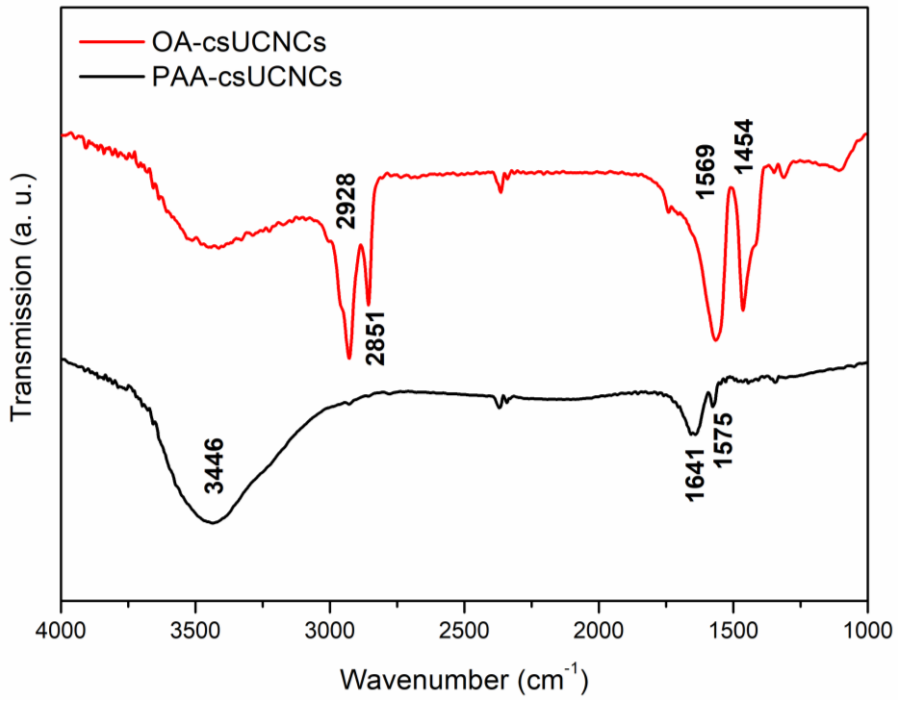

Figure 36 FTIR transmission spectra of OA- and PAA-capped $NaGdF_4$:Yb/Er@$NaGdF_4$:Yb/Nd csUCNCs.

Apart from FTIR, the ξ of the PAA and probe-oligo conjugated csUCNCs were measured in water (Figure 37). The PAA-csUCNCs present a highly negative value at -38 mV; this could be explained by the vast amount of COO^- groups on the PAA polymer chain. After oligo modifications, the ξ value shifted to a less negative value at -11 mV, which could be attributed to the negative charges on the phosphate backbone of oligo chain. Such shift supported the conjugation of the probe oligo to the csUCNCs.

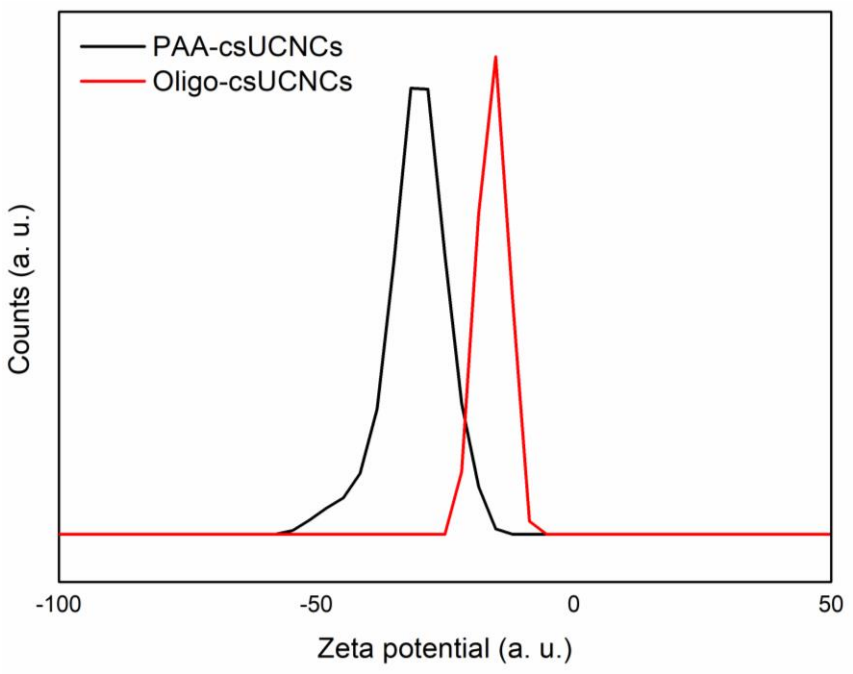

Figure 37 ξ of PAA- and Oligo-csUCNCs.

4.3.5 UV-vis characterization of thiolated oligos and AuNPs-oligo

The thiolated oligos were cleaved by using DTT and purified by the spin column. A loss in thiolated oligo was expected owing to the cleavage reaction and column purification. Hence, it is essential to quantify the amount of recovered thiolated oligos by measuring the optical density at 260 nm. Figure 38(a) presents the molar absorption spectra of the cleaved thiolated oligos, the absorbance at 260 nm indicated consistent decrease in different molar concentrations. The cleaved oligo concentration was denoted as x M and the value was found by using Beer-Lambert Law and the corresponding absorbance (abs). The concentration of cleaved oligo after column purification was around 63 μM (Figure 38(b)).

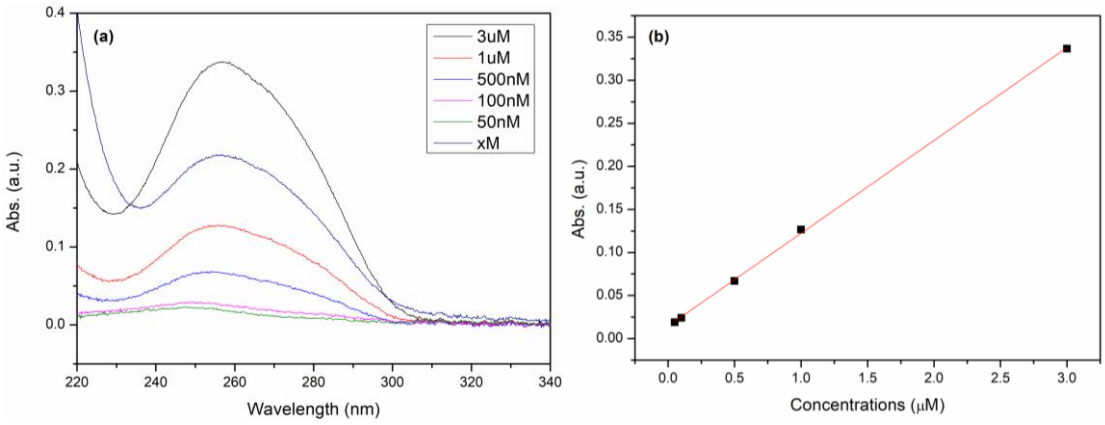

Figure 38(a) Molar absorption spectra of the cleaved thiolated oligo and (b) The absorbance at 260 nm was used to quantify the concentration by Beer-Lambert Law.

The 15 nm citrate-stabilized AuNPs was obtained from Sigma-Aldrich and the thiolated oligo was conjugated on their surfaces via Au-S bond in acidic condition. The absorption spectra of the AuNPs and AuNPs-oligo are shown in Figure 39. The peak absorption was found at around 540 nm. Therefore, the UCL emission spectrum overlapped well with the absorption spectrum of AuNPs. More importantly, there were no observable shift in absorption peak after oligo modification on the AuNPs, this validate the quality of the oligo conjugation onto AuNPs.

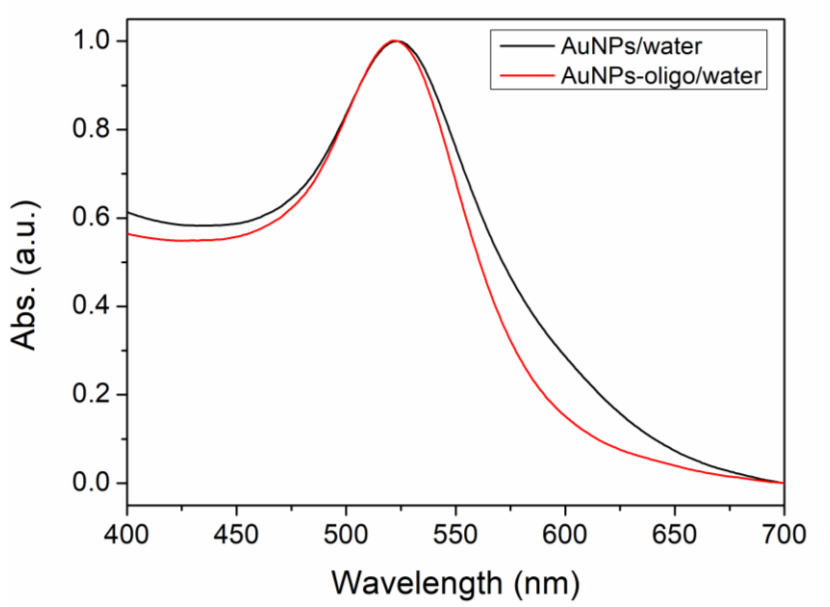

Figure 39 Absorption spectra of AuNPs and AuNPs-oligo for the sandwich heterogeneous assay.

In addition to the absorption property of the AuNPs, the UV-vis spectroscopy was also used to quantify the amount of oligo on the surface of the PAA-csUCNCs via EDC/NHS reaction. An oligo sequence with amine modification at 5' and Cy3 dye modification at 3' was conjugated onto the csUCNCs by EDC/NHS reaction (5'- NH_2 GGACCGCCAAGGTAAAAAATGAGGT-3'-Cy3). The resultant absorption spectrum is shown in Figure 39. The peak absorption at 550 nm corresponded to the maximum absorption of Cy3 was used to quantify the amount of conjugated oligo; it was found that 45 % of the amine-modified oligo was conjugated on the surface of the csUCNCs by using Beer's Law. In fact, this was consistent with the high efficient nature of EDC/NHS reaction.

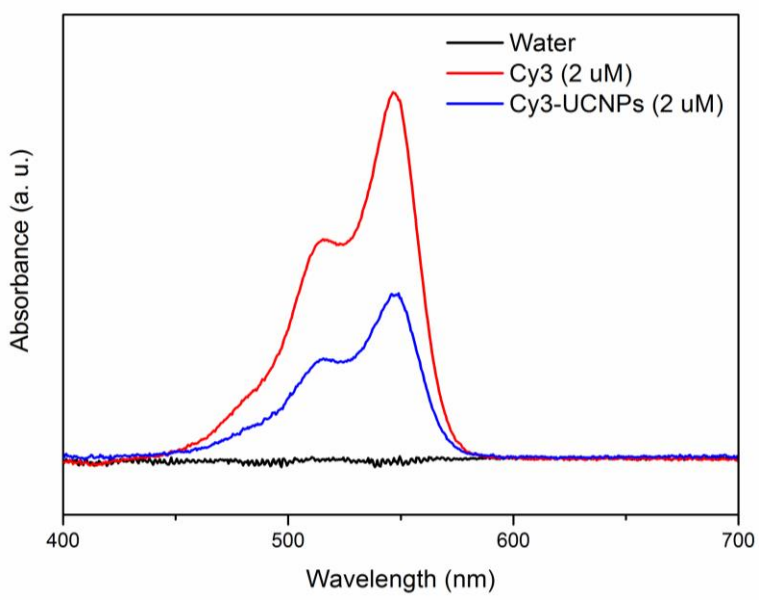

Figure 40 Absorption spectra of water, Cy3 dye and Cy3-UCNCs. The absorption maximum at 550 nm was monitored for finding the coupling efficiency.

4.3.6 Morphology of the csUCNCs/nPS composite

The csUCNCs/nPS composite was prepared by coupling the PAA-csUCNCs to the NH_2-nPS via EDC/NHS reaction. The morphological information of the composite was revealed by SEM. Figure 40(a) shows the homogeneous spherical shape of the nPS, the size was around 5 μm. Figure 40(b) captures a single particle of the nPS, it was clear that the high porosity of the nPS can accommodate a substantial amount of csUCNCs for detection. After the EDC/NHS coupling with csUCNCs, one can observe some small size particle occupying the whole surface of the nPS in Figure 40(c). The high resolution SEM image in Figure 40(d) clear indicates the high capturing density of the csUCNCs in the nPS. Therefore, the change in morphology of the nPS supported the structure of the csUCNCs/nPS composite.

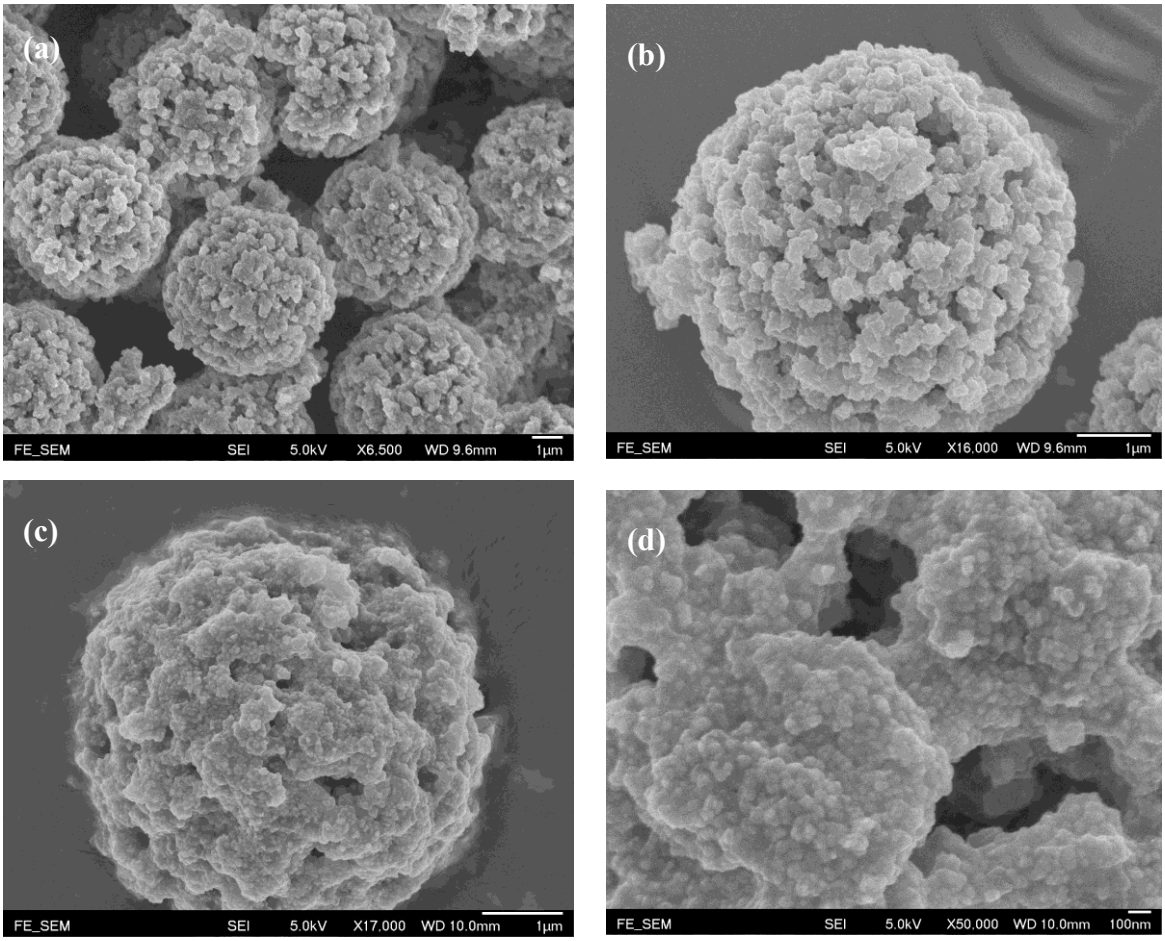

Figure 41(a) Morphology and (b) Single particle image of the nPS. (c) Single particle image and (d) High resolution image of the csUCNCs/nPS composite.

5. Conclusions and suggestions for future work

5.1 Conclusions

Luminescent biodetection assays possess inherent high sensitively towards different types of target; the development of these types of assays may be beneficial to the biomedical field by providing alternative detection routes in addition to traditional PCR and ELISA technique. UCL avoids the drawbacks of downconversion or downshifting luminescence assays by utilizing NIR laser excitation. Therefore, UCNCs hold the promising key as donor in LRET assays.

The PEI-modified $BaGdF_5$:Yb/Er UCNCs had been prepared by using one-step hydrothermal method. The as-synthesized UCNCs were dispersed in water as a stable colloidal owing to the repulsion of the vast amount of amine groups. The UCNCs exhibit green UCL emission when pumped by 980 nm laser while AuNPs were known to have strong absorption at the green regime. The overlapping of the UCL emission and absorption spectrum manifested the spectral requirement for LRET system; the green emission will be quenched when UCNCs and AuNPs were in close proximity. The LRET system was adopted for the homogeneous detection of lethal Ebola virus oligo by modifying the specific sequence of probe oligo on the surface of UCNCs. Therefore, oligo hybridization of the probe and the simulated virus oligo led to the close proximity of UCNCs and AuNPs for efficient LRET. The decrease in the green UCL

was used to quantify the concentration of the virus oligos and the homogeneous assay yielded a LOD of 7 pM. However, the sensitivity for lethal virus should be as high as possible, considering the early administration of cure. On the other hand, nanoporous materials were capable to increase the surface area for chemical reaction. The UCNCs were anchored in the nanochannels of the NAAO membrane by covalent bond to form a heterogeneous assay, which presented a LOD of around 300 fM. The LOD had been increased by around 20 folds compared to the homogeneous assay; such enhancement was attributed to the increased capturing density in the nanochannels. The high density of nanoprobes was able to support more oligo hybridization reaction between the probes and virus oligo. Moreover, the RNA was extracted from the inactive Ebola virons to test the novel heterogeneous assay. The AuNPs were modified to capture the RNA by using covalent bonding to the amine groups on the RNA. The results indicated that the assay was able to detect the concentration of virus RNA down to fM level. Here, the use of clinical samples may validate the possibility of using the heterogeneous assay for future biomedical detections. Apart from LOD, the specificity of the assay was analyzed by using the base mismatch and non-complementary sequences. The results suggested that the NAAO membrane-based heterogeneous assay was specific to the Ebola virus sequence.

Some of the viruses pose threats to human by mutating the genetic sequences as a family of subtypes. Flu viruses are famous example because they mutate themselves to cause seasonal outbreaks. Therefore, the UCL detection scheme was necessary to modify for more selective and sensitive nanosensor to tackle the situation. The

$NaGdF_4$:Yb/Er@$NaGdF_4$:Yb/Nd csUCNCs were synthesized by the coprecipitation method. The hydrophilicity of the csUCNCs were endowed by removing the surface oleate group and replaced by PAA. The amount of required UCNCs were significantly reduced owing to increased UCL intensity compared that from one-step hydrothermal method. The target in the sandwich heterogeneous detection scheme was probed by the two sections of oligo probes on the csUCNCs and AuNPs. As a result, the specificity of the detection was improved by the two segment recognition of the target. The highly efficient EDC/NHS covalent coupling was used to conjugate different sequences of oligo probes onto the surface of csUCNCs; this led to the stable coupling of probes on the csUCNCs. In addition, the csUCNCs were conjugated to nPS to form csUCNCs/nPS composite. The composite inherited the merit of heterogeneous assay in liquid phase, avoiding complicated handling and retained the high LOD. Hence, the improvement was a step-forward towards on-site and actual virus oligo screening applications.

5.2 Suggestions for future work

The developed system aimed to provide another way for luminescent readout for virus oligo detection by using UCNCs. The detection was based on the LRET between the UCNCs and AuNPs, the quenching led to the decrease in the UCL intensities and it was used to evaluate the concentrations of virus oligos. This type of detection was referred as the “signal-off” detection; the drawback of this method might be the decreased signal-to-noise ratio upon the increasing virus oligo concentration. As a

result, the assay can be enhanced by designing a "signal-on" detection system, for example the UCL will be increased when the probe hybridized with the target oligo. Previously, Huang et. al reported the use of $LiLuF_4$ UCNCs for detecting tumor marker by using a heterogeneous assay.[96] The UCL was enhanced owing to the antibody-antigen interaction, the unreacted nanoprobes were washed away to prevent unwanted UCL signal from the non-specific binding. The washing steps were tedious and usually the nanoprobes were sticky to the polymer surface on the microwell plate. Therefore, simpler and faster operation scheme should be developed for the detection.

Molecular beacon (MB) is a type of hair-pin DNA oligo strand probe, which is routinely used in qPCRs.[155–157] The hair-pin or stem-loop structure was essentially a folded DNA structure as shown in Figure 42. The 5' and 3' terminal is usually conjugated with an energy donor and acceptor; therefore the initial state will be at "off" state owing to efficient quenching of luminescence by LRET. After hybridizing with the target in suitable condition, the hairpin structure will be opened to form a double strand structure. The increased distance between the donor and acceptor suppress the LRET for the "on" state, the luminescent intensity will be increased with different concentrations of oligos.

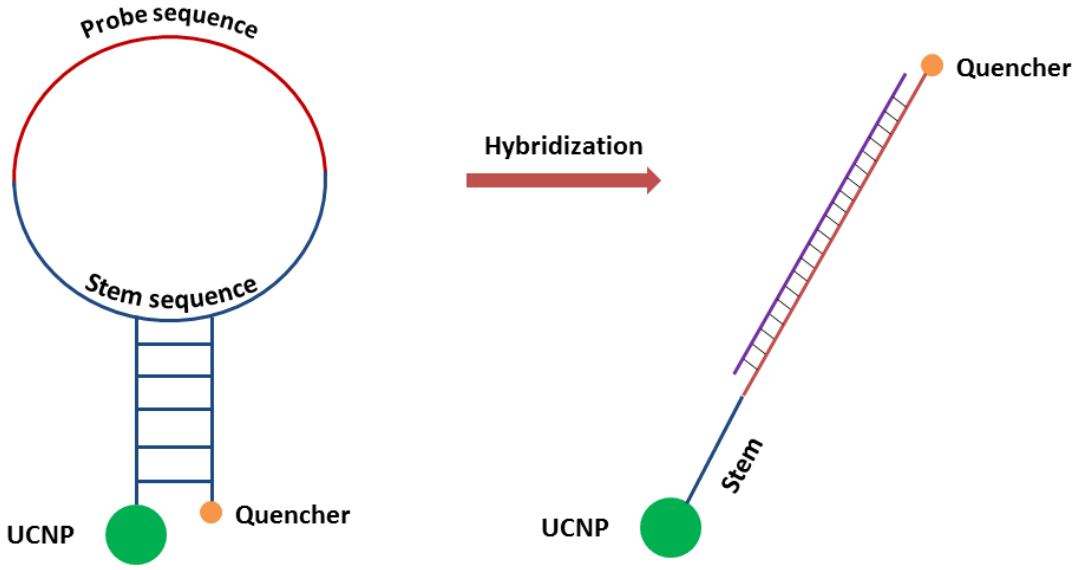

Figure 42 Hair-pin DNA probe structure with UCNP at the 5' and quencher at the 3' terminal. The loop opening of the probe after hybridization forms the double strand structure.

In addition to the hair-pin DNA probe structure, the development of point-of-care (POC) devices for patients is also a feasible direction. The POC devices are useful for rapid screening and high throughput detection applications. In the previous designs of POC, Alere© was one of the devices utilize molecular dyes for rapid detection of targets.[158] Unfortunately, the dyes present short Stokes-shift emission with wide bandwidth. In addition, the cross-talking problem raises issue in the readout by the optical sensor. These shortcomings provide the opportunity for nanoprobes, such as UCNCs, to play the key role in new generation POC devices. The aforementioned flu viruses' outbreaks usually led to a substantial number of patients who might increase the

demand for medical treatment. The POC devices can potentially assist the clinics and hospitals to rapidly screen the suspected patients or the patients can operate the simple device at their homes rather than queueing at the hospitals. As a result, the POC device should be rationally designed to suit simple operation. The dual probe scheme is desirable for the device fabrication because of the high chemical stability of colloidal offered by the probe and the NIR diode laser triggered UCNCs enable miniature design of optical paths. Moreover, the readout part of the device can simply be monitored by a silicon photodiode because the LRET does not involve changes in emission wavelength, therefore the device requires a module that can calculate and compare the UCL intensity for readout.

Recently, the fluorescent imaging in the second biological window (900-1700 nm) has gained considerable attention because of the outstanding penetration ability of photons in living organisms. Ideally, the nanoprobe should possess NIR-NIR fluorescence property with small size ad suitable surface modifications. The primarily results on the coprecipitation synthesis of Nd-doped KY_3F_{10} indicated the downshifting nanoparticles (DSNPs) presented an average size of around 7 nm with orthorhombic phase (Figure 43(a)-(d)). After removing the oleate groups, the DSNPs were functionalized with PAA groups for hydrophilicity. The DSNPs also emit 1056 nm photons upon 808 nm laser excitation (Figure 43(e)). The cytotoxicity test was performed in HeLa cells and the results showed that the PAA-capped DSNPs posed low toxicity even after 24 h incubation. Therefore, these DSNPs were expected to be a useful NIR-NIR fluorescence agent for second window optical diagnosis.

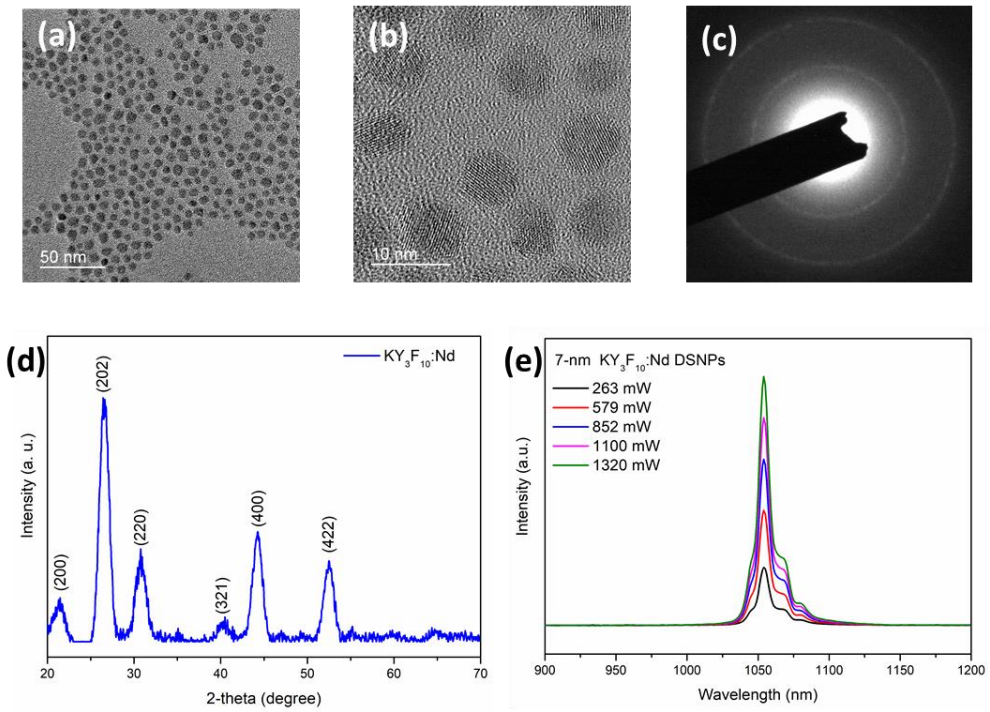

Figure 43 (a) Morphology, (b) HR-TEM, (c) SAED, (d) XRD pattern and (e) NIR-NIR emission spectra of Nd-doped KY_3F_{10} DSNPs.

References

(1) Shionoya, S.; Yen, W. M.; Yamamoto, H.*Phosphor Handbook*; 2 nd.; CRC press: Boca Raton, FL, 2006.

(2) Gu, Y.; Zhang, Q.; Li, Y.; Wang, H.Nitridation from Core-Shell Oxides for Tunable Luminescence of $BaSi_2O_2N_2:Eu^{2+}$ LED Phosphors. *J. Mater. Chem.* **2010**, *20*, 6050.

(3) Sun, Y.; Peng, J.; Feng, W.; Li, F.Upconversion Nanophosphors $NaLuF_4$:Yb,Tm for Lymphatic Imaging *in Vivo* by Real-Time Upconversion Luminescence Imaging under Ambient Light and High-Resolution X-Ray CT. *Theranostics* **2013**, *3*, 346–353.

(4) Blumenthal, T.; Meruga, J.; Stanley May, P.; Kellar, J.; Cross, W.; Ankireddy, K.; Vunnam, S.; Luu, Q. N.Patterned Direct-Write and Screen-Printing of NIR-to-Visible Upconverting Inks for Security Applications. *Nanotechnology* **2012**, *23*, 185305–185312.

(5) Wang, F.; Xie, Z.; Zhang, B.; Liu, Y.; Yang, W.; Liu, C.-Y.Down- and up-Conversion Luminescent Carbon Dot Fluid: Inkjet Printing and Gel Glass Fabrication. *Nanoscale* **2014**, *6*, 3818–3823.

(6) Liu, Y.; Ai, K.; Lu, L.Designing Lanthanide-Doped Nanocrystals with Both Up- and Down-conversion Luminescence for Anti-Counterfeiting. *Nanoscale* **2011**, *3*, 4804–4810.

(7) Li, D.; Wang, Y.; Zhang, X.; Yang, K.; Liu, L.; Song, Y.Optical Temperature Sensor through Infrared Excited Blue Upconversion Emission in Tm^{3+}/Yb^{3+}

Codoped Y_2O_3. *Opt. Commun.* **2012**, *285*, 1925–1928.

(8) Zhang, F.*Photon Upconversion Nanomaterials*; Lockwood, D. J., Ed.; Springer: Berlin Heidelberg, 2015; Vol. 44.

(9) Tan, M. C.; Chow, G.-M.; Ren, L.; Zhang, Q.Inorganic Nanoparticles for Biomedical Applications. In *Nanoscience in Biomedicine*; Shi, D., Ed.; Springer: Berlin Heidelberg, 2009; pp. 272–289.

(10) Liu, T.-C.; Huang, Z.-L.; Wang, H.-Q.; Wang, J.-H.; Li, X.-Q.; Zhao, Y.-D.; Luo, Q.-M.Temperature-Dependent Photoluminescence of Water-Soluble Quantum Dots for a Bioprobe. *Anal. Chim. Acta* **2006**, *559*, 120–123.

(11) Walker, G. W.; Sundar, V. C.; Rudzinski, C. M.; Wun, A. W.; Bawendi, M. G.; Nocera, D. G.Quantum-Dot Optical Temperature Probes. *Appl. Phys. Lett.* **2003**, *83*, 3555–3557.

(12) Zhang, T.; Ge, J.; Hu, Y.; Yin, Y.A General Approach for Transferring Hydrophobic Nanocrystals into Water. *Nano Lett.* **2007**, *7*, 3203–3207.

(13) Auzel, F.Upconversion and Anti-Stokes Processes with F and D Ions in Solids. *Chem. Rev.* **2004**, *104*, 139–173.

(14) Tsang, M.-K.; Zeng, S.; Chan, H. L. W.; Hao, J.Surface Ligand-Mediated Phase and Upconversion Luminescence Tuning of Multifunctional $NaGdF_4$:Yb/Er Materials with Paramagnetic and Cathodoluminescent Characteristics. *Opt. Mater.* **2013**, *35*, 2691–2697.

(15) Gu, H. U.; Pollnau, M.; Gamelin, D. R.; Lu, S. R.Power Dependence of Upconversion Luminescence in Lanthanide and Transition-Metal-Ion Systems ¨. *Phys. Rev. B* **2000**, *61*.

(16) Haase, M.; Schäfer, H.Upconverting Nanoparticles. *Angew. Chem. Int. Ed.* **2011**, *50*, 5808–5829.

(17) Li, C.; Lin, J.Rare Earth Fluoride Nano-/microcrystals: Synthesis, Surface Modification and Application. *J. Mater. Chem.* **2010**, *20*, 6831–6847.

(18) Wang, M.; Abbineni, G.; Clevenger, A.; Mao, C.; Xu, S.Upconversion Nanoparticles: Synthesis, Surface Modification and Biological Applications. *Nanomedicine* **2011**, *7*, 710–729.

(19) Dong, H.; Sun, L.-D.; Yan, C.-H.Energy Transfer in Lanthanide Upconversion Studies for Extended Optical Applications. *Chem. Soc. Rev.* **2014**.

(20) Y. Guyot, H. Manaa, J. Y. Rivoire, and R. M.Excited-State-Absorption and Upconversion Studies of Nd^{3+}-Doped Single Crystals $Y_3A1_5O_{12}$, $YLiF_4$, and $LaMgA1_{11}O_{19}$. *Phys. Rev. B* **1995**, *51*, 784–799.

(21) Quimby, R. S.; Condon, N. J.; O'Connor, S. P.; Biswal, S.; Bowman, S. R.Upconversion and Excited-State Absorption in the Lower Levels of $Er:KPb_2Cl_5$. *Opt. Mater.* **2008**, *30*, 827–834.

(22) Jouart, J. P.; Bissieux, C.; Mary, G.Excited-State Absorption and Upconversion in Er^{3+} Single Sites of $CdF_2:Er^{3+},Na^+$. *J. Phys. C-Solid State Phys.* **1987**, *20*, 2019–2026.

(23) Tse, M. Y.; Tsang, M. K.; Wong, Y. T.; Chan, Y. L.; Hao, J.Simultaneous Observation of Up/down Conversion Photoluminescence and Colossal Permittivity Properties in (Er+Nb) Co-Doped TiO_2 Materials. *Appl. Phys. Lett.* **2016**, *109*, 42903.

(24) Chen, S.; Wu, M.; An, L.; Li, Y.; Wang, S.Strong Green and Red Upconversion

Emission in Er^{3+}-Doped $Na_{1/2}Bi_{1/2}TiO_3$ Ceramics. *J. Am. Ceram. Soc.* **2007**, *90*, 664–666.

(25) Wilhelm, S.; Hirsch, T.; Patterson, W. M.; Scheucher, E.; Mayr, T.; Wolfbeis, O. S.Multicolor Upconversion Nanoparticles for Protein Conjugation. *Theranostics* **2013**, *3*, 239–248.

(26) Suyver, J. F.; Grimm, J.; Krämer, K. W.; Güdel, H. U.Highly Efficient near-Infrared to Visible up-Conversion Process in. *J. Lumin.* **2005**, *114*, 53–59.

(27) Wang, F.; Liu, X.Recent Advances in the Chemistry of Lanthanide-Doped Upconversion Nanocrystals. *Chem. Soc. Rev.* **2009**, *38*, 976–989.

(28) Li, Y.; Wang, G.; Pan, K.; Fan, N.; Liu, S.; Feng, L.Controlled Synthesis and Tunable Upconversion Luminescence of $NaYF_4:Yb^{3+}/Er^{3+}$ Nanocrystals by Pb^{2+} Tridoping. *RSC Adv.* **2013**, *3*, 1683.

(29) Aebischer, A.; Heer, S.; Biner, D.; Krämer, K.; Haase, M.; Güdel, H. U.Visible Light Emission upon near-Infrared Excitation in a Transparent Solution of Nanocrystalline β-$NaGdF_4$: Yb^{3+}, Er^{3+}. *Chem. Phys. Lett.* **2005**, *407*, 124–128.

(30) Du, H.; Zhang, W.; Sun, J.Structure and Upconversion Luminescence Properties of $BaYF_5:Yb^{3+}$, Er^{3+} Nanoparticles Prepared by Different Methods. *J. Alloys Compd.* **2011**, *509*, 3413–3418.

(31) Xue, Z.; Yi, Z.; Li, X.; Li, Y.; Jiang, M.; Liu, H.; Zeng, S.Upconversion Optical/magnetic Resonance Imaging-Guided Small Tumor Detection and *in-vivo* Tri-Modal Bioimaging Based on High-Performance Luminescent Nanorods. *Biomaterials* **2017**, *115*, 90–103.

(32) Zhang, H.; Li, Y.; Ivanov, I. A.; Qu, Y.; Huang, Y.; Duan, X.Plasmonic

Modulation of the Upconversion Fluorescence in $NaYF_4$:Yb/Tm Hexaplate Nanocrystals Using Gold Nanoparticles or Nanoshells. *Angew. Chem. Int. Ed.* **2010**, *122*, 2927–2930.

(33) Hao, J.; Zhang, Y.; Wei, X.Electric-Induced Enhancement and Modulation of Upconversion Photoluminescence in Epitaxial $BaTiO_3$:Yb/Er Thin Films. *Angew. Chem. Int. Ed.* **2011**, *50*, 6876–6880.

(34) Wang, F.; Wang, J.; Liu, X.Direct Evidence of a Surface Quenching Effect on Size-Dependent Luminescence of Upconversion Nanoparticles. *Angew. Chem. Int. Ed.* **2010**, *49*, 7456–7460.

(35) Huang, X.; Han, S.; Huang, W.; Liu, X.Enhancing Solar Cell Efficiency: The Search for Luminescent Materials as Spectral Converters. *Chem. Soc. Rev.* **2013**, *42*, 173–201.

(36) Zheng, W.; Huang, P.; Tu, D.; Ma, E.; Zhu, H.; Chen, X.Lanthanide-Doped Upconversion Nano-Bioprobes: Electronic Structures, Optical Properties, and Biodetection. *Chem. Soc. Rev.* **2015**, *44*, 1379–1415.

(37) Wang, F.; Deng, R.; Wang, J.; Wang, Q.; Han, Y.; Zhu, H.; Chen, X.; Liu, X.Tuning Upconversion through Energy Migration in Core-Shell Nanoparticles. *Nat. Mater.* **2011**, *10*, 968–973.

(38) Jayakumar, M. K. G.; Idris, N. M.; Huang, K.; Zhang, Y.A Paradigm Shift in the Excitation Wavelength of Upconversion Nanoparticles. *Nanoscale* **2014**, *6*, 8441–8443.

(39) Wang, Y.-F.; Liu, G.-Y.; Sun, L.-D.; Xiao, J.-W.; Zhou, J.-C.; Yan, C.-H.Nd^{3+}-Sensitized Upconversion Nanophosphors: Efficient in Vivo Bioimaging Probes

with Minimized Heating Effect. *ACS Nano* **2013**, *7*, 7200–7206.

(40) Wang, D.; Xue, B.; Kong, X.; Tu, L.; Liu, X.; Zhang, Y.; Chang, Y.; Luo, Y.; Zhao, H.; Zhang, H.808 nm Driven Nd^{3+}-Sensitized Upconversion Nanostructures for Photodynamic Therapy and Simultaneous Fluorescence Imaging. *Nanoscale* **2015**, *7*, 190–197.

(41) Wen, H.; Zhu, H.; Chen, X.; Hung, T. F.; Wang, B.; Zhu, G.; Yu, S. F.; Wang, F.Upconverting near-Infrared Light through Energy Management in Core-Shell-Shell Nanoparticles. *Angew. Chem. Int. Ed.* **2013**, *52*, 13419–13423.

(42) Liu, Y.; Tu, D.; Zhu, H.; Li, R.; Luo, W.; Chen, X.A Strategy to Achieve Efficient Dual-Mode Luminescence of Eu^{3+} in Lanthanides Doped Multifunctional NaGdF(4) Nanocrystals. *Adv. Mater.* **2010**, *22*, 3266–3271.

(43) Viswanatha, R.; Sarma, D. D.Growth of Nanocrystals in Solution. In *Nanomaterials Chemistry: Recent Developments and New Directions*; C.N.R., R.; A., M.; A.K., C., Eds.; Wiley-VCH Verlag GmbH & Co. KGaA, 2007; pp. 139–170.

(44) Bahrig, L.; Hickey, S. G.; Eychmüller, A.Mesocrystalline Materials and the Involvement of Oriented Attachment – A Review. *CrystEngComm* **2014**, *16*, 9408–9424.

(45) Wong, H.-T.; Tsang, M.-K.; Chan, C.-F.; Wong, K.-L.; Fei, B.; Hao, J.In Vitro Cell Imaging Using Multifunctional Small Sized $KGdF_4$:Yb^{3+},Er^{3+} Upconverting Nanoparticles Synthesized by a One-Pot Solvothermal Process. *Nanoscale* **2013**, *5*, 3465–3473.

(46) Tsang, M.-K.; Chan, C.-F.; Wong, K.-L.; Hao, J.Comparative Studies of

Upconversion Luminescence Characteristics and Cell Bioimaging Based on One-Step Synthesized Upconversion Nanoparticles Capped with Different Functional Groups. *J. Lumin.* **2015**, *157*, 172–178.

(47) Ye, W. W.; Tsang, M.-K.; Liu, X.; Yang, M.; Hao, J.Upconversion Luminescence Resonance Energy Transfer (LRET)-Based Biosensor for Rapid and Ultrasensitive Detection of Avian Influenza Virus H7 Subtype. *Small* **2014**, *10*, 2390–2397.

(48) Chan, C.-F.; Tsang, M.-K.; Li, H.; Lan, R.; Chadbourne, F. L.; Chan, W.-L.; Law, G.-L.; Cobb, S. L.; Hao, J.; Wong, W.-T.; *et al.*Bifunctional Up-converting Lanthanide Nanoparticles for Selective *in-vitro* Imaging and Inhibition of Cyclin D as Anti-Cancer Agents. *J. Mater. Chem. B* **2014**, *2*, 84–91.

(49) Zeng, S.; Tsang, M.-K.; Chan, C.-F.; Wong, K.-L.; Hao, J.PEG Modified $BaGdF_5$:Yb/Er Nanoprobes for Multi-Modal Upconversion Fluorescent, *in-vivo* X-Ray Computed Tomography and Biomagnetic Imaging. *Biomaterials* **2012**, *33*, 9232–9238.

(50) Wang, F.; Fan, X.; Wang, M.; Zhang, Y.Multicolour PEI/$NaGdF_4$:Ce^{3+} ,Ln^{3+} Nanocrystals by Single-Wavelength Excitation. *Nanotechnology* **2007**, *18*, 025701–025705.

(51) Wang, X.; Zhuang, J.; Peng, Q.; Li, Y.A General Strategy for Nanocrystal Synthesis. *Nature* **2005**, *437*, 121–124.

(52) Wang, F.; Deng, R.; Liu, X.Preparation of Core-Shell $NaGdF_4$ Nanoparticles Doped with Luminescent Lanthanide Ions to Be Used as Upconversion-Based Probes. *Nat. Protoc.* **2014**, *9*, 1634–1644.

(53) Xia, A.; Deng, Y.; Shi, H.; Hu, J.; Zhang, J.; Wu, S.; Chen, Q.; Huang, X.; Shen, J.Polypeptide-Functionalized $NaYF_4$: Yb^{3+}, Er^{3+} Nanoparticles : Red- Emission Biomarkers for High Quality Bioimaging Using a 915 nm Laser. *Appl. Mater. Interfaces* **2014**, *6*, 18329.

(54) Kale, V.; Päkkilä, H.; Vainio, J.; Ahomaa, A.; Sirkka, N.; Lyytikäinen, A.; Talha, S. M.; Kutsaya, A.; Waris, M.; Julkunen, I.; *et al.*Spectrally and Spatially Multiplexed Serological Array-in-Well Assay Utilizing Two-Color Upconversion Luminescence Imaging. *Anal. Chem.* **2016**, *88*, 4470–4477.

(55) Hlaváček, A.; Farka, Z.; Hübner, M.; Horňáková, V.; Němeček, D.; Niessner, R.; Skládal, P.; Knopp, D.; Gorris, H. H.Competitive Upconversion-Linked Immunosorbent Assay for the Sensitive Detection of Diclofenac. *Anal. Chem.* **2016**, *88*, 6011–6017.

(56) Liu, C.; Gao, Z.; Zeng, J.; Hou, Y.; Fang, F.; Li, Y.; Qiao, R.; Shen, L.Magnetic / Upconversion Fluorescent Dual-Modal Molecular Probes for Imaging Tiny Tumors in Vivo. *ACS Nano* **2013**, *7*, 7227–7240.

(57) Zhang, Y.-W.; Sun, X.; Si, R.; You, L.-P.; Yan, C.-H.Single-Crystalline and Monodisperse LaF3 Triangular Nanoplates from a Single-Source Precursor. *J. Am. Chem. Soc.* **2005**, *127*, 3260–3261.

(58) Mai, H.-X.; Zhang, Y.-W.; Si, R.; Yan, Z.-G.; Sun, L.; You, L.-P.; Yan, C.-H.High-Quality Sodium Rare-Earth Fluoride Nanocrystals: Controlled Synthesis and Optical Properties. *J. Am. Chem. Soc.* **2006**, *128*, 6426–6436.

(59) Ye, X.; Collins, J. E.; Kang, Y.; Chen, J.; Chen, D. T. N.; Yodh, A. G.; Murray, C. B.Morphologically Controlled Synthesis of Colloidal Upconversion

Nanophosphors and Their Shape-Directed Self-Assembly. *Proc. Natl. Acad. Sci.* **2010**, *107*, 22430–22435.

(60) Yi, G. S.; Chow, G. M.Synthesis of Hexagonal-Phase $NaYF_4$:Yb,Er and $NaYF_4$:Yb,Tm Nanocrystals with Efficient Up-Conversion Fluorescence. *Adv. Funct. Mater.* **2006**, *16*, 2324–2329.

(61) Mai, H.; Zhang, Y.; Sun, L.-D.; Yan, C.-H.Highly Efficient Multicolor up-Conversion Emissions and Their Mechanisms of Monodisperse $NaYF_4$: Yb, Er Core and Core/shell-Structured Nanocrystals. *J. Phys. Chem. C* **2007**, *111*, 13721–13729.

(62) Du, Y.-P.; Zhang, Y.-W.; Yan, Z.-G.; Sun, L.-D.; Gao, S.; Yan, C.-H.Single-Crystalline and near-Monodispersed $NaMF_3$ (M = Mn, Co, Ni, Mg) and $LiMAlF_6$ (M = Ca, Sr) Nanocrystals from Cothermolysis of Multiple Trifluoroacetates in Solution. *Chem. Asian J.* **2007**, *2*, 965–974.

(63) Boyer, J.-C.; Vetrone, F.; Cuccia, L. A.; Capobianco, J. A.Synthesis of Colloidal Upconverting $NaYF_4$ Nanocrystals Doped with Er^{3+}, Yb^{3+} and Tm^{3+}, Yb^{3+} via Thermal Decomposition of Lanthanide Trifluoroacetate Precursors. *J. Am. Chem. Soc.* **2006**, *128*, 7444–7445.

(64) Sedlmeier, A.; Gorris, H. H.Surface Modification and Characterization of Photon-Upconverting Nanoparticles for Bioanalytical Applications. *Chem. Soc. Rev.* **2015**, *44*, 1526–1560.

(65) Wang, F.; Banerjee, D.; Liu, Y.; Chen, X.; Liu, X.Upconversion Nanoparticles in Biological Labeling, Imaging, and Therapy. *Analyst* **2010**, *135*, 1839–1854.

(66) Yao, J.; Yang, M.; Duan, Y.Chemistry , Biology , and Medicine of Fluorescent

Nanomaterials and Related Systems : New Insights into Biosensing , Bioimaging , Genomics , Diagnostics , and Therapy. *Chem. Rev.* **2014**.

(67) Bogdan, N.; Vetrone, F.; Ozin, G. A.; Capobianco, J. A.Synthesis of Ligand-Free Colloidally Stable Water Dispersible Brightly Luminescent Lanthanide-Doped Upconverting Nanoparticles. *Nano Lett.* **2011**, *11*, 835–840.

(68) Xu, J.; Zhou, S.; Tu, D.; Zheng, W.; Huang, P.; Li, R.; Chen, Z.; Huang, M.; Chen, X.Sub-5 Nm Lanthanide-Doped Lutetium Oxyfluoride Nanoprobes for Ultrasensitive Detection of Prostate Specific Antigen. *Chem. Sci.* **2016**, *7*, 2572–2578.

(69) Tian, J.; Zeng, X.; Xie, X.; Han, S.; Liew, O.; Chen, Y.; Wang, L.; Liu, X.Intracellular Adenosine Triphosphate Deprivation through Lanthanide-Doped Nanoparticles. *J. Am. Chem. Soc.* **2015**, *137*, 6550–6558.

(70) Xiong, L.; Chen, Z.; Tian, Q.; Cao, T.; Xu, C.; Li, F.Targeted Imaging in Vivo Using Peptide-Labeled Nanophosphors. *Anal. Chem.* **2009**, *81*, 8687–8694.

(71) Naccache, R.; Vetrone, F.; Mahalingam, V.; Cuccia, L. A.; Capobianco, J. A.Controlled Synthesis and Water Dispersibility of Hexagonal Phase NaGdF4 : Ho^{3+} /Yb^{3+} Nanoparticles. *Chem. Mater.* **2009**, 717–723.

(72) Shen, J.; Sun, L.-D.; Zhang, Y.-W.; Yan, C.-H.Superparamagnetic and Upconversion Emitting Fe_3O_4/$NaYF_4$:Yb,Er Hetero-Nanoparticles via a Crosslinker Anchoring Strategy. *Chem. Commun.* **2010**, *46*, 5731–5733.

(73) Wu, S.; Han, G.; Milliron, D. J.; Aloni, S.; Altoe, V.; Talapin, D.V; Cohen, B. E.; Schuck, P. J.Non-Blinking and Photostable Upconverted Luminescence from Single Lanthanide-Doped Nanocrystals. *Proc. Natl. Acad. Sci.* **2009**, *106*, 10917–

10921.

(74) Yang, Y.; Shao, Q.; Deng, R.; Wang, C.; Teng, X.; Cheng, K.; Cheng, Z.; Huang, L.; Liu, Z.; Liu, X.; *et al.*In Vitro and *in-vivo* Uncaging and Bioluminescence Imaging by Using Photocaged Upconversion Nanoparticles. *Angew. Chem. Int. Ed.* **2012**, *51*, 3125–3129.

(75) Yang, Y.; Liu, F.; Liu, X.; Xing, B.NIR Light Controlled Photorelease of siRNA and Its Targeted Intracellular Delivery Based on Upconversion Nanoparticles. *Nanoscale* **2013**, *5*, 231–238.

(76) Liu, C.; Wang, H.; Li, X.; Chen, D.Monodisperse, Size-Tunable and Highly Efficient β-$NaYF_4$:Yb,Er(Tm) up-Conversion Luminescent Nanospheres: Controllable Synthesis and Their Surface Modifications. *J. Mater. Chem.* **2009**, *19*, 3546.

(77) Chen, F.; Zhang, S.; Bu, W.; Liu, X.; Chen, Y.; He, Q.; Zhu, M.; Zhang, L.; Zhou, L.; Peng, W.; *et al.*A "neck-Formation" strategy for an Antiquenching Magnetic/upconversion Fluorescent Bimodal Cancer Probe. *Chem. An Eur. J.* **2010**, *16*, 11254–11260.

(78) Li, Z.; Zhang, Y.Monodisperse Silica-Coated Polyvinylpyrrolidone/$NaYF_4$ Nanocrystals with Multicolor Upconversion Fluorescence Emission. *Angew. Chem. Int. Ed.* **2006**, *118*, 7896–7899.

(79) Lü, Q.; Guo, F.; Sun, L.; Li, A.; Zhao, L.Silica-/titania-Coated Y_2O_3:Tm^{3+}, Yb^{3+} Nanoparticles with Improvement in Upconversion Luminescence Induced by Different Thickness Shells. *J. Appl. Phys.* **2008**, *103*, 123533–123542.

(80) Duan, N.; Wu, S.; Zhu, C.; Ma, X.; Wang, Z.; Yu, Y.; Jiang, Y.Dual-Color

Upconversion Fluorescence and Aptamer-Functionalized Magnetic Nanoparticles-Based Bioassay for the Simultaneous Detection of Salmonella Typhimurium and Staphylococcus Aureus. *Anal. Chim. Acta* **2012**, *723*, 1–6.

(81) Tsang, M.-K.; Bai, G.; Hao, J.Stimuli Responsive Upconversion Luminescence Nanomaterials and Films for Various Applications. *Chem. Soc. Rev.* **2015**, *44*, 1585–1607.

(82) González-Béjar, M.; Francés-Soriano, L.; Pérez-Prieto, J.Upconversion Nanoparticles for Bioimaging and Regenerative Medicine. *Front. Bioeng. Biotechnol.* **2016**, *4*, 1–9.

(83) Wu, X.; Chen, G.; Shen, J.; Zhang, Y.; Han, G.; Wu, X.; Chen, G.; Shen, J.; Li, Z.; Zhang, Y.; *et al.*Upconversion Nanoparticles : A Versatile Solution to Multiscale Biological Imaging Upconversion Nanoparticles : A Versatile Solution to Mul- Tiscale Biological Imaging. *Bioconjug. Chem.* **2015**, *26*, 166–175.

(84) Zeng, S.; Tsang, M.-K.; Chan, C.-F.; Wong, K.-L.; Fei, B.; Hao, J.Dual-Modal Fluorescent/magnetic Bioprobes Based on Small Sized Upconversion Nanoparticles of Amine-Functionalized $BaGdF_5$:Yb/Er. *Nanoscale* **2012**, *4*, 5118–5124.

(85) Sun, Y.; Yu, M.; Liang, S.; Zhang, Y.; Li, C.; Mou, T.; Yang, W.; Zhang, X.; Li, B.; Huang, C.; *et al.*Fluorine-18 Labeled Rare-Earth Nanoparticles for Positron Emission Tomography (PET) Imaging of Sentinel Lymph Node. *Biomaterials* **2011**, *32*, 2999–3007.

(86) Cao, T.; Yang, Y.; Sun, Y.; Wu, Y.; Gao, Y.; Feng, W.; Li, F.Biomaterials Biodistribution of Sub-10 nm PEG-Modified Radioactive / Upconversion

Nanoparticles. *Biomaterials* **2013**, *34*, 7127–7134.

(87) Sun, Y.; Zhu, X.; Peng, J.; Li, F.Core-Shell Lanthanide Upconversion Nanophosphors as Four-Modal Probes for Tumor Angiogenesis Imaging. *ACS Nano* **2013**, *7*, 11290–11300.

(88) Liu, Y.; Kang, N.; Lv, J.; Zhou, Z.; Zhao, Q.; Ma, L.; Chen, Z.Deep Photoacoustic / Luminescence / Magnetic Resonance Multimodal Imaging in Living Subjects Using High-Efficiency Upconversion Nanocomposites. *Adv. Mater.* **2016**, *28*, 6411–6419.

(89) Rieffel, J.; Chen, F.; Kim, J.; Chen, G.; Shao, W.; Shao, S.; Chitgupi, U.; Hernandez, R.; Graves, S. A.; Nickles, R. J.; *et al.*Hexamodal Imaging with Porphyrin-Phospholipid-Coated Upconversion Nanoparticles. *Adv. Mater.* **2015**, *27*, 1785–1790.

(90) Xiong, L.; Yang, T.; Yang, Y.; Xu, C.; Li, F.Long-Term *in-vivo* Biodistribution Imaging and Toxicity of Polyacrylic Acid-Coated Upconversion Nanophosphors. *Biomaterials* **2010**, *31*, 7078–7085.

(91) Zhang, F.; Haushalter, R. C.; Haushalter, R. W.; Shi, Y.; Zhang, Y.; Ding, K.; Zhao, D.; Stucky, G. D.Rare-Earth Upconverting Nanobarcodes for Multiplexed Biological Detection. *Small* **2011**, *7*, 1972–1976.

(92) Wu, S.; Duan, N.; Zhu, C.; Ma, X.; Wang, M.; Wang, Z.Magnetic Nanobead-Based Immunoassay for the Simultaneous Detection of Aflatoxin B1 and Ochratoxin A Using Upconversion Nanoparticles as Multicolor Labels. *Biosens. Bioelectron.* **2011**, *30*, 35–42.

(93) Liu, Y.; Chen, M.; Cao, T.; Sun, Y.; Li, C.; Liu, Q.; Yang, T.; Yao, L.; Feng, W.;

Li, F.A Cyanine-Modified Nanosystem for *in-vivo* Upconversion Luminescence Bioimaging of Methylmercury. *J. Am. Chem. Soc.* **2013**, *135*, 9869–9876.

(94) Li, C.; Liu, J.; Alonso, S.; Li, F.; Zhang, Y.Upconversion Nanoparticles for Sensitive and in-Depth Detection of Cu^{2+} Ions. *Nanoscale* **2012**, *4*, 6065–6071.

(95) Liu, J.; Liu, Y.; Liu, Q.; Li, C.; Sun, L.; Li, F.Iridium(III) Complex-Coated Nanosystem for Ratiometric Upconversion Luminescence Bioimaging of Cyanide Anions. *J. Am. Chem. Soc.* **2011**, *133*, 15276–15279.

(96) Huang, P.; Zheng, W.; Zhou, S.; Tu, D.; Chen, Z.; Zhu, H.; Li, R.; Ma, E.; Huang, M.; Chen, X.Lanthanide-Doped $LiLuF_4$ Upconversion Nanoprobes for the Detection of Disease Biomarkers. *Angew. Chem. Int. Ed.* **2014**, *53*, 1252–1257.

(97) Wu, S.; Duan, N.; Shi, Z.; Fang, C.; Wang, Z.Simultaneous Aptasensor for Multiplex Pathogenic Bacteria Detection Based on Multicolor Upconversion Nanoparticles Labels. *Anal. Chem.* **2014**, *86*, 3100–3107.

(98) Bansal, A.; Zhang, Y.Photocontrolled Nanoparticle Delivery Systems for Biomedical Applications. *Acc. Chem. Res.* **2014**.

(99) Yang, D.; Ma, P.; Hou, Z.; Cheng, Z.; Li, C.; Lin, J.Current Advances in Lanthanide Ion (Ln^{3+})-Based Upconversion Nanomaterials for Drug Delivery. *Chem. Soc. Rev.* **2014**.

(100) Dai, Y.; Ma, P.; Cheng, Z.; Kang, X.; Zhang, X.; Hou, Z.; Li, C.; Yang, D.; Zhai, X.; Lin, J.Up-Conversion Cell Imaging and pH-Induced Thermally Controlled Drug Release from $NaYF_4$:Yb^{3+}/Er^{3+}@Hydrogel Core-Shell Hybrid Microspheres. *ACS Nano* **2012**, *6*, 3327–3338.

(101) Zhang, C.; Li, C.; Peng, C.; Chai, R.; Huang, S.; Yang, D.; Cheng, Z.; Lin,

J.Facile and Controllable Synthesis of Monodisperse CaF_2 and CaF_2:Ce^{3+}/Tb^{3+} Hollow Spheres as Efficient Luminescent Materials and Smart Drug Carriers. *Chem. An Eur. J.* **2010**, *16*, 5672–5680.

(102) Wang, Y.; Yang, P.; Ma, P.; Qu, F.; Gai, S.; Niu, N.; He, F.; Lin, J.Hollow Structured $SrMoO_4$:Yb^{3+}, Ln^{3+} (Ln = Tm, Ho, Tm/Ho) Microspheres: Tunable Up-conversion Emissions and Application as Drug Carriers. *J. Mater. Chem. B* **2013**, *1*, 2056–2065.

(103) Zhang, X.; Yang, P.; Dai, Y.; Ma, P.; Li, X.; Cheng, Z.; Hou, Z.; Kang, X.; Li, C.; Lin, J.Multifunctional Up-Converting Nanocomposites with Smart Polymer Brushes Gated Mesopores for Cell Imaging and Thermo/pH Dual-Responsive Drug Controlled Release. *Adv. Funct. Mater.* **2013**, *23*, 4067–4078.

(104) Cheng, L.; Wang, C.; Liu, Z.Upconversion Nanoparticles and Their Composite Nanostructures for Biomedical Imaging and Cancer Therapy. *Nanoscale* **2013**, *5*, 23–37.

(105) Zhou, J.; Liu, Z.; Li, F.Upconversion Nanophosphors for Small-Animal Imaging. *Chem. Soc. Rev.* **2012**, *41*, 1323–1349.

(106) Liu, J.-N.; Bu, W.-B.; Shi, J.-L.Silica Coated Upconversion Nanoparticles: A Versatile Platform for the Development of Efficient Theranostics. *Acc. Chem. Res.* **2015**, *48*, 1797–1805.

(107) Zhou, J.; Liu, Q.; Feng, W.; Sun, Y.; Li, F.Upconversion Luminescent Materials : Advances and Applications. *Chem. Rev.* **2013**.

(108) Wang, C.; Tao, H.; Cheng, L.; Liu, Z.Near-Infrared Light Induced *in-vivo* Photodynamic Therapy of Cancer Based on Upconversion Nanoparticles.

Biomaterials **2011**, *32*, 6145–6154.

(109) Wang, C.; Cheng, L.; Liu, Y.; Wang, X.; Ma, X.; Deng, Z.; Li, Y.; Liu, Z.Imaging-Guided pH-Sensitive Photodynamic Therapy Using Charge Reversible Upconversion Nanoparticles under Near-Infrared Light. *Adv. Funct. Mater.* **2013**, *23*, 3077–3086.

(110) Dong, B.; Xu, S.; Sun, J.; Bi, S.; Li, D.; Bai, X.; Wang, Y.; Wang, L.; Song, H.Multifunctional $NaYF_4$: Yb^{3+}, Er^{3+}@Ag Core/shell Nanocomposites: Integration of Upconversion Imaging and Photothermal Therapy. *J. Mater. Chem.* **2011**, *21*, 6193–6200.

(111) Wang, Y.; Wang, H.; Liu, D.; Song, S.; Wang, X.; Zhang, H.Graphene Oxide Covalently Grafted Upconversion Nanoparticles for Combined NIR Mediated Imaging and Photothermal/photodynamic Cancer Therapy. *Biomaterials* **2013**, *34*, 7715–7724.

(112) Bevan, S.; Rapley, R.; Walker, M. R.Sequencing of PCR-Amplified DNA. *Genome Ressearch* **1992**, *1*, 222–228.

(113) Vlodavsky, I.; Friedmann, Y.; Elkin, M.; Aingorn, H.; Atzmon, R.; Ishai-Michaeli, R.; Bitan, M.; Pappo, O.; Peretz, T.; Michal, I.; *et al.*Mammalian Heparanase: Gene Cloning, Expression and Function in Tumor Progression and Metastasis. *Nat. Med.* **1999**, *5*, 793–802.

(114) Wendland, J.PCR-Based Methods Facilitate Targeted Gene Manipulations and Cloning Procedures. *Curr. Genet.* **2003**, *44*, 115–123.

(115) Martínez, J.; Tomás, G.; Merino, S.; Arriero, E.; Moreno, J.Detection of Serum Immunoglobulins in Wild Birds by Direct ELISA: A Methodological Study to

Validate the Technique in Different Species Using Antichicken Antibodies. *Funct. Ecol.* **2003**, *17*, 700–706.

(116) Moser, C.; Ruggli, N.; Tratschin, J. D.; Hofmann, M. A.Detection of Antibodies against Classical Swine Fever Virus in Swine Sera by Indirect ELISA Using Recombinant Envelope Glycoprotein E2. *Vet. Microbiol.* **1996**, *51*, 41–53.

(117) Yamazaki, Y.; Imura, A.; Urakawa, I.; Shimada, T.; Murakami, J.; Aono, Y.; Hasegawa, H.; Yamashita, T.; Nakatani, K.; Saito, Y.; *et al.*Establishment of Sandwich ELISA for Soluble Alpha-Klotho Measurement: Age-Dependent Change of Soluble Alpha-Klotho Levels in Healthy Subjects. *Biochem. Biophys. Res. Commun.* **2010**, *398*, 513–518.

(118) Hoppe, A.; Christensen, K.; Swanson, J. A.Fluorescence Resonance Energy Transfer-Based Stoichiometry in Living Cells. *Biophys. J.* **2002**, *83*, 3652–3664.

(119) Feng, W.; Han, C.; Li, F.Upconversion-Nanophosphor-Based Functional Nanocomposites. *Adv. Mater.* **2013**, *25*, 5287–5303.

(120) Ghosh, D.; Chattopadhyay, N.Gold Nanoparticles: Acceptors for Efficient Energy Transfer from the Photoexcited Fluorophores. *Opt. Photonics J.* **2013**, *3*, 18–26.

(121) Fan, C.; Wang, S.; Hong, J. W.; Bazan, G. C.; Plaxco, K. W.; Heeger, A. J.Beyond Superquenching: Hyper-Efficient Energy Transfer from Conjugated Polymers to Gold Nanoparticles. *Proc. Natl. Acad. Sci.* **2003**, *100*, 6297–6301.

(122) Swierczewska, M.; Lee, S.; Chen, X.The Design and Application of Fluorophore–gold Nanoparticle Activatable Probes. *Phys. Chem. Chem. Phys.* **2011**, *13*, 9929–9941.

(123) Selvin, P. R.; Rana, T. M.; Hearst, J. E.Luminescence Resonance Energy

Transfer. *J. Amer. Chem. Soc.* **1994**, *116*, 6029–6030.

(124) Anas, A.; Akita, H.; Harashima, H.; Itoh, T.; Ishikawa, M.; Biju, V.Photosensitized Breakage and Damage of DNA by CdSe - ZnS Quantum Dots. *J. Phys. Chem. B* **2008**, *112*, 10005–10011.

(125) Ma, L.; Liu, F.; Lei, Z.; Wang, Z.Biosensors and Bioelectronics A Novel Upconversion @ Polydopamine Core @ Shell Nanoparticle Based Aptameric Biosensor for Biosensing and Imaging of Cytochrome c inside Living Cells. *Biosens. Bioelectron.* **2016**, *87*, 638–645.

(126) Peh, A. E. K.; Li, S. F. Y.Dengue Virus Detection Using Impedance Measured across Nanoporous Alumina Membrane. *Biosens. Bioelectron.* **2013**, *42*, 391–396.

(127) Chan, K. Y.; Ye, W. W.; Zhang, Y.; Xiao, L. D.; Leung, P. H. M.; Li, Y.; Yang, M.Ultrasensitive Detection of E. Coli O157:H7 with Biofunctional Magnetic Bead Concentration via Nanoporous Membrane Based Electrochemical Immunosensor. *Biosens. Bioelectron.* **2013**, *41*, 532–537.

(128) Wang, L.; Yan, R.; Huo, Z.; Wang, L.; Zeng, J.; Bao, J.; Wang, X.; Peng, Q.; Li, Y.Fluorescence Resonant Energy Transfer Biosensor Based on Upconversion-Luminescent Nanoparticles. *Angew. Chem. Int. Ed.* **2005**, *44*, 6054–6057.

(129) Luo, M.; Xiang, X.; Xiang, D.; Yang, S.; Ji, X.; He, Z.A Universal Platform for Amplified Multiplexed DNA Detection Based on Exonuclease III-Coded Magnetic Microparticle Probes. *Chem. Commun.* **2012**, *48*, 7416–7418.

(130) Kumar, A. a.; Hennek, J. W.; Smith, B. S.; Kumar, S.; Beattie, P.; Jain, S.; Rolland, J. P.; Stossel, T. P.; Chunda-Liyoka, C.; Whitesides, G. M.From the

Bench to the Field in Low-Cost Diagnostics: Two Case Studies. *Angew. Chem. Int. Ed.* **2015**.

(131) Xue, X.; Wang, F.; Liu, X.Emerging Functional Nanomaterials for Therapeutics. *J. Mater. Chem.* **2011**, *21*, 13107–13127.

(132) Hunter, R. J.*Zeta Potential in Colloid Science: Principles and Applications.*; 2nd ed.; Academic press, 2013.

(133) WHO Ebola Response Team.Ebola Virus Disease in West Africa — The First 9 Months of the Epidemic and Forward Projections. *N. Engl. J. Med.* **2014**, *371*, 1481–1495.

(134) Gire, S. K.; Goba, A.; Andersen, K. G.; Sealfon, R. S. G.; Park, D. J.; Kanneh, L.; Jalloh, S.; Momoh, M.; Fullah, M.; Dudas, G.; *et al.*Genomic Surveillance Elucidates Ebola Virus Origin and Transmission during the 2014 Outbreak. *Science (80-.).* **2014**, *345*, 1369–1372.

(135) Drosten, C.; Drosten, C.; Schilling, S.; Schilling, S.; Asper, M.; Asper, M.; Panning, M.; Panning, M.; Schmitz, H.; Schmitz, H.Rapid Detection and Quantification of RNA of Ebola and Marburg Viruses, Lassa Virus, Crimean-Congo Hemorrhagic Fever Virus, Rift Valley Fever Virus, Dengue Virus, and Yellow Fever Virus by Real-Time Reverse Transcription-PCR. *J. Clin. Microbiol.* **2002**, *40*, 2323–2330.

(136) Daaboul, G. G.; Lopez, C. A.; Chinnala, J.; Goldberg, B. B.; Connor, J. H.; Unlü, M. S.Digital Sensing and Sizing of Vesicular Stomatitis Virus Pseudotypes in Complex Media: A Model for Ebola and Marburg Detection. *ACS Nano* **2014**, *8*, 6047–6055.

(137) Yanik, A. A.; Huang, M.; Kamohara, O.; Artar, A.; Geisbert, T. W.; Connor, J. H.; Altug, H.An Optofluidic Nanoplasmonic Biosensor for Direct Detection of Live Viruses from Biological Media. *Nano Lett.* **2010**, *10*, 4962–4969.

(138) Li, Y.; Cu, Y. T. H.; Luo, D.Multiplexed Detection of Pathogen DNA with DNA-Based Fluorescence Nanobarcodes. *Nat. Biotechnol.* **2005**, *23*, 885–889.

(139) Feng, C.-L.; Zhong, X. H.; Steinhart, M.; Caminade, A. M.; Majoral, J.-P.; Knoll, W.Graded-Bandgap Quantum- Dot-Modified Nanotubes: A Sensitive Biosensor for Enhanced Detection of DNA Hybridization. *Adv. Mater.* **2007**, *19*, 1933–1936.

(140) Brenner, M.; Hearing, V. J.The Protective Role of Melain Against UV Damage in Human Skin. *Photochem. Photobiol.* **2008**, *84*, 539–549.

(141) Bai, G.; Tsang, M.-K.; Hao, J.Luminescent Ions in Advanced Composite Materials for Multifunctional Applications. *Adv. Funct. Mater.* **2016**, *26*, 6330–6350.

(142) Fan, W.; Bu, W.; Shi, J.On The Latest Three-Stage Development of Nanomedicines Based on Upconversion Nanoparticles. *Adv. Mater.* **2016**, *28*, 3987–4011.

(143) Gai, S.; Li, C.; Yang, P.; Lin, J.Recent Progress in Rare Earth Micro/nanocrystals: Soft Chemical Synthesis, Luminescent Properties, and Biomedical Applications. *Chem. Rev.* **2014**, *114*, 2343–2389.

(144) Tan, F.; Leung, P. H. M.; Liu, Z.; Zhang, Y.; Xiao, L.; Ye, W.; Zhang, X.; Yi, L.; Yang, M.A PDMS Microfluidic Impedance Immunosensor for E. Coli O157:H7 and Staphylococcus Aureus Detection via Antibody-Immobilized Nanoporous

Membrane. *Sensors Actuators B Chem.* **2011**, *159*, 328–335.

(145) Ye, W.; Guo, J.; Chen, S.; Yang, M.Nanoporous Membrane Based Impedance Sensors to Detect the Enzymatic Activity of Botulinum. *J. Mater. Chem. B* **2013**, *1*, 6544–6550.

(146) dela Escosura-Muñiz, A.; Chunglok, W.; Surareungchai, W.; Merkoçi, A.Nanochannels for Diagnostic of Thrombin-Related Diseases in Human Blood. *Biosens. Bioelectron.* **2013**, *40*, 24–31.

(147) Pichetsurnthorn, P.; Vattipalli, K.; Prasad, S.Nanoporous Impedemetric Biosensor for Detection of Trace Atrazine from Water Samples. *Biosens. Bioelectron.* **2012**, *32*, 155–162.

(148) Wang, Z.-L.; Hao, J.; Chan, H. L. W.; Law, G.-L.; Wong, W.-T.; Wong, K.-L.; Murphy, M. B.; Su, T.; Zhang, Z. H.; Zeng, S. Q.Simultaneous Synthesis and Functionalization of Water-Soluble up-Conversion Nanoparticles for in-Vitro Cell and Nude Mouse Imaging. *Nanoscale* **2011**, *3*, 2175–2181.

(149) Tsang, M.-K.; Ye, W.; Wang, G.; Li, J.; Yang, M.; Hao, J.Ultrasensitive Detection of Ebola Virus Oligonucleotide Based on Upconversion Nanoprobe/Nanoporous Membrane System. *ACS Nano* **2016**, *10*, 598–605.

(150) Grabar, K. C.; Freeman, R. G.; Hommer, M. B.; Natan, M. J.Preparation and Characterization of Au Colloid Monolayers. *Anal. Chem.* **1995**, *67*, 735–743.

(151) Karrasch, S.; Dolder, M.; Schabert, F.; Ramsden, J.; Engel, A.Covalent Binding of Biological Samples to Solid Supports for Scanning Probe Microscopy in Buffer Solution. *Biophys. J.* **1993**, *65*, 2437–2446.

(152) Weissleder, R.A Clearer Vision for *in Vivo* Imaging Progress Continues in the

Development of Smaller , More Penetrable Probes for Biological Imaging . Toward the Phosphoproteome. *Nat. Biotechnol.* **2001**, *19*, 316–317.

(153) Zhang, X.; Servos, M. R.; Liu, J.Instantaneous and Quantitative Functionalization of Gold Nanoparticles with Thiolated DNA Using a pH-Assisted and Surfactant-Free Route. *J. Am. Chem. Soc.* **2012**, *134*, 7266–7269.

(154) World Health Organization.*WHO Information for Molecular Diagnosis of Influenza Virus*; 2015.

(155) Hadjinicolaou, A.V; Demetriou, V. L.; Emmanuel, M. A.; Kakoyiannis, C. K.; Kostrikis, L. G.Molecular Beacon-Based Real-Time PCR Detection of Primary Isolates of Salmonella Typhimurium and Salmonella Enteritidis in Environmental and Clinical Samples. *BMC Microbiol.* **2009**, *9*, 97.

(156) Li, J. J.; Fang, X.Molecular Beacons : A Novel Approach to Detect Protein -DNA Interactions. *Angew. Chemie Int. Ed.* **2000**, *87*, 1091–1094.

(157) Ge, Y.; Cui, L.; Qi, X.; Shan, J.; Shan, Y.; Qi, Y.; Wu, B.; Wang, H.; Shi, Z.Detection of Novel Swine Origin Influenza A Virus (H1N1) by Real-Time Nucleic Acid Sequence-Based Amplification. *J. Virol. Methods* **2010**, *163*, 495–497.

(158) Nie, S.; Roth, R. B.; Stiles, J.; Mikhlina, A.; Lu, X.; Tang, Y. W.; Babady, N. E.Evaluation of Alere I Influenza A&B for Rapid Detection of Influenza Viruses A and B. *J. Clin. Microbiol.* **2014**, *52*, 3339–3344.